Exploration of Wood DCB Specimens Using Southern Yellow Pine for Monotonic and Cyclic Loading

by

Brian Liswell

A Thesis submitted to the Faculty of
Virginia Polytechnic Institute and State University
in partial fulfillment of the requirements for the degree of

MASTERS OF SCIENCE

in

Engineering Mechanics

Approved by:

David Dillard, Co-Chairman	Charles E. Frazier, Co-Chairman

Surot Thangjitham

April 16, 2004
Blacksburg, Virginia

Keywords: Fracture Mechanics, Wood Adhesion, Double Cantilever Beam, Adhesive Testing, Fatigue, Cyclic Loading

Exploration of Wood DCB Specimens Using Southern Yellow Pine for Cyclic and Monotonic Loading

by

Brian P. Liswell

Engineering Science and Mechanics

Abstract

The primary direction of this thesis was towards exploring qualitative and quantitative characteristics necessary for refining and understanding the flat wood double cantilever beam (DCB) as a valid means for testing Mode I fracture energy in wood adhesive bonds. Southern yellow pine (SYP) adherends were used with epoxy and phenol formaldehyde (PF) impregnated films, providing two systems with different characteristics for investigation.

An adhesive penetration analysis was performed for both the epoxy and PF bonds. The PF penetration into the SYP was shown to be relatively shallow. The epoxy penetration was shown to be deeper. Epoxy-SYP DCBs were quasi-statically tested with varying widths (10 mm, 15 mm, and 20 mm), showing decreases in scatter of critical and arrest strain energy release rates, G_{Ic} and G_{Ia}, with increases in specimen width. Quasi-static fracture testing was also performed on PF SYP-DCBs, showing much higher critical and arrest fracture energy values than the epoxy-SYP DCBs, indicating that deep adhesive penetration is not necessarily a requisite for higher Mode I fracture energy values.

Grain distribution influences were computationally investigated because of the stiffness difference between latewood and earlywood growth and the grain angle along the length of the beams. The grain angle and the stiffness difference between latewood

and earlywood growth caused the effective stiffness, $(E_{xx}I)_{eff}$, to vary along the length of the beam. The effective stiffness variation caused variations in the beam's ability to receive and store strain energy, complicating and confounding determination of experimental results.

Cyclic loading tests were performed on PF-SYP DCB's. The cycle frequency was 3Hz, with a valley to peak load ratio of $R = 0.5$. Specimen softening was observed with cycling, with re-stiffening occurring with crack growth. Contrary to expectations, specimen compliance occasionally decreased with small crack extensions. A toughening mechanism was frequently observed, whereby subsequent crack lengths required more cycles to failure than the previous crack length. Monotonically extending the crack length far from the fatigued region created a fresh crack that did not show the toughened behavior. But toughening did resume with subsequent crack lengths.

Dedication

A boring piece of technical writing should not be dedicated to a beautiful poet, but I would like to take the opportunity to dedicate this thesis to the love of my life, Emily Morrison.

Acknowledgments

Though many people contributed to this project, I would like to specifically thank Dr. Dillard for his wisdom and experience, Dr. Frazier for his advice and example of boundless energy, and Dr. Thangjitham for his insight and perspective.

I would also like to thank the Center for Adhesive and Sealant Science (CASS) for funding, and Newport Adhesive and Composites, Inc. and Dynea Overlays, Inc. for supplying materials.

TABLE OF CONTENTS

LIST OF FIGURES

LIST OF TABLES

Chapter 1: Background and work explored

1.1 Introduction

Double cantilever beam (DCB) fracture specimens are used to measure Mode I fracture properties of adhesive bonds, and have been standardized in ASTM D3433 for metallic adherends. Several works have been published on using DCB's constructed with wood adherends. Depending on the adhesive system, failures can frequently olccur in the bondline, either cohesively or in the interphase (Frihart, 2004). However, many standard wood adhesion tests are strength-based, which promote wood failure. In fact, a visual estimation of "% wood failure" is recorded with the ultimate strength (ASTM D 905, ASTM D 906). While such tests are valuable (and a mainstay for the industry), tests that promote wood failure actually obscure certain insights into the nature and performance of wood adhesion. A Mode I fracture test which maintains the failure within the wood-adhesive bondline allows for research into wood adhesion mechanisms and structural properties. Wood DCB's offer an excellent opportunity to explore Mode I fracture properties of a wood bond. Loading can be applied in a quasi-static manner, cyclically, in impact tests, or through long term loading. The specimens can be made from virtually any species and adhesive, and subjected to various environmental conditions prior to or during testing.

The motivation of this thesis is to develop specimen configuration and test method recommendations for constant cross-section bonded wood DCB for both quasi-static and cyclic loading tests. Criteria and aspects such as appropriate specimen width, viscoelastic response of the wood, and the significance of adhesive penetration were studied. A novel method for cyclic fatigue testing wood DCBs was developed. All

specimens in this work were made from southern yellow pine (SYP) using epoxy or phenol formaldehyde (PF) adhesive bonds.

A bonded DCB specimen consists of two long adherends (beams) bonded along their length with an initial debond at one end, as shown in Figure 1.1. Loading can be applied by a wedge driven into the debond, or as in this work, by pulling the two beams apart by their ends, inducing Mode I cracking. The specimen can be connected to the loading machine via hinges, pins run through rigid blocks fixed to the beam, or by holes drilled directly through the adherends. The DCB debond is characterized by the strain energy release rate (SERR), G_I, which is defined as the amount of strain energy available per unit of fracture surface area created during Mode I crack growth. In the case of bonded wood DCB's, precise grain control is critical in order that crack propagation remains within the bondline.

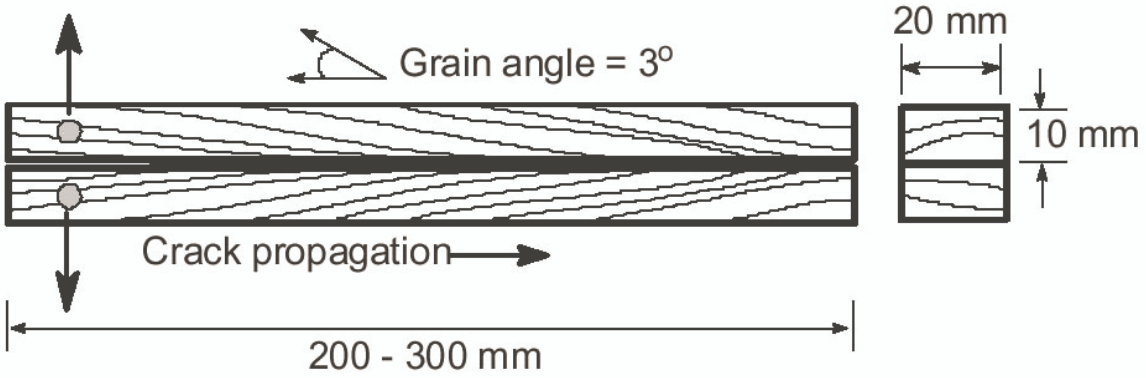

Figure 1.1: A typical wood DCB constructed so the grain converges into the bondline at a small angle, with an initial crack and two holes in one end.

1.2 DCB Mechanics Review

Early work in fracture mechanics using bonded DCB specimens was performed by Mostovoy and associates (1969, 1971). Assuming cohesive fracture within the adhesive bondline, Farhad and colleagues (1977) investigated the role of the adhesive layer in a DCB with isotropic adherends. This was done because the adhesive's

mechanical properties influence the crack's fracture energy. The influence of the adherend and adhesive elastic moduli ratio and thickness ratio on the bond stress distribution and crack tip stress intensity factor was explored. The modulus ratio was found to play the larger role. Korjakin and associates (1998), in studying the influence of glass fiber surface treatment on fracture toughness, evaluated six different methods for calculating the critical SERR G_{Ic}: area method, compliance method, linear beam analysis, finite element analysis (linear and nonlinear), and the modified beam analysis described by Blackman and associates (1991). The results were mixed, though the modified beam method showed the best consistency.

Blackman et al. (1991) published a review of the various correction methods used for DCB quasi-static testing, including the crack length correction, the moment arm correction for large displacements, and a correction for the stiffening contributions from end blocks. Williams (1989) provided an analytically derived correction, using a beam on elastic foundation analysis accounting for both vertical and rotational displacements in the foundation; this was verified with finite element analysis. Williams' approach was incorporated in Hashemi et al's (1991) extensive report on interlaminar Mode I, Mode II, and mixed mode fracture for fiber-polymer composites. In that paper experimental work was used to validate various correction methods and evaluate different methods for calculating G_{Ic}, in particular the cube-root compliance method which is used in the present work. Two methods for calculating the longitudinal stiffness, E_{xx}, were compared, with one method using a crack length correction value. The E_{xx} value which did not use the crack length correction showed increases in stiffness with increases in crack length, which is an erroneous finding. The corrected stiffness value remained

relatively constant with increases in crack length. Furthermore the beam stiffness determined through three-point bending was compared to the beam stiffness derived from the cube-root compliance plot, showing close.

The importance of the ratio of the adherend vertical elastic modulus, E_{yy}, to the adhesive elastic modulus, E_a, was investigated for influences on: fracture toughness (Wang 1978), optimal bondline thickness (Wang 1978, Penado 1993), plastic zone size and stress distribution (Wang 1997). All work was conducted on specimens with $E_{yy}/E_a>1$. Wang and colleagues (1978) performed a finite element analysis of DCB specimens assuming homogeneous isotropic substrates with the crack tip located in the bulk adhesive layer. Varying the adhesive stiffness and keeping the substrate stiffness constant, the system's dependence on the substrate to adhesive stiffness ratio was investigated, though the ratio never went below unity. As the modulus ratio approached unity, the vertical stresses, σ_{yy}, increased in the y direction above the crack tip in both the adhesive and substrate. The distance between the crack tip and the perimeter of the compressive region ahead of the crack tip decreased as the stiffness ratio approached unity. Also the stress intensity factor increased as the adhesive elastic modulus approached that of the substrate, as shown in Figure 1.2.

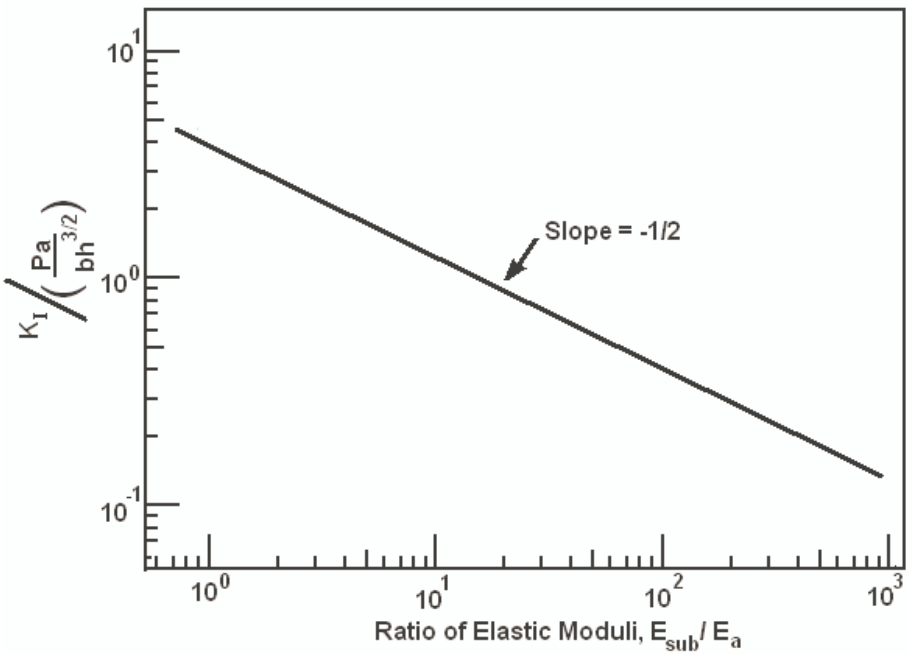

Figure 1.2: **The effect of the elastic modulus ratio E_{sub}/E_a (E_{sub}: adherend modulus, E_a: adhesive modulus) on the mode I stress intensity factor, K_I, normalized with load, P, crack length, a, specimen width, b, and beam height, h, from Wang's (1978) FE modeling.**

Penado (1991) developed a closed form solution for calculating a DCB's G_{Ic} for both isotropic and orthotropic substrates with cohesive adhesive failure, starting with a beam on elastic foundation (no rotational displacement). The difference in Penado's work is that the foundation stiffness is explicitly derived from the adherend and adhesive stiffnesses. Ignoring the adhesive stiffness is practical when the bondline is thin and the adherend is much stiffer. However a system with a thick and stiff adhesive layer, as in epoxy-bonded wood, would benefit from an analysis of vertical stresses, σ_{yy}. Unfortunately, Penado only confirmed his analysis with FE modeling, but no experimental data.

1.3 Strain Energy Release Rate – Corrected compliance method

When a DCB is loaded, strain energy is stored primarily in the specimen's two beams and can be calculated by assuming simple beam theory. With crack growth the length of each beam is extended, making the beam more compliant so that for the same

displacement, the load and strain energy decrease. The amount of strain energy released by crack growth can be used to characterize the adhesive bond over the area exposed. Assuming fixed displacement conditions, a bond's critical strain energy release rate, G_{Ic}, is defined as the strain energy released, *dU*, by fracturing an area of bond, *dA*, as described by Equation 1.1. For a beam of constant width, *b*, and crack length, *a*, the change in area *dA* = *b*da*. The change in strain energy, *dU*, is equal to the area between two subsequent loading cycles in a load versus displacement plot. Examples of subsequent quasi-static load cycles can be seen in the load versus displacement plot shown in Figure 1.3.

$$G_{Ic} = -\frac{dU}{dA} \qquad \textbf{1.1}$$

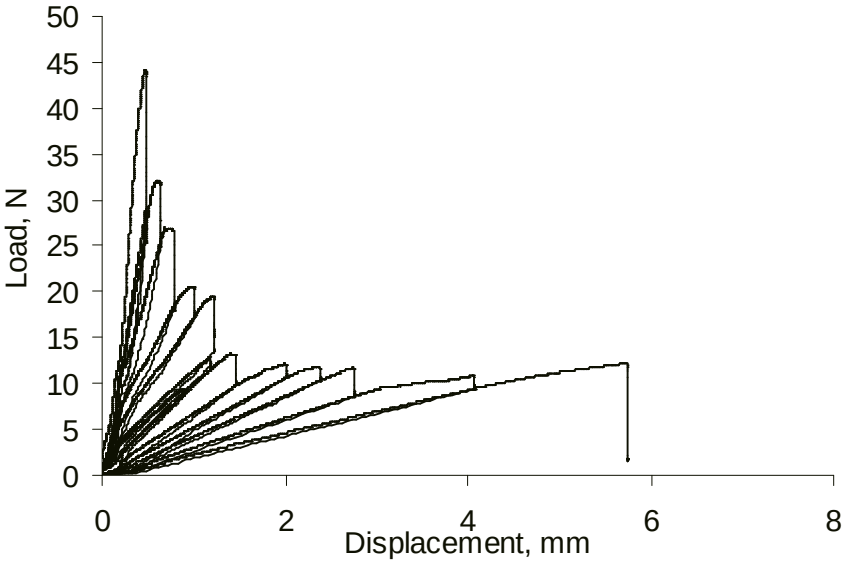

Figure 1.3: Typical load vs. displacement plot for an epoxy-SYP DCB specimen (specimen #: Bd18s3).

The compliance for two deforming beams, C, and the strain energy, U, stored in the two bonded beams are,

$$C = \frac{\delta}{P}$$
$$U = \frac{P\delta}{2} = \frac{P^2 C}{2} \qquad \textbf{1.2}$$

where P is the load applied and δ is the displacement of the loading pins, as shown in Figure 1.4.

Figure 1.4: A diagram of a DCB showing the load and displacement of the two beams.

With crack growth, strain energy changes in the system can be caused by continued increases in loading, or compliance changes. Regardless, Equation 1.1 can be rewritten as

$$G_{Ic} = \frac{1}{2b}\frac{\partial(P^2 C)}{\partial a} = \frac{P^2}{2b}\frac{\partial C}{\partial a} \qquad \textbf{1.3}$$

From classic beam theory, the strain energy stored in the two beams due to normal stresses caused by bending is

$$U = \frac{P^2 a^3}{3E_{xx} I} \qquad \textbf{1.4}$$

where E_{xx} is the Young's Modulus along the length and I is the second moment of area of the cross-section about the neutral axis of an individual beam. From Equations 1.2 and 1.4 the compliance of the entire specimen is

$$C = \frac{2a^3}{3E_{xx} I} \qquad \textbf{1.5}$$

With Equation 1.5, Equation 1.3 becomes:

$$G_{Ic} = \frac{P_c^{\,2} a^2}{b E_{xx} I} \qquad \textbf{1.6}$$

A crack length correction, α, was used by Williams (1989) to take into account the strain energy being stored in the beam beyond the crack tip. Using bonded wood DCB's, Gagliano (2001) compared the direct compliance method for calculating G_I to the corrected compliance method, which uses the crack length correction; the better results were obtained from the latter. (Throughout this thesis the beam's longitudinal, vertical and width directions are defined to be *x*, *y*, and *z*, respectively.) For an orthotropic material such as wood, where the shear modulus, G_{xy}, and the vertical elastic modulus, E_{yy}, are respectively about 1/15th and 1/10th the E_{xx} value, material displacements could occur as much as 35 mm past the crack tip. Williams (1989) derived an approximation for crack correction, α, with a constant Poisson's ratio, ν:

$$\alpha = \sqrt{\frac{1}{18K}\left(\frac{E_{xx}}{G_{xy}}\right)}\left[3 - 2\left(\frac{\Gamma}{1+\Gamma}\right)^2\right]^{1/2}$$
$$\Gamma = \frac{\sqrt{E_{xx}E_{yy}}}{KG_{xy}} \qquad \textbf{1.7}$$
$$K = \frac{10(1+\nu)}{12+11\nu}$$

Clearly α is dependent on orthotropic material properties. This is relevant for many reasons. From a cyclic loading perspective, the moduli in different directions could soften in different manners during fatigue loading, leading to unpredictable changes in the correction value α, thereby changing the G_I being applied.

The crack correction value, α, and the beam effective stiffness $(E_{xx}I)_{eff}$ is determined from the linear fit to the plot of $C^{1/3}$ vs. *a*. The correction α is the negative of the abscissa intercept, while the slope ($m = C^{1/3}/a$) provides the beam effective stiffness,

$(E_{xx}I)_{eff}$ as derived in Equation 1.8 with Equation 1.5. Figure 1.5 is an example of such a plot, with α = 19 mm and stiffness $(E_{xx}I)_{eff}$ = 9.6 N·m^2, and an R^2 value of 0.9967.

$$m = \frac{C^{1/3}}{a} = \left(\frac{2}{3(E_{xx}I)_{eff}} \right)^{1/3}$$
$$(E_{xx}I)_{eff} = \frac{2}{3m^3} \qquad \textbf{1.8}$$

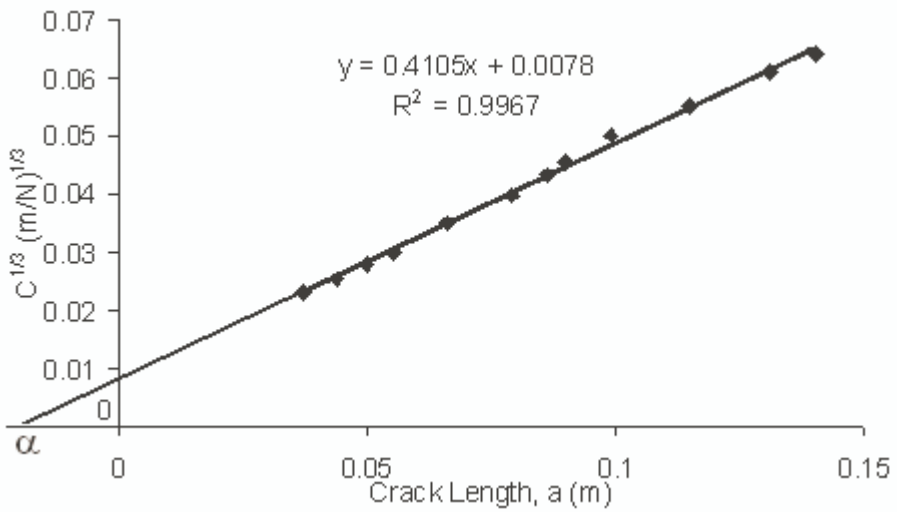

Figure 1.5: **A plot of the cube-root of compliance vs. crack length, *a*, whose slope and absicsa intercept provide the beam effective stiffness $(E_{xx}I)_{eff}$ and crack length correction α, respectively (epoxy-SYP DCB specimen #: Bd20s12).**

The critical strain energy release rate used throughout this work is therefore:

$$G_{Ic} = \frac{P_c^{\,2}(a+\alpha)^2}{b(E_{xx}I)_{eff}} \qquad \textbf{1.9}$$

The arrest fracture energy, G_{Ia}, is acquired by using the load, P_a, and crack length at which crack growth stops, a_a, while the beam end displacement is fixed:

$$G_{Ia} = \frac{P_a^{\,2}(a_a+\alpha)^2}{b(E_{xx}I)_{eff}} \qquad \textbf{1.10}$$

1.4 Wood Mechanics

DCB's can be made of various materials, though in this study they were constructed from southern yellow pine, SYP. For SYP severe density variations occur

within each annual growth ring. Like all woods, SYP is a cellular material; the cell wall is a composite of oriented and highly crystalline cellulose fibrils which are coated and "crosslinked" by amorphous heteropolysaccharides, referred to as hemicellulose. The interfibrillar hemicellulose network is interspersed with an amorphous, polyphenolic network polymer which is called lignin. In SYP the approximate proportion of these macromolecules is about 44% cellulose, 25% hemicellulose, and 31% lignin. The oven-dry specific gravity of SYP ranges from 0.52 – 0.65, which is high among the commercially significant gymnosperms. Furthermore, SYP contains about 2-5% of a complex mixture of natural products which collectively are referred to as wood extractives, so called because these nonstructural compounds are isolated by solvent extraction. Notable among the SYP extractives are free fatty acids, resin acids, neutral terpenes, as well as mono-, di-, and triglycerides. Collectively, the structural and nonstructural components of SYP could interact, and react, with the adhesive in highly specific ways depending upon adhesive chemistry. The molecular and supramolecular organization described above is further complicated by the growth variations that occur in temperate climates.

Entering the spring, wood begins a rapid growth stage with large "earlywood" cells having approximately 50 μm diameter lumens, with about 10 μm thick walls. Subsequent growth during the drier summer months is slower, producing a denser material called latewood, which has thicker walls and smaller cell lumens. An example of the two growth types is shown in Figure 1.6, a micrograph of a microtomed cross-section of a beam, using the method described in Chapter 2. In SYP, the higher density latewood has an elastic modulus which is more than three times the earlywood stiffness

(Cramer et al. 2004). There is also significant variability in strength and stiffness depending on the location in the tree from which the wood was cut (Groom et al. 2002). For work covered in this thesis, the mesoscopic scale of differentiating between latewood and earlywood growth is the smallest scale considered.

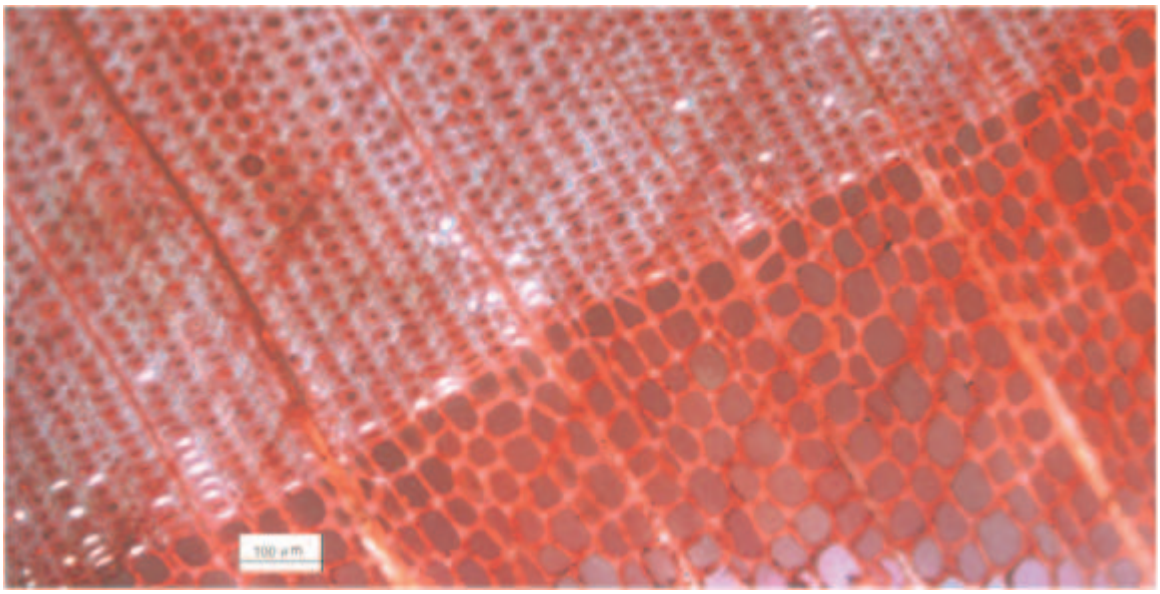

Figure 1.6: **A digital photomicrograph of a transverse section of microtomed and dyed SYP, with the upper region consisting of denser latewood as compared to the lower region consisting of larger and less dense earlywood cells.**

The longitudinal, radial and tangential grain directions define the orthotropic axes of the tree stem. Longitudinal grain, running parallel to the tree's stem, is stiffest in order to resist bending moments from the tree's mass, and from lateral wind loads. The tangential direction is perpendicular to the longitudinal direction and is tangential to the growth rings. The radial direction radiates outward from the pith (stem central axis), normal to the tangential direction. SYP is actually a category of eleven different species, grouped together because of their similar macro-mechanical properties and visual appearances. The most common southern pines are loblolly, short leaf, longleaf and splash pine. Table 1.1 lists the average material properties for loblolly, longleaf and slash. Table 1.2 lists the orthotropic Poisson's ratios and the tensile and shear elastic

moduli for the three orthotropic directions as ratios of the longitudinal modulus, E_L. The radial-tangential plane elastic moduli and Poisson ratios listed in Table 1.1 do not satisfy the reciprocity relation of Equation 1.11. Instead of being equal to 1, the right hand side becomes 0.728 for the listed values. This means the values from Table 1.1 must be used with the understanding that they may be incorrect.

$$\frac{E_T}{E_R}\frac{\nu_{RT}}{\nu_{TR}} = 1 \qquad \textbf{1.11}$$

Table 1.1: Macroscopic material properties for three species of southern yellow pine (Green et. al, 1999).

Species	Specific Gravity	Longitudinal Modulus of Elasticity GPa	Ultimate Compression Strength Parallel to Grain MPa	Ultimate Compression Strength Perpendicular to Grain MPa	Shear Strength Parallel to Grain MPa	Ultimate Tensile Strength Parallel to Grain MPa
Loblolly	0.51	12.3	49.2	5.4	9.6	80.0
Longleaf	0.59	13.7	58.4	6.6	10.4	--
Slash	0.59	13.7	56.1	7.0	11.6	--

Table 1.2: Modulus and Poisson's ratios for different orthotropic directions and planes(Green et. al, 1999).

Species	E_T/E_L	E_R/E_L	G_{LR}/E_L	G_{LT}/E_L	G_{RT}/E_L	ν_{LR}	ν_{LT}	ν_{RT}	ν_{TR}
Loblolly	0.078	0.113	0.082	0.081	0.013	0.328	0.292	0.382	0.362
Longleaf	0.055	0.102	0.071	0.06	0.012	0.332	0.365	0.384	0.342
Slash	0.045	0.074	0.055	0.053	0.01	0.392	0.444	0.447	0.387

Obviously there is significant variation between the species; the variation within a species is also great not to mention the variation even within one tree. Table 1.3 lists the coefficients of variation for different mechanical properties for a wide variety of species. The longitudinal elastic modulus has a coefficient of variation in the range of 22%.

Table 1.3: Average coefficients of variation for some mechanical properties of clear wood (Green et. al, 1999).

Property	Coefficient of variation[a] (%)
Static bending	
Modulus of rupture	16
Modulus of elasticity	22
Work to maximum load	34
Impact bending	25
Compression parallel to grain	18
Compression perpendicular to grain	28
Shear parallel to grain, maximum shearing strength	14
Tension parallel to grain	25
Side hardness	20
Toughness	34
Specific gravity	10

[a]Values based on results of tests of green wood from approximately 50 species. Values for wood adjusted to 12% moisture content may be assumed to be approximately of the same magnitude.

Cramer and colleagues (2004) found the latewood to earlywood ratio for loblolly pine to vary from 0.8 to 6.5 with an average of 2.3. The average earlywood elastic modulus was 4.34 GPa, while the average latewood elastic modulus was 9.88 GPa. It should be noted that these average values produce a macroscopic elastic modulus similar to that given by Green (reference, or indicate table) for the same species. Latewood and earlywood have a similar chemical composition, but the thinner earlywood cell walls are more susceptible to collapse under compression experienced during hot pressing. Examples of this can be seen in Figures 1.7 and 1.8, showing microtomed surfaces, with some collapsed earlywood cell walls, and the unaffected dense latewood growth.

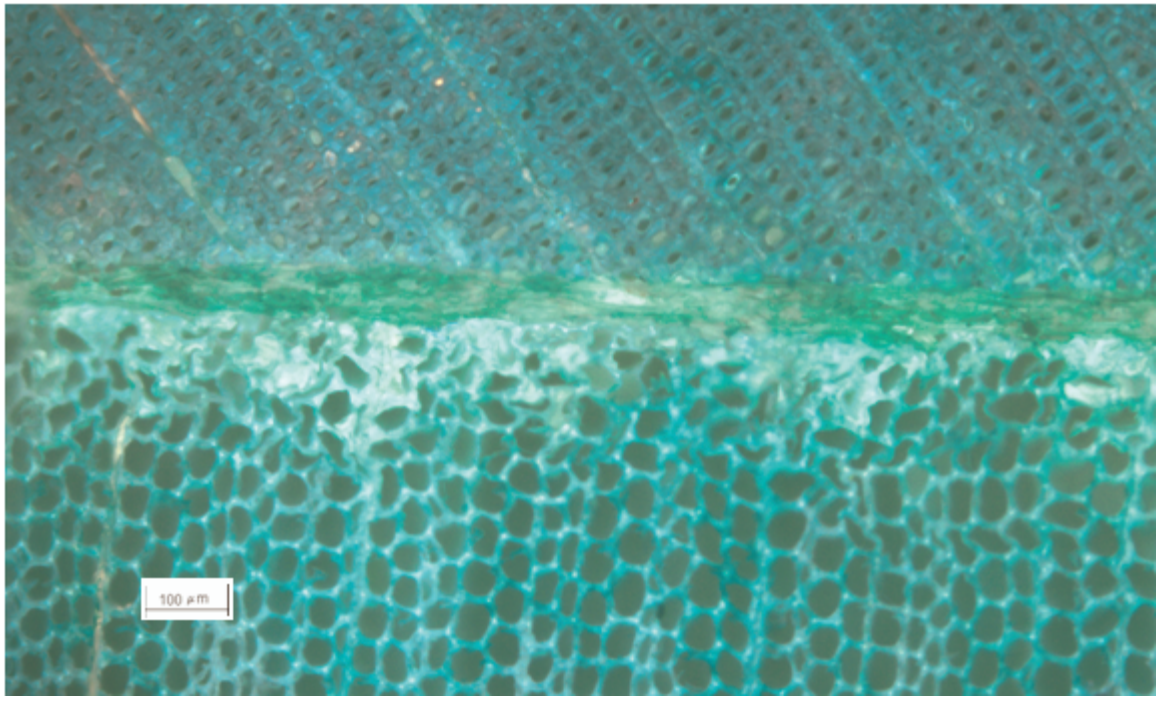

Figure 1.7: **Photomicrograph of microtomed cross-sections of a PF bond, showing collapsed earlywood cells.**

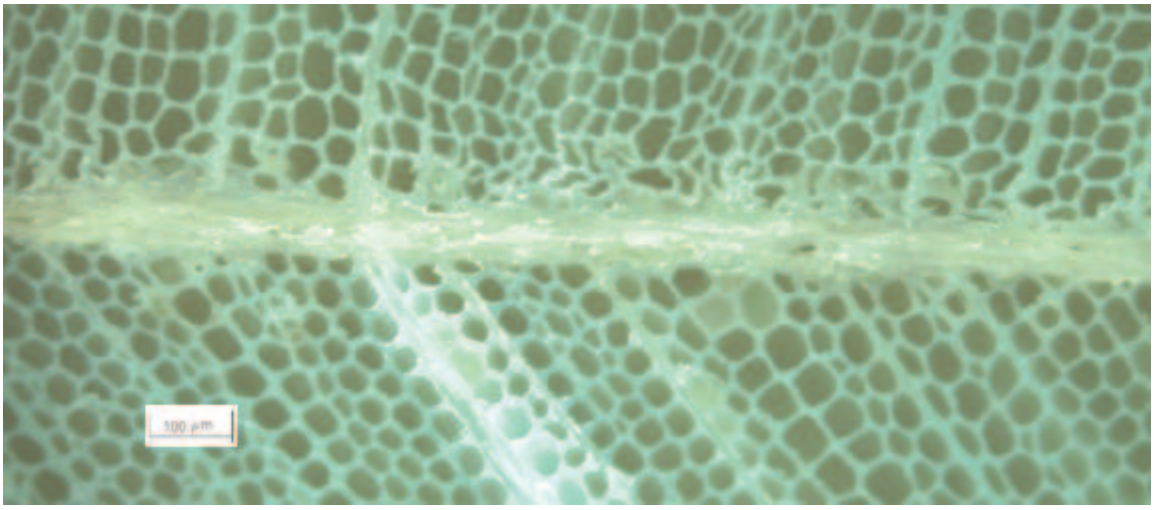

Figure 1.8: **Photomicrograph of microtomed cross-sections of a PF bond, showing collapsed earlywood cells.**

1.5 Wood Fracture Mechanics Review

Several research papers have been published on wood adhesive fracture mechanics, with some using bonded wood DCBs. Ebewelle (1980) constructed tapered DCBs from maple with phenolic adhesives. The specimens were constructed by affixing two precut tapered beams in a jig. All specimens were machined specifically to ensure a

10^{o} grain angle converging at the bondline. The converging grain angle served the function of driving crack growth within the wood adherends back into the bondline. Ebewelle investigated the influence of bondline thickness on fracture energy by using specimens in which the bond thickness varied along the beam length. Consequently, the thickness at each crack tip was used as the measured value. Ebewelle also studied the influence sandpaper grit size and sanding method had on fracture toughness, noting that back and forth hand sanded specimens achieved greater fracture energies than machine sanding in one direction (either parallel or perpendicular to the grain.) He suggested that a crack blunting mechanism (Cook and Gordon 1991) explains the benefits from hand sanding. According to Ebewelle, sanding creates localized failures between wood cells, causing blunted crack tips and reduced plane stress. The back and forth motion of hand sanding proved superior to the unidirectional machine sanding, presumably because of the directional randomization of blunting features associated with hand sanding.

In the same paper, Ebewelle also examined the effect of adhesive fillers and depth of adhesive penetration. He observed that for shallow penetrations, the crack grew into the substrates, while for deep penetrations crack growth remained in the bondline. While this is not true for all wood-adhesive bonds, it does indicate a possible toughening mechanism caused by the penetrated adhesive. Using photomicrographs of fractured surfaces, he noted mostly interfacial failures and showed higher filler concentrations in the adhesive layer with less attached on the substrate interfaces. Ebewelle's research demonstrates fracture behavior will be influenced by wood surface preparation, bondline thickness and the adhesive penetration into the wood substrate. In another paper, again using tapered wood DCB's, Ebewelle (1986) reported the influence wood processing has

on adhesive joint performance, using tapered maple DCB's.

Kyokon, Keenan and Bond (1986) used yellow-poplar to test the validity of Griffith's brittle fracture theory, Rice's J-Integral theory, and Eringen's nonlocal (relating to circular bar tension specimens) theories. They found these theories to be valid for poplar-resorcinal bonds, "provided that the appropriate adjustments are taken into account." This showed various existing fracture mechanics theories can be applied to analyzing wood adhesive bonds. Microphotography was also used to analyze microtomed bond sections, showing the resorcinol adhesive flow into the vessel cell lumens. However they did not relate variations in adhesive penetration with fracture toughness.

Several wood DCB specimen configurations have been used, in addition to Ebewelle's work with contoured solid wood DCBs. River et al. (1989) conducted research with contoured composite DCB's, made from flat-pressed bonded-wood laminates attached to contoured aluminum beams. This development greatly simplified sample preparation; it eliminated the special jigs required to consolidate solid wood contoured beams. While the wood/aluminum composite tapered beams were an improvement, the tapered aluminum was costly and it required chemical etching to form a good bond to the flat-pressed wooden DCB. These problems were eliminated with the development of composite tapered beams made with wood oriented strand board (River and Okkonen 1993). Testing has also been done with composite DCBs using constant tapered beams made from laminated strand lumber (Davalos 1997). The composite tapered beams were effective, but their preparation was nevertheless time consuming, not to mention the fact that the beams required compliance calibration.

In 2001 Gagliano and Frazier published a method using the simple flat DCB; this greatly simplified sample preparation, the benefits of which were found to outweigh the need for real time crack length measurements which are not required with contoured beams. This method of using constant cross-section and non-composite DCB's, which is also employed in this thesis work, makes specimen preparation easier while increasing the number of specimens produced. In a separate work, Gagliano (2001) investigated several different methods for determining the strain energy release rate, *G*, and found the corrected compliance method described by Blackman et al. (1991) to provide the most reasonable results with least variation. Gagliano's research determined that there may be a load rate dependence, recommending that the load rate applied for each cycle be set to the cross-head displacement reached at fracture for the previous cycle. A hysteresis in the load versus displacement profiles was observed, though the reasons for this were not determined.

Using specimen preparation method's similar to Gagliano and Frazier's work, Conrad et al. (2003) used flat wood DCB's to analyze the fracture toughness of various sized PF resin droplets from flexographic printing plates bonding Douglas fir. Interestingly, in their work the beam thickness was lowered to 6.35mm to reduce process induced residual stresses leading to premature bond failure. And starting with a tapered beam on elastic foundation model, though not allowing for foundation rotation as Williams (1989) did, Qiao et al. (1997) compared analytical predictions and FEA models to experimental work, using aspen wood laminated strand lumber tapered DCB's with thick adherend layers of red maple or phenolic fiber reinforced plastic. Experimental work agreed more closely with the FE results than with the Rayleigh-Ritz solution they

studied.

1.6 Work explored

The primary direction of this thesis is towards exploring qualitative and quantitative characteristics necessary for refining and understanding the wood double cantilever beam (DCB) as a valid means for testing fracture energy in wood adhesive bonds. The appropriate specimen width, latewood/earlywood grain distribution influences, significance of adhesive penetration, and system behavior under cyclic loading were investigated. Both epoxy and phenol formaldehyde (PF) impregnated films were used with southern yellow pine (SYP) adherends, providing two systems with different characteristics. This research should be considered an extension of Gagliano's (2001) research into using the same specimen geometry for quasi-static testing.

In Chapter 2 the effect of specimen width on strain energy release rate, G_{Ic}, was investigated experimentally by testing DCB's at varying widths (10 mm, 15 mm, and 20 mm. The analysis of epoxy bonded DCB's was complemented with bulk epoxy toughness measurements using the single edge notched specimen. Quasi-static fracture testing was also performed on SYP adherends bonded with PF films. In Chapter 3 microphotography of stained microtomed specimen cross-sections was used to analyze the adhesive penetration into the adherends for both the epoxy and PF bonded specimens. Also investigated was the difference in penetration depth of the epoxy into earlywood versus latewood growth regions.

In Chapter 4 grain distribution influences were computationally investigated because of the stiffness difference between latewood and earlywood growth and the grain's angle along the length of the beams. The difference between the longitudinal grain elastic modulus and the lengthwise elastic modulus of the beam was calculated for a

range of grain angles. Also investigated were the effects from a grain angle in the x-z plane. Various latewood grain thickness and distributions were examined within reasonable ranges for southern yellow pine. Based on these considerations, another recommendation is made for an appropriate beam width.

Chapter 5 describes the cyclic testing performed using PF-SYP DCB's at 3Hz with a valley to peak load ratio of R = 0.5. Testing was performed under load control in order to maintain a constant load ratio, with both maximum and minimum displacements increased with cycling at constant crack length. The specimens were coated in an oil based aluminum paint and sealed in plastic bags during testing to maintain moisture control.

Chapter 2: Epoxy-SYP DCB and PF-SYP DCB static fracture

2.1 Introduction

The width dependence of epoxy southern yellow pine (SYP) double cantilever beam's (DCB) was experimentally investigated. The specimens were cut to 10 mm, 15 mm, and 20 mm widths. The properties analyzed for width dependence include the critical and arrest strain energy release rate, G_{Ic} and G_{Ia}, respectively; the square of the Pearson product moment correlation coefficient, R^2, from the cube root compliance versus crack length plot; the determined effective stiffness divided by specimen width, $(E_{xx}I)_{eff}/b$; the crack length correction, α; and the beam's calculated macroscopic lengthwise elastic modulus, E_{xx}. The elastic modulus and fracture toughness of the bulk epoxy were also determined using tensile coupons and single-edge notched-beam (SENB) specimens prepared with the same two-stage curing process used to make the epoxy SYP-DCB's.

Past experiments with other substrates (e.g. aluminum, Kinloch and Shaw (1981)) have shown greater G_{Ic} values for smaller widths, leveling down to a constant value as width increases. The determining factor for this behavior is generally associated with the relative proportion of plane strain to plane stress plastic zone volumes. Plane stress plastic zones, prominent on a specimen's edge, are significantly larger than plane strain zones. For this reason narrow specimens have larger plastic zone volumes per unit width, resulting in higher fracture energies. With stiffer adherends such as aluminum, the plastic zone is constrained to be entirely within the adhesive. However wood's comparable softness allows for significant substrate deformation in the vicinity of the crack tip's stress concentration. Because the stress concentrations near the crack tip are

deforming the wood adherend, the wood's orthotropic and non-homogeneous nature will result in complicated stress distributions. One objective of this work was to experimentally determine the point that epoxy SYP-DCB's G_{Ic} cease to decrease with increases in width, if such a point is observable.

2.2 Methods and Materials

Following the process developed by Gagliano and Frazier (2001), southern yellow pine (SYP) double cantilever beams (DCB) were made from machined wood lamina and two separate adhesives: a thin film epoxy NB101 U 0.060 from Newport Adhesive and Composites, Inc. and a phenol formaldehyde (PF) impregnated paper 42209/PGF from Dynea Overlays, Inc., both approximately 250 μm in thickness. SENB fracture specimens and dogbone tension specimens (procedure described below) were made from the same epoxy film using silicone molds.

2.2.1 Wood Lamina Preparation

Clear grain SYP was purchased in the form of 2.4 m to 3.7 m long, 50 mm thick boards, with widths ranging from 150 mm to 300 mm. The boards were cut into 25 cm long sections, and then lines were drawn at 3^o angles against the longitudinal grain as measured from the sides, at least 15 mm apart. A bandsaw was then used to cut free the laminae, with each section yielding one to three laminae, depending on the grain's angle of the starting board. The lamina were then planed down to approximately 12 mm thickness and then placed in an environmentally regulated chamber maintaining a relative humidity of 67% at 20 ^oC, which equilibrated the wood's moisture content to 12% by weight. Variations in initial moisture content caused the time to equilibrate to vary, potentially lasting several weeks. All wood specimens and materials were stored in the equilibration chamber until needed for further processing.

2.2.2 Epoxy-SYP DCB fabrication

After the wood laminae moisture content had equilibrated, the laminae were planed down to a final thickness of 10 mm. The adhesive film was placed between the two laminae, which were oriented to have the grain angle converge at the bondline, as depicted in Figure 2.1. The epoxy laminates were fabricated with three layers of film. The laminate was wrapped in aluminum foil and then placed in a preheated oven. The aluminum foil prevented expelled liquefied epoxy from leaking onto the oven floor and damaging it.

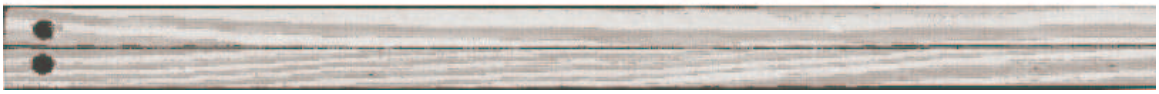

Figure 2.1: A typical wood DCB made from southern yellow pine constructed so the grain converges into the bondline at an approximately 3^{o} angle, with an initial crack and two holes drilled in one end.

When moisture escapes, wood has a tendency to curve in the opposite direction of the growth ring curvature. This characteristic becomes more pronounced as the moisture content in the wood decreases, the rate and level of which is dependent on temperature and atmospheric humidity. For this reason, in order to reduce residual stresses and ensure more consistent bondline thickness, the boards were laid so that their growth ring curvatures were in the same direction. An example of this is shown in Figure 2.2. This ensured that distortions that would have taken place, due to wood drying in the oven during the long curing process, would be in the same direction. The important result being that residual stresses were minimized so that they did not contribute to crack growth, thereby lowering the measured Mode I fracture energy.

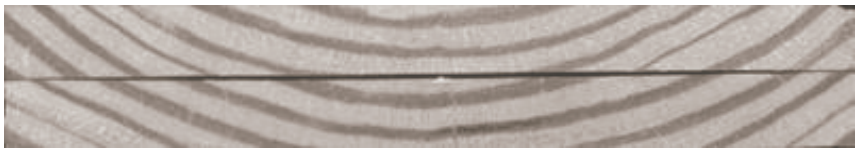

Figure 2.2: End cross-sections of two lamina nested so that the curvature of their growth rings are in the same direction.

The epoxy laminates were centered in the oven under flat steel plates applying an approximate pressure of 3.5 kPa, cured with a two stage curing process: 20 hours at 55^{o}C followed by 3 hours at 100 ^{o}C. The two stage curing process was used to keep epoxy within the bondline by raising the viscosity by partially curing at a lower temperature, so that when the temperature was raised to 100^{o}C to complete the cure, not all the epoxy was expelled from the sides. After curing the laminate, the aluminum foil was removed and the laminate was allowed to cool. The individual beams were cut to the appropriate width using a table saw, with the laminate's outer 10 mm edges being discarded due to avoid edge effects. Specimens 10 mm, 15 mm, and 20 mm wide were machined from an individual epoxy laminate, as depicted in Figure 2.3. This ensured that sample preparation effects were randomized across all test specimens. Holes were drilled in the specimen's starting end. The epoxy-SYP specimens were returned to the environmental chamber for storage. In total, there were sixteen 10 mm specimens, nineteen 15 mm, and seven 20 mm wide specimens.

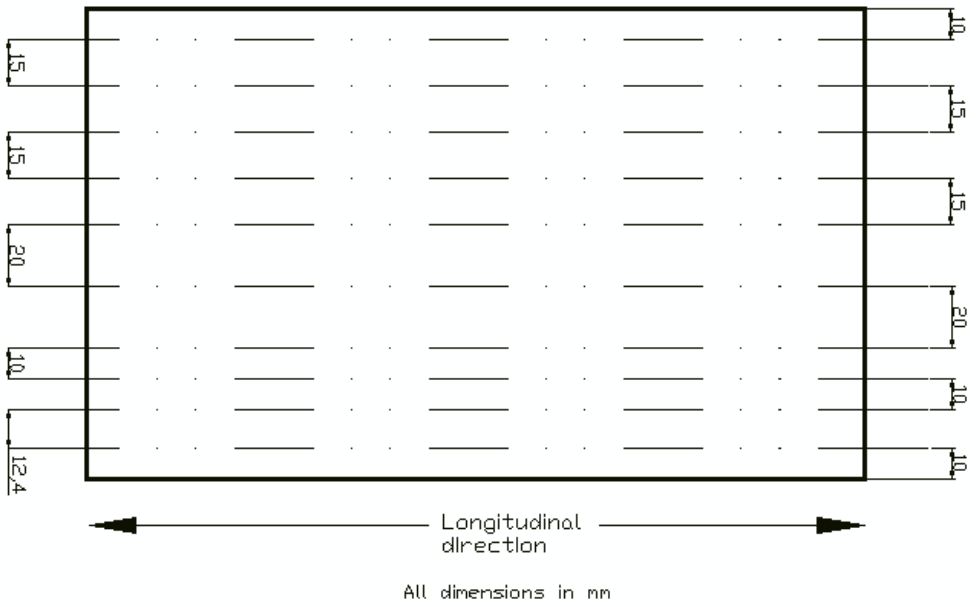

Figure 2.3: An example of the cutting pattern for obtaining different width beam from the same lamination, discarding the outer 10 mm sections.

2.2.3 PF-SYP DCB fabrication

After being planed to 10 mm thickness, the boards were nested together with the same growth ring curvature and grain angle directions, as described earlier. The laminates were wrapped in fresh aluminum foil and centered in a preheated hot press, under 245 kPa at 150^{o}C for 20 min. The pressing time was the optimal time found by Gagliano (2001) with the same adhesive, though he used yellow poplar, a less dense material, pressed at 175^{o}C under 965 kPa. The phenol formaldehyde impregnated paper film is approximately 250 μm thick with no tackiness at room temperature. Upon heating the paper substrate remains solid, however the impregnated phenol formaldehyde flows into the bond interface.

Within an hour and a half of being removed from the hot press, the specimens were cut to a width of 20 mm with a tablesaw, holes were drilled in the end. The specimens were then immersed entirely in oil based aluminum paint, removed and allowed to air dry for approximately 24 hours. The specimens were placed in two plastic

Ziploc bags for storage to maintain their moisture content. Over twenty specimens were prepared, however only three were used in the quasi-static DCB test.

2.2.4 DCB specimen pretest preparation

Before testing the epoxy and PF-SYP DCBs, a ruler tape was pasted along the side, directly underneath the bondline, with the measurement starting at the center of the fixture holes. White-colored typographic correction fluid was painted along the bondline in order to make the crack more visible to the naked eye. Testing was performed within 30 minutes of applying the correction fluid. A clamp was applied at approximately 50 mm past the fixture holes in order to restrict crack growth beyond that point while a sharp wedge was tapped into the bondline to make an initial crack.

2.2.5 Bulk epoxy tensile dogbone preparation

To minimize void formation the dogbone tensile coupons, were cured under vacuum (< 34 kPa) in silicone rubber molds. Curing was conducted with the same two-stage heating process as for the epoxy-SYP DCB's: 20 hours at 55^{o}C followed by 3 hours at 100^{o}C. Leaks did cause vacuum pressure to decline, but not before the material had vitrified within each stage. For this reason a vacuum was used to bring pressure below 34 kPa again before devitrification in stage 2.

Approximately 0.5 mm of excess material was removed from each side using rotating drum and unidirectional circular wall sanders. All sides of the dogbone specimens were flattened for constant rectangular cross-sections and finally exposed to sanding along the length to ensure scoring across the width did not contribute to early specimen failure. Five specimens were prepared ranging in thickness from 1.93 mm to 4.23 mm, with an average width of 12.9 mm and length of 101 mm. All testing and specimen preparation was based on ASTM D638-95

2.2.6 Bulk epoxy SENB preparation

The same thin film epoxy described above was cut into strips and laid within a silicone rubber mold. The epoxy was then cured at 55^{o}C for 20 hrs followed by 100^{o}C for 3 hrs, the same two stage curing process used for making the DCB specimens. A solid 200 mm long rectangular block was produced, with a cross-section of 25 mm by 25 mm. The specimen dimensions were chosen in accordance with ASTM D 5045 – 95. A table saw was used to cut the block into two strips 6 mm thick and 12 mm wide. A bandsaw was used to cut 4 blocks from each strip, and a vertical belt sander employed to flatten off all edges to the approximate dimensions of 49.3 mm length, 5.6 mm thickness (B), and 11.2 mm width (W). A guiding cut was made for a 60^{o} file to create a triangular notch approximately 2/3 B in depth.

Following a method proposed by Dillard et al. (1993) using an eccentric compressive load to aid in pre-cracking a SENB, the specimen was loaded in a vice with small pins placed at the base of each end. This off-center loading produced bending, with tensile stress at the notch tip and compressive stress below, as shown in Figure 2.4. When a razor blade was tapped into the bottom of the notch, the tensile stress aided crack growth initiation, while the compressive stress helped prevent crack overextension. Though tapping was stopped when the ratio of natural crack length, a, to width, W, driven by the blade appeared to reach a/W = 0.5, as measured from the side, actual internal crack length was determined from the fractured surface using a microscope. Crack extensions were not all straight, so an estimated average of these lengths was used, acquired when validating the specimen, as described below.

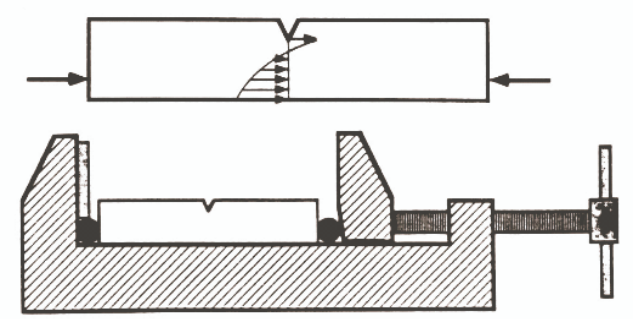

Figure 2.4: Graphic showing eccentric compressive loading and resulting stress distribution on SENB, showing the specimen length and width (Dillard et al. 1993)

2.2.7 Bulk epoxy tensile test methods

Prior to loading, the specimen effective length, and the rectangular cross-sectional dimensions were measured. The specimens were secured in an Instron 4204 testing machine, fitted with an extensometer, and loaded at an effective strain rate of 1% per minute until fracture. Load was measured with a 1 kN load cell. All time, displacement, and loads were recorded by the controlling computer. Strain was taken to be the extensometer displacement divided by the original effective length; stress was taken to be the measured load divided by the cross-section's original area.

2.2.8 Bulk epoxy SENB test methods

To ascertain the fracture toughness of the neat epoxy, neat epoxy single edge notch beam (SENB) specimens were loaded in a device that applied Mode I loading through three point bending, with an extensometer measuring displacement, using the method described in ASTM D 5045 – 95. The specimens were loaded at 1mm/min in an Instron 4204 testing machine. Load was measured with a 1 kN load cell. All time, displacement, and loads were recorded by the controlling computer.

2.2.9 Epoxy-SYP DCB and PF-SYP DCB quasi-static DCB testing methods

All DCB specimens were tested using the method refined by Gagliano (2001), which was adapted from ASTM D3433-93 for bonded metal DCBs. The beams were closed after each crack extension arrested. To ensure the crack opening rate remained

relatively constant for each cycle, the crosshead displacement rate was set so that the previous cycle's maximum displacement would be reached within one minute. With each loading cycle, the crack length was measured and the compliance was determined from the linear region of the load versus displacement plots as the displacement was increasing.

2.3 Results and Discussion

2.3.1 Bulk epoxy tensile testing results

Table 2.1 shows the yield stress, yield strain, and Young's modulus for each specimen. Using the 0.2% offset strain method, the yield point was determined to be the intersection between the data and a straight line, whose slope was the obtained modulus, offset to $\varepsilon = 0.002$, as shown in Figure 2.5. However specimen 1 was deemed invalid based on a prominent void and inexplicable smooth region in the fracture surface when all other specimens showed rough surfaces without voids. A yield point was not obtained for specimen 3 because fracture occurred before the expected intercept point. Each specimen demonstrated brittle failure with very little elongation, with fracture surfaces perpendicular to the loading direction, indicating no shear failure.

Table 2.1: Modulus of elasticity, yield strength and yield strain from tested tensile coupons, with the average (AVG), standard deviation (STD), and coefficient of variation (COV) values.

Specimen #	*E*, GPa	Yield Stress, MPa	Yield Strain
1			
2	2.28	36.64	0.0181
3	2.42		
4	2.66	37.89	0.0163
5	2.63	40.27	0.0173
Avg	2.50	38.27	0.0172
Std	0.18	1.84	0.0009
Cov	0.07	0.05	0.0534

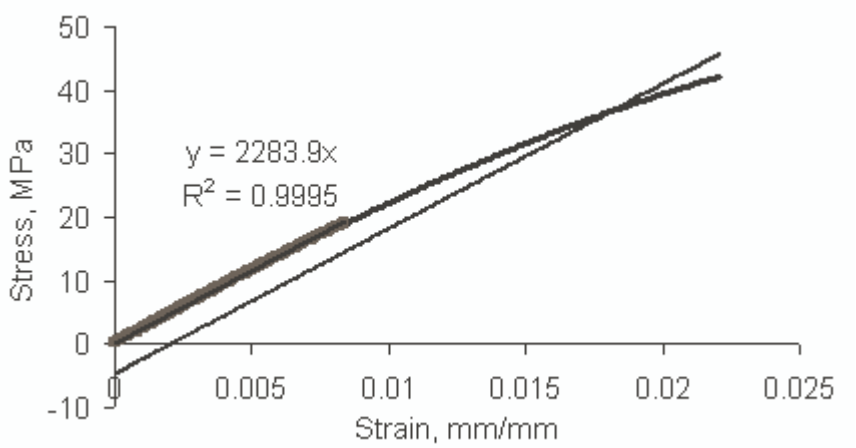

Figure 2.5: Stress strain curve for a typical bulk tensile coupon, showing the offset line used to determine yield point.

2.3.2 Bulk epoxy SENB fracture testing results and discussion

According to ASTM D 5045 – 95, if the material to be tested is supplied in the form of a sheet, the specimens should be cut so that the specimen thickness is the sheet thickness, in order to optimize material use. This variability in specimen dimensions allowed greater freedom in machining the specimens to the chosen dimensions. However the use of such an arbitrary thickness must be justified by proving the results meet the ASTM test method's validity requirements. A preliminary fracture toughness value, K_Q, was calculated using the maximum load sustained, $P_{Q,}$ for:

$$K_Q = (P_Q B W^{1/2}) f(c)$$
$$f(x) = 6c^{1/2} \frac{1.99 - c(1-c)(2.15 - 3.93c + 2.7c^2)}{(1+2c)(1-c)^{3/2}} \qquad \textbf{2.1}$$

where B is the specimen thickness, W the specimen depth, and $c = a/W$, where a is the initial crack length measured to include the notch and induced crack. The ASTM standard specifies that if the difference between the shortest and the longest initial crack length distances within individual specimens is greater than 10%, then the specimen is considered invalid. Analyzed under a microscope, all specimen crack extensions were

shown to be sufficiently uniform across the width. The specimen is also considered to be invalid if the size criteria are not satisfied:

$$B, a, (w-a) > 2.5(K_Q / \sigma_y)^2 \qquad \textbf{2.2}$$

where σ_y is the yield stress obtained from the tensile tests. These criteria exist to ensure that the crack tip's process zone is not influenced by the specimen's size or stress at the loading points. All specimens met the necessary criteria, so the K_{Ic} value was taken to be the calculated K_Q from each specimen.

As can be seen in Figure 2.6, the SENB load vs. displacement curves are almost perfectly linear, with a small decrease in slope immediately prior to fracture corresponding with crack growth initiation. Frequently initial displacements showed increases in slope, which might be attributable to compliance in the Instron's load train. For this reason, early displacements weren't used in calculating compliance.

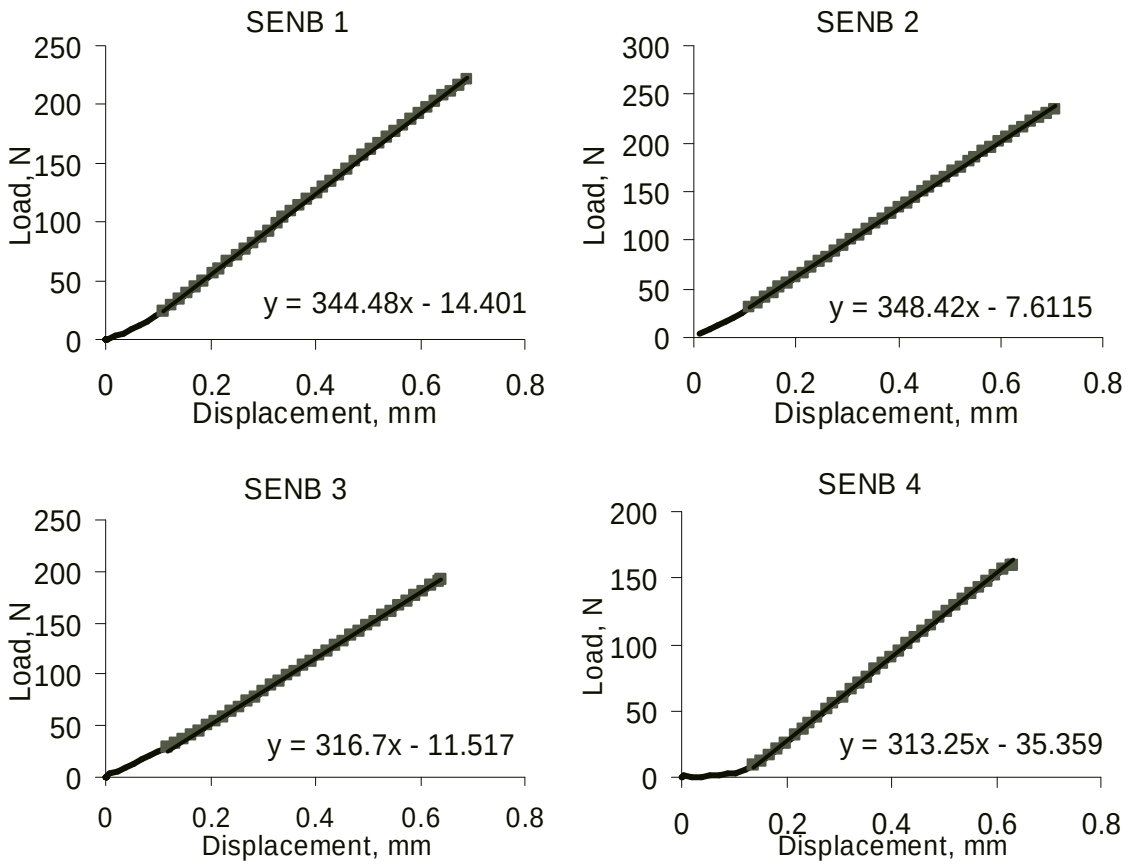

Figure 2.6: Load vs. Displacement curves for four SENB specimens showing regions of constant slope

Figure 2.7 shows the specimen's K_{Ic} values plotted against the *a/W* ratios. Five specimens fall outside the ASTM recommended $0.45 < a/W < 0.55$ range. The average *a/W* ratio was 0.46, with a COV of 9%. However, it can be seen that those which fall outside of the range do not deviate greatly from the average in K_{Ic} value of 1.18 $MPa \cdot m^{1/2}$ with a COV of 9%.

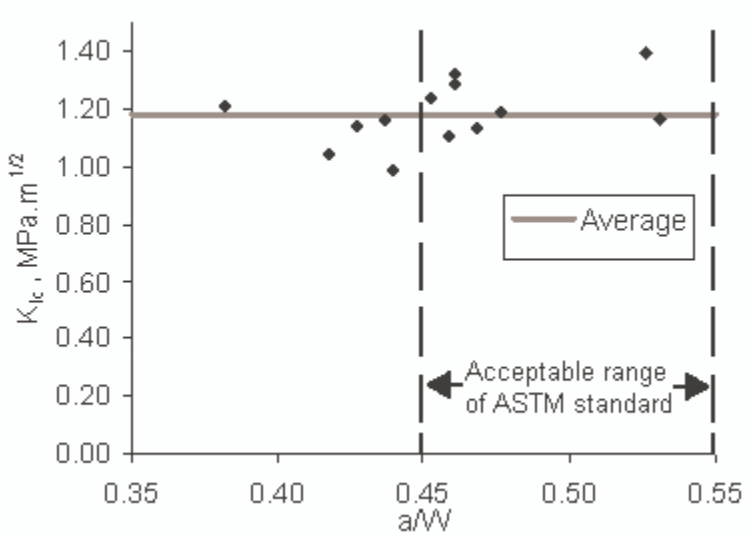

Figure 2.7: K_{Ic} **vs.** a/W**, with an average of 1.18 MPa.m$^{1/2}$ and all specimens considered valid.**

2.3.3 Epoxy-SYP DCB Results

Shown in Figure 2.8 are load versus displacement profiles from several specimens, labeled with their respective widths. In total, there were sixteen 10 mm specimens, nineteen 15 mm, and seven 20 mm wide specimens.

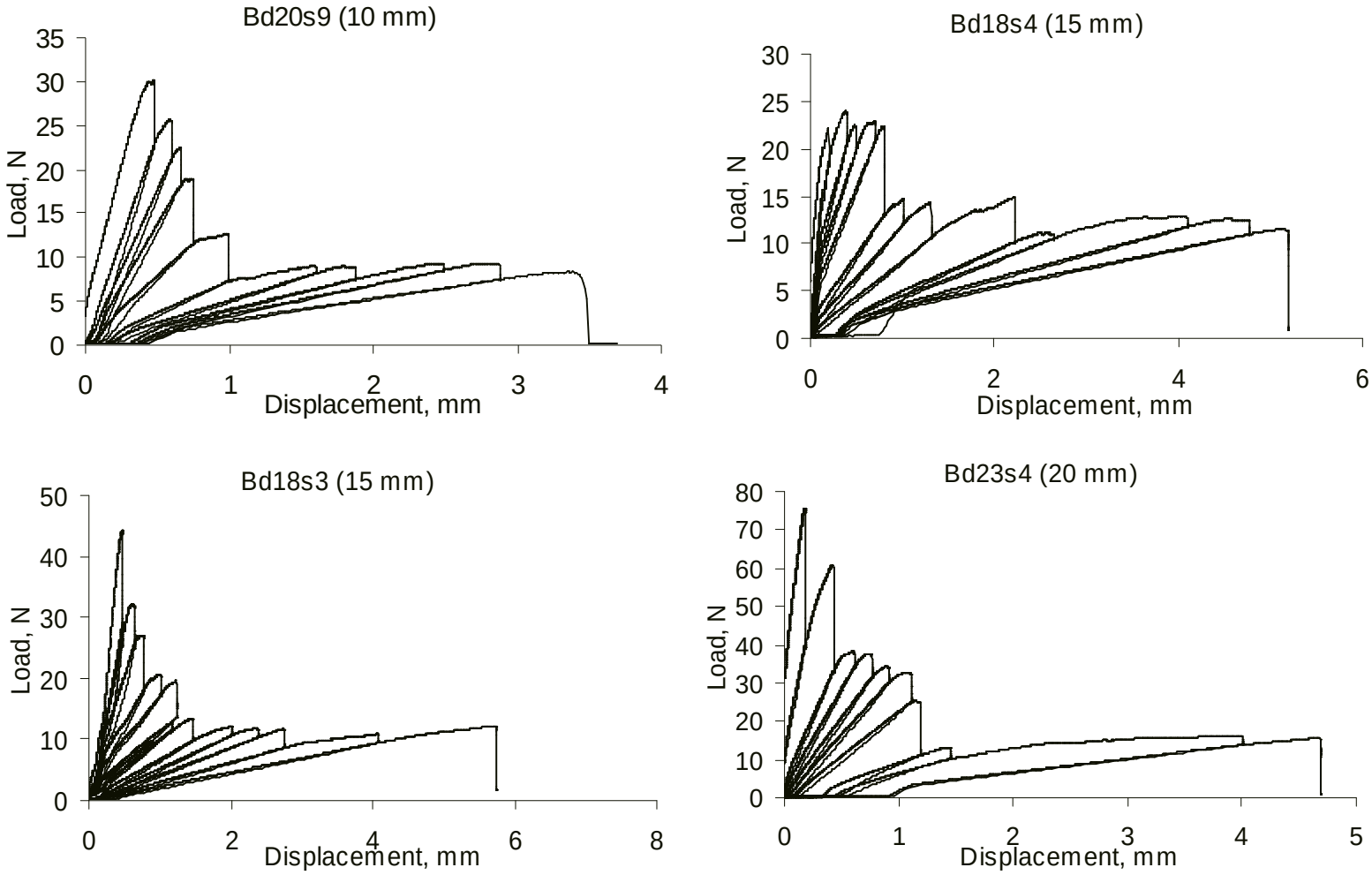

Figure 2.8: **Representative load vs. displacement plots for epoxy-SYP DCB specimens Bd20s9 (10 mm), Bd18s4 (15 mm), Bd18s3 (15 mm), and Bd23s4 (20 mm).**

Hysteresis was observable between iso-crack-length loading and unloading displacements. The hysteresis effect is considered to be negligible; loading curves approaching crack initiation are linear, meaning the assumptions for deriving G_{Ic} are generally valid.

Figure 2.9 shows the cube root compliance, C, versus crack length plots with linear trend line fits, used to acquire effective stiffness, $(E_{xx}I)_{eff}$, and crack length correction, α, as described in Chapter 1. The plots in Figure 2.9 are from the same specimens used to create Figure 2.8.

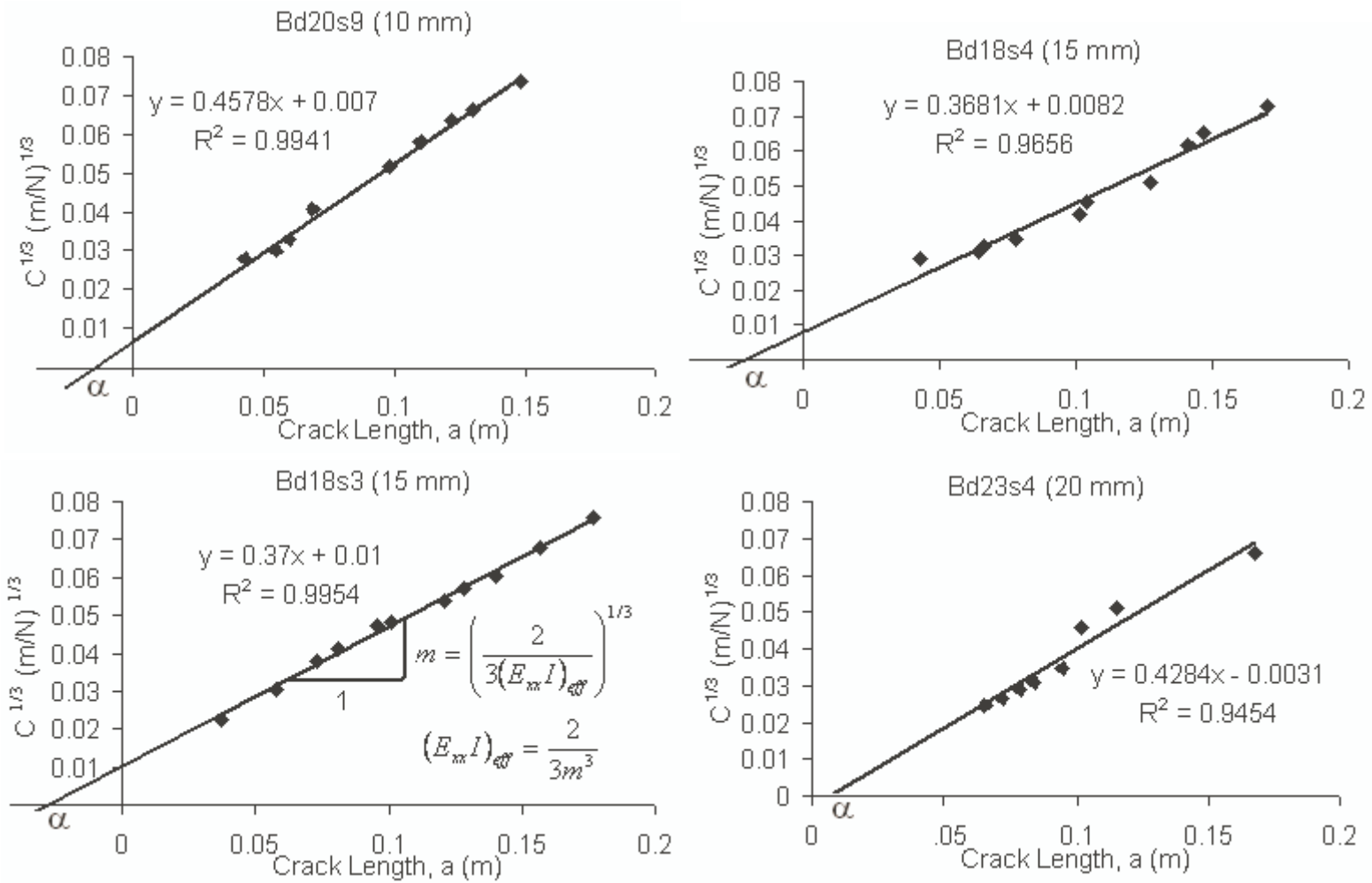

Figure 2.9: **Typical cube root compliance, $C^{1/3}$, vs. crack length, a, for epoxy-SYP DCB specimens Bd20s9 (10mm), Bd18s4 (15 mm), Bd18s3 (15 mm), and Bd23s4 (20 mm).**

Figures 2.10 and 2.11 present the average critical and arrest strain energy release rate, G_{Ic} and G_{Ia} respectively, from each specimen plotted against the actual specimen width. Also shown are the averaged G_{Ic} values from the 10 mm, 15 mm, and 20 mm groupings. The critical loads are considered too low (compared to other adhesive wood DCB systems) to cause the 10 mm beams to be influenced by plane stress plastic zones. Assuming Equation 2.3 for cohesive cracks in bulk adhesives from Kinloch and Shaw (1981) is a valid estimation for the epoxy SYP-DCB specimens, a typical plastic zone size, r_p, is 134 μm, or approximately 50% to 70% the bondline thickness, where E_a is the epoxy modulus of 2.5 GPa, G_{Ic} the epoxy fracture energy of 493 J/m^2, and σ_{yld} the epoxy yield stress of 38.3 MPa. If the loads were greater, the plastic zone size would be greater, extending the crack tip yield zone into the wood adherends. And considering that most cracks were interfacial, not cohesive, the stress concentrations most likely did extend into the soft wood adherends. Regardless, the amount of scatter obviously decreases as width increases, with 55%, 42%, and 28% coefficients of variation for the 10 mm, 15 mm and 20 mm widths, respectively.

$$r_p = \frac{1}{2\pi}\frac{E_a G_{Ic}}{\sigma_{yld}^{\ 2}} \qquad \textbf{2.3}$$

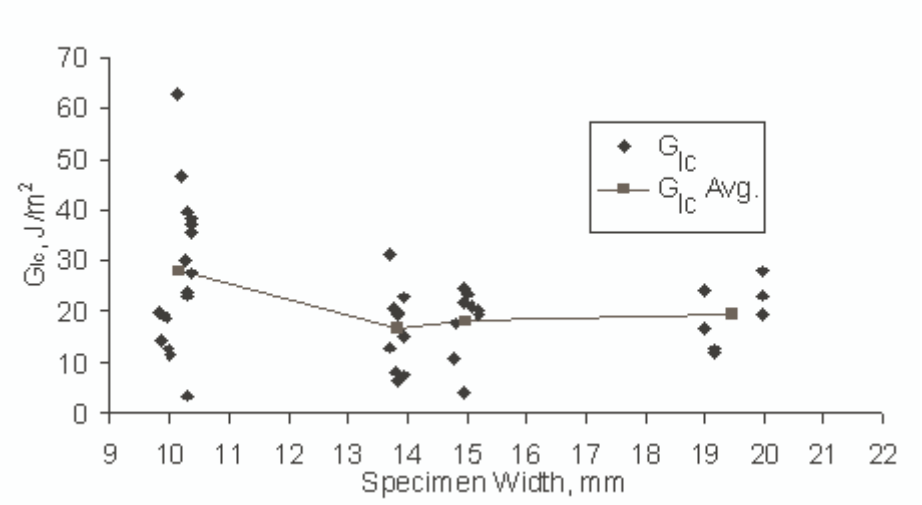

Figure 2.10: Critical strain energy release rate, G_{Ic}, plotted as a function of width.

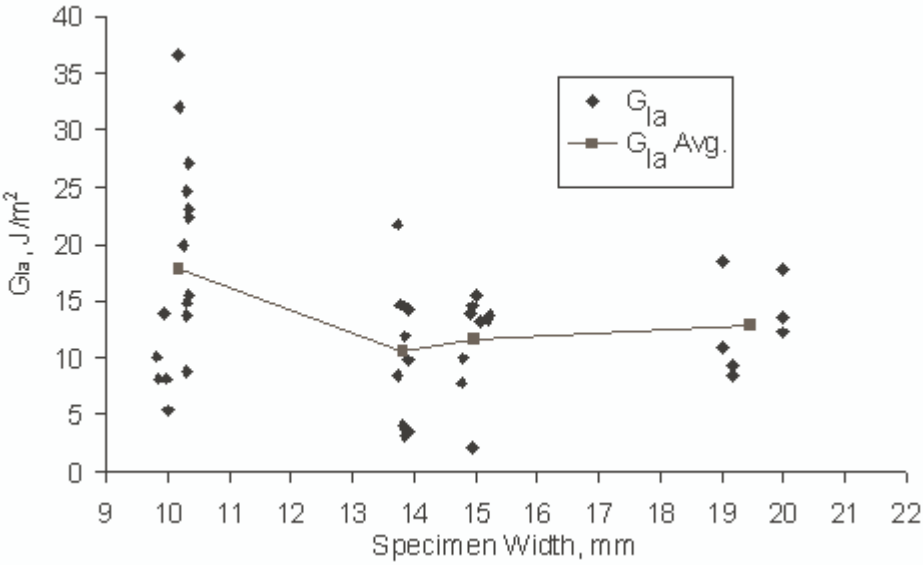

Figure 2.11: Arrest strain energy release rate, G_{Ia}, plotted as a function of width.

There may be several reasons for the decrease in scatter with increases in specimen width. It should be noted that specimens from each width group were produced from several different laminations, with a lamination producing several specimens of different widths. This precludes the possibility that scatter is dependent on the batch from which the specimens originated. One hypothesis for decreased scatter with

increased width combines the facts that the epoxy showed superior adhesion and deep penetration into earlywood regions than latewood regions, and that wider specimens were more consistent in the proportion of growth types exposed on the substrate.

The width dependence of four different indicators was investigated. The cube root of compliance versus crack length linear fit correlation coefficient, R^2; the effective stiffness $(E_{xx}I)_{eff}$ divided by width, b,; the macroscopic lengthwise elastic modulus, E_{xx}, calculated from Equation 2.4; and the crack length correction, α, were all plotted against specimen width in Figures 2.12 to 2.15. Data points come from each from each specimen are plotted against the specimens width, with three statistical outliers removed.

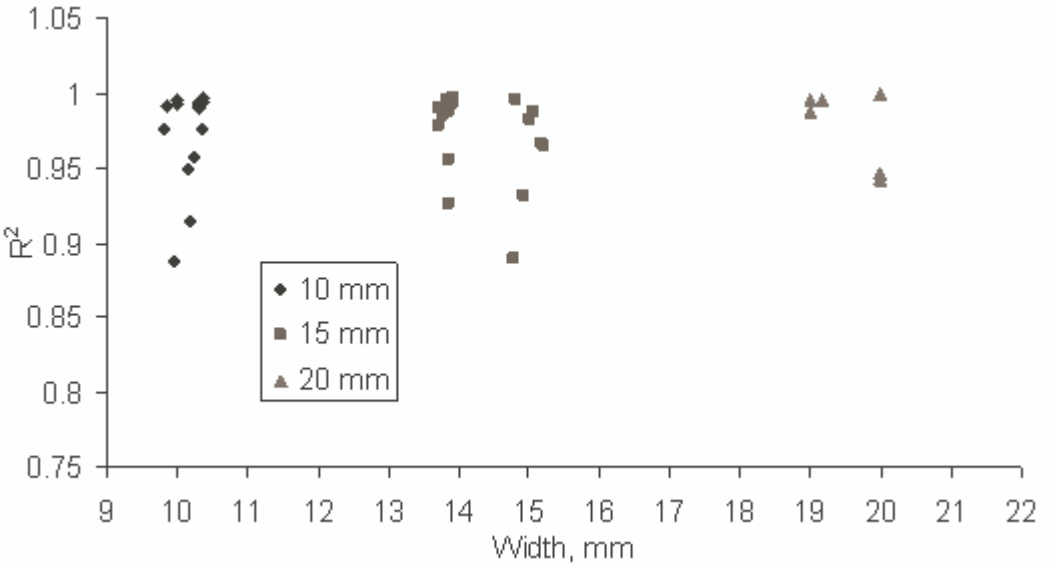

Figure 2.12: The cube root compliance versus crack length linear fit correlation coefficient, R^2, plotted against specimen width.

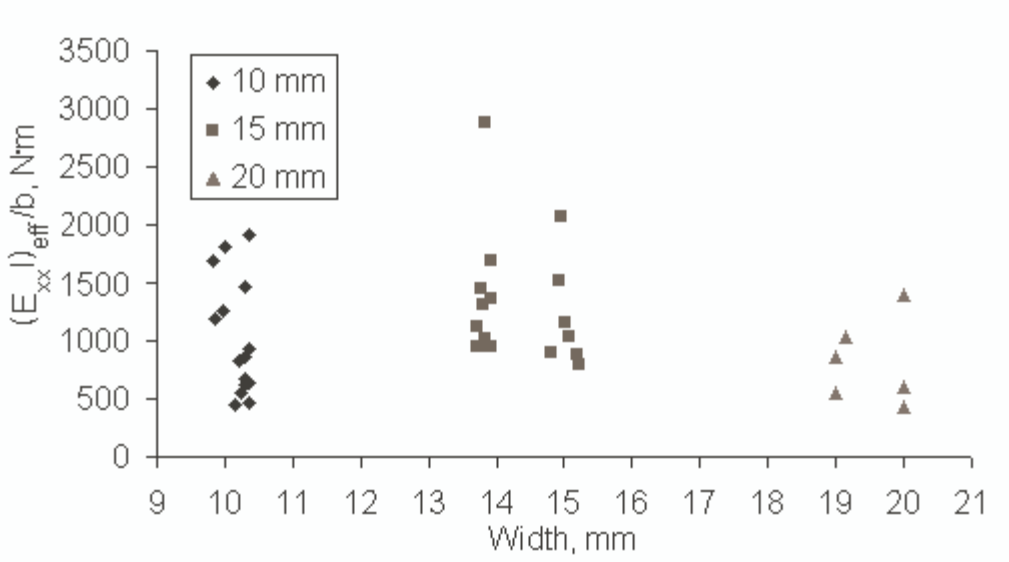

Figure 2.13: **The effective stiffness $(E_{xx}I)_{eff}$ divided by width, b, plotted against specimen width.**

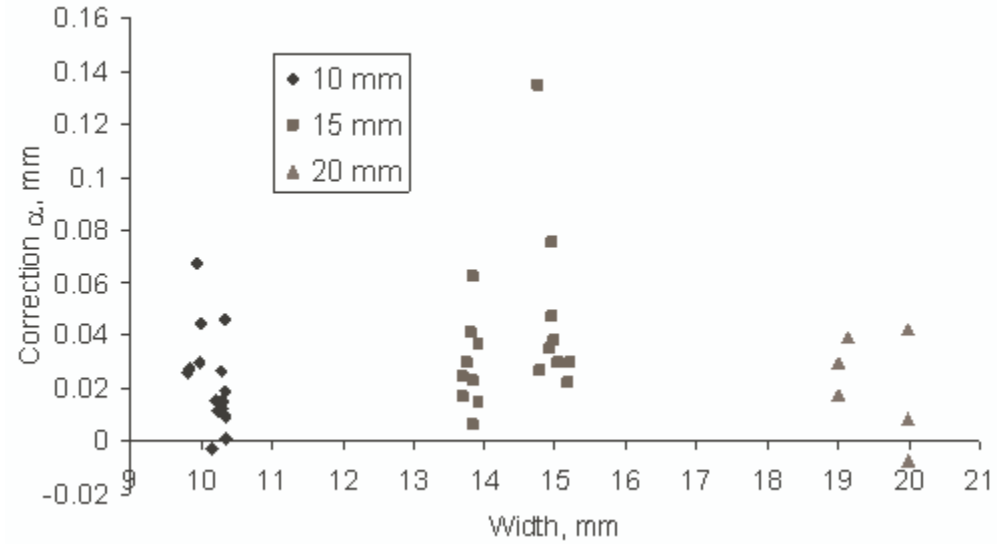

Figure 2.14: **The crack length correction, α, plotted against specimen width.**

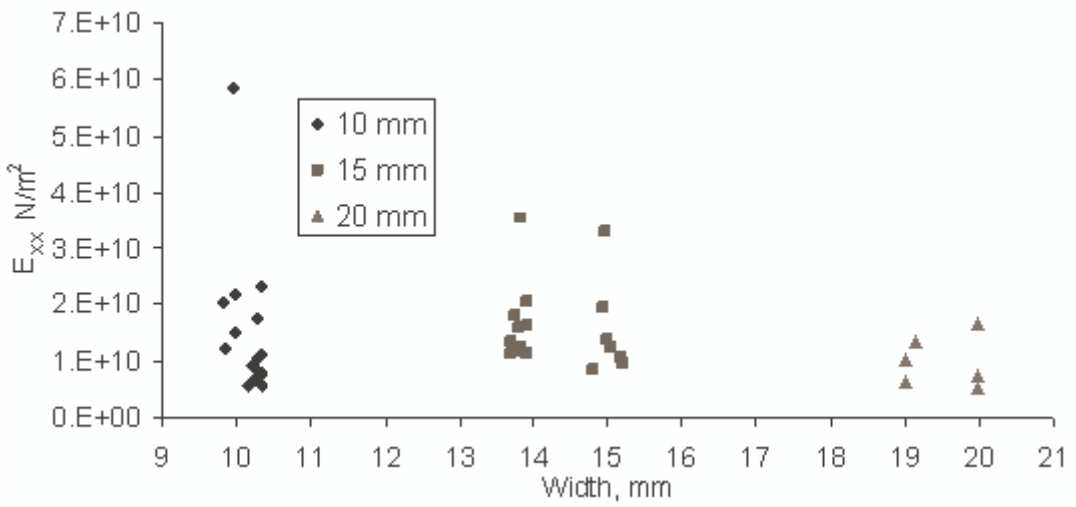

Figure 2.15: The macroscopic lengthwise elastic modulus, E_{xx}, calculated from Equation 2.3, plotted against specimen width.

As discussed earlier, the proportion of earlywood to latewood is more likely to be consistent in wider specimens. The consistency in the proportion of earlywood to latewood within a specimen could influence the scatter of the R^2 value. And the scatter in values of the beam effective stiffness and experimentally determined elastic modulus, E_{xx}, will be dependent the differences between specimens. Considering the sizes of SYP growth rings (2-5 mm), narrower specimens are plausibly more likely to have significant differences in the proportion of growth types, and therefore significant differences in mechanical properties. However there is no apparent width dependence for any of these values in terms of scatter or data ranges. This is significant because the critical and arrest strain energy release rate values showed a decrease in scatter with an increase in width. If any of these indicators had shown similar behavior, they would have given a clue as to the cause for the G_{Ic} and G_{Ia} behavior.

Figure 2.16 presents effective stiffness $(E_{xx}I)_{eff}$ versus correction α, for the three different width groups. As would be expected from Equation 2.4 from Blackman et al. (1991), there is a clear cubic dependence on α, where h is the beam height. However, no

width group stands out as being different.

$$E_{xx} = \frac{1}{C}\frac{8(a+\alpha)^3}{bh^3} \qquad \textbf{2.4}$$

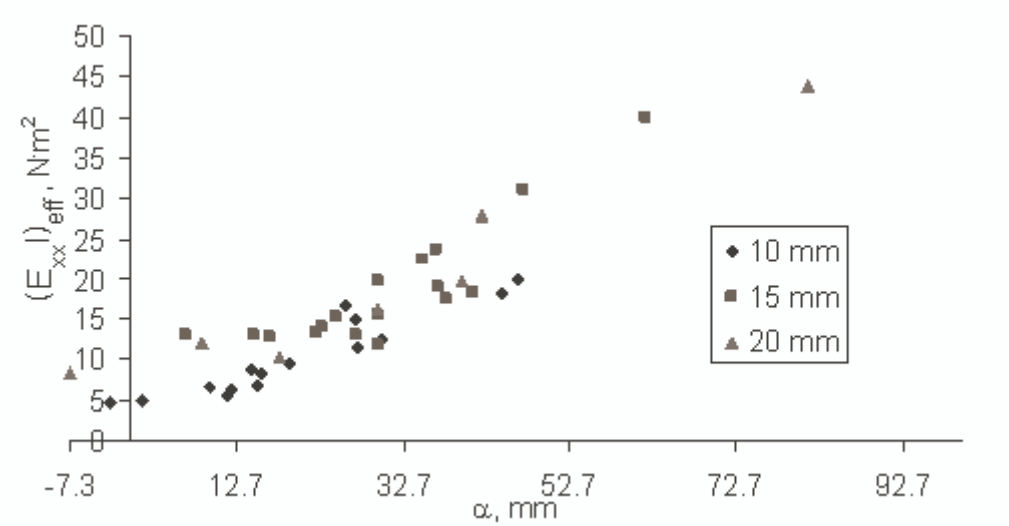

Figure 2.16: Effective stiffness, $(E_{xx}I)_{eff}$, (determined from the cube root compliance versus crack length plot) plotted as a function of crack length correction, α.

2.3.4 Epoxy-SYP DCB and epoxy SENB Discussion

Several factors influence the epoxy-SYP failure behavior, such as bondline thickness, adhesive penetration, and the adhesive's critical fracture energy. The bondlines were sufficiently thick to preclude concerns about bondline starvation causing the low fracture energies. So although SENB specimens have stress distributions different from those seen in interfacial failure, an epoxy with low fracture toughness would explain the low G_{Ic} values obtained in the epoxy-SYP DCB tests.

Equation 2.5 was used to convert the SENB K_{Ic} values to G_{Ic}, where E_a is the epoxy's Young's modulus, and ν the Poisson's ratio. Though the epoxy's Poisson's ratio was not experimentally determined, an assumed value of ν = 0.35 produced 493 J/m^2. These values are well above the epoxy-SYP DCB fracture average value of 20 J/m^2.

$$G_{Ic} = \frac{(1-\nu^2)K_{Ic}{}^2}{E_a} \qquad \textbf{2.5}$$

Though the epoxy fails in brittle fashion under tension, its fracture toughness is sufficiently great to preclude cohesive failure from being the cause of the DCB's low fracture toughness. The reasons for the low wood-epoxy DCB fracture toughness remain unknown. Several possible explanations have been hypothesized, but nothing has been proven. Perhaps a combination of reasons contributes to the final lower toughness. One explanation involves the preferential adsorption of one of the epoxy reactants into wood, in which case the epoxy stoichiometry could be altered away from the optimum with deleterious effects in the interphase. An interfacial crack (which was the dominant failure mode) would pass through a material of perhaps lower toughness. And although the cracks were mostly interfacial, typically a layer of epoxy remained on the failed side. Another explanation involves the absorbed epoxy filling and stiffening the substrate around the crack tip. The average elastic modulus for the epoxy is approximately two times greater than SYP's bulk radial direction elastic modulus, and 4 times greater than the tangential direction modulus, though about $1/5^{th}$ the longitudinal stiffness. If the wood cells were to remain unfilled, stresses around the crack tip could have been dissipated in the softer porous material. With the cells filled with stiff epoxy, stress fields at the crack tip are greater for the same beam loading/displacement. This explanation by itself is not sufficient to explain the extremely low fracture toughness values in comparison to the neat epoxy. In a SENB specimen the crack tip is certainly surrounded by stiff epoxy. The penetrated region of a DCB is a softer composite of wood and epoxy. If stiffness of the surrounding material were the sole criteria for lower fracture toughness, the SENB specimens would show the lowest toughness.

2.3.5 PF-SYP DCB Results and Discussion

In order to ascertain the critical fracture loads at different crack lengths, displacement controlled quasi-static fracture tests were performed on three PF-SYP DCBs. The G_{Ic} values from individual crack lengths ranged from below 200 J/m^2 in one specimen to above 360 J/m^2 in another, with an approximately 10% coefficient of variation for each specimen. The average G_{Ic} value for the three specimens was 272 J/m^2, with individual G_{Ic} and G_{Ia} plots against crack length given in Figure 2.17. The plots of the cube root of compliance, *C*, versus crack length, *a*, had very good linear fits. The square of the Pearson product moment correlation coefficient, R^2, was over 0.98, as shown in Figure 2.18. Data from all specimens, taken as a whole, does not show trends, such as increasing fracture energy values with increasing crack length.

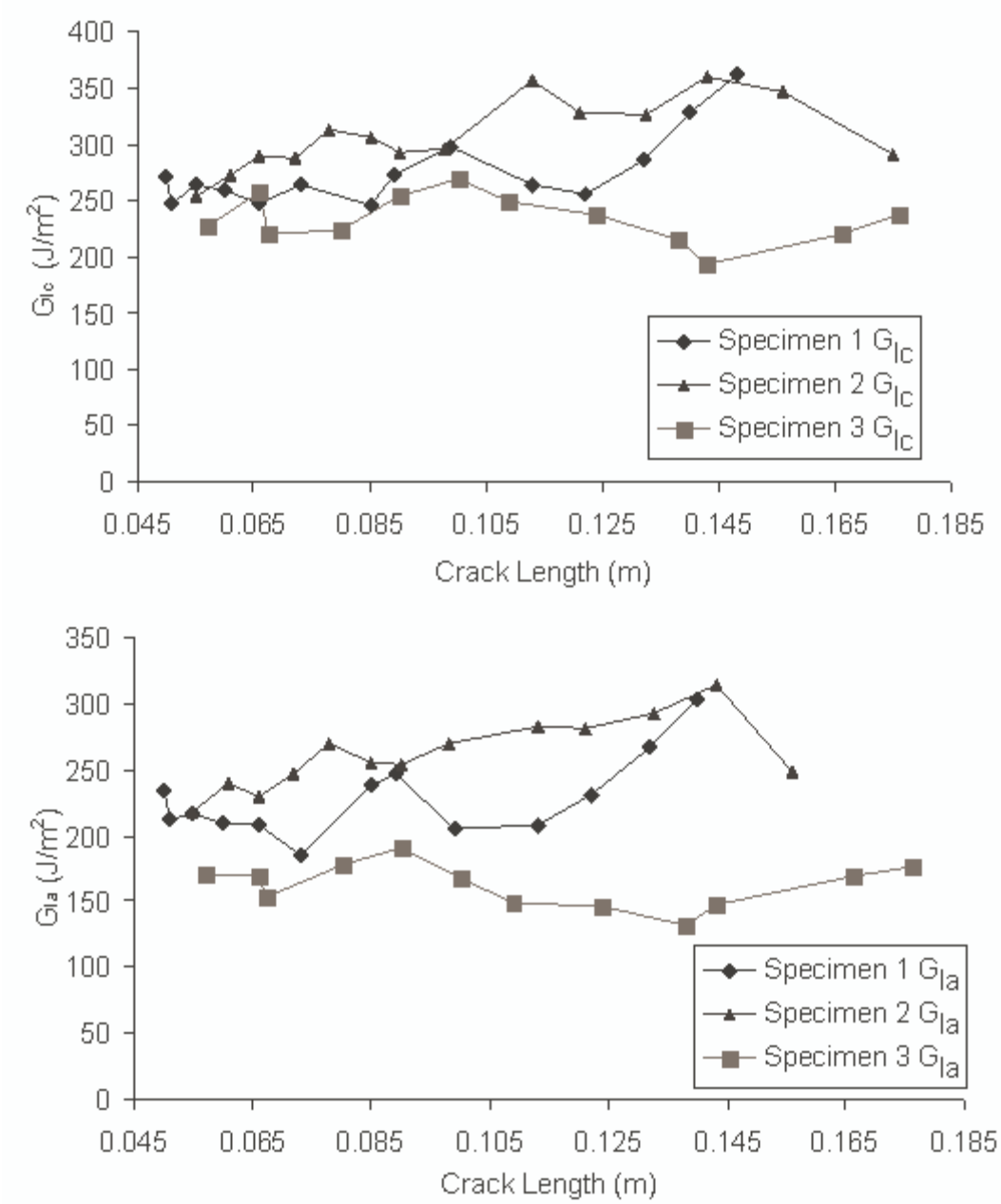

Figure 2.17: **The plots of critical and arrest fracture energies, G_{Ic} and G_{Ia}, against crack length for quasi-statically loaded PF-SYP DCB.**

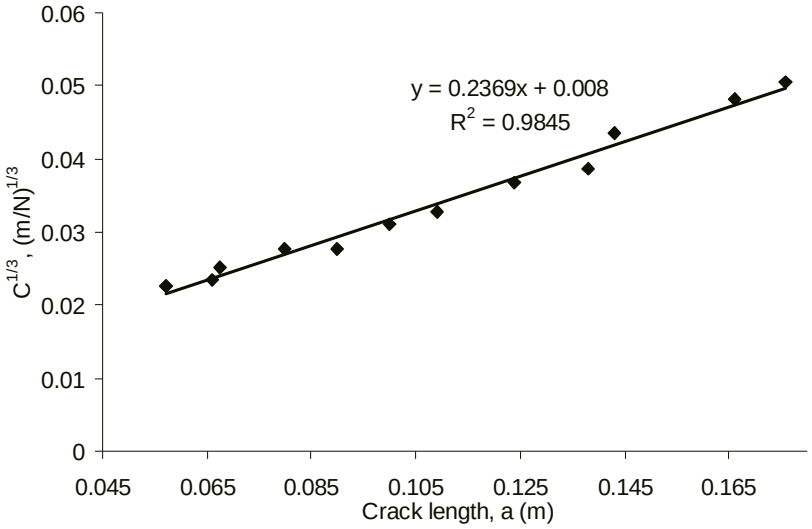

Figure 2.18: A plot of the cube root of the DCB's compliance against crack length for a typical quasi-statically loaded PF-SYP DCB.

In Figure 2.19 the critical loads from the three quasi-statically tested PF-SYP DCBs are plotted as a function of crack length. Interestingly, as can be seen by comparing Figure 2.17 and 2.18, a specimen may have a higher critical load but lower critical fracture energies compared to other specimens. This is due to variations in crack length correction, α, which ranged from 17 mm to 33 mm. In addition to variation between specimens in critical loads at similar crack lengths, none of the specimens show a smooth decline, but rather a waviness as crack length increased. The waviness could be due to local variations in beam properties causing the effective crack length at individual points to differ from the values used based on the overall crack length correction for the entire specimen. The grain angle converging at the bondline will cause variations in the cross-section stiffness along the specimen length. This could potentially lead to variations in the critical fracture load, as will be discussed in a later chapter.

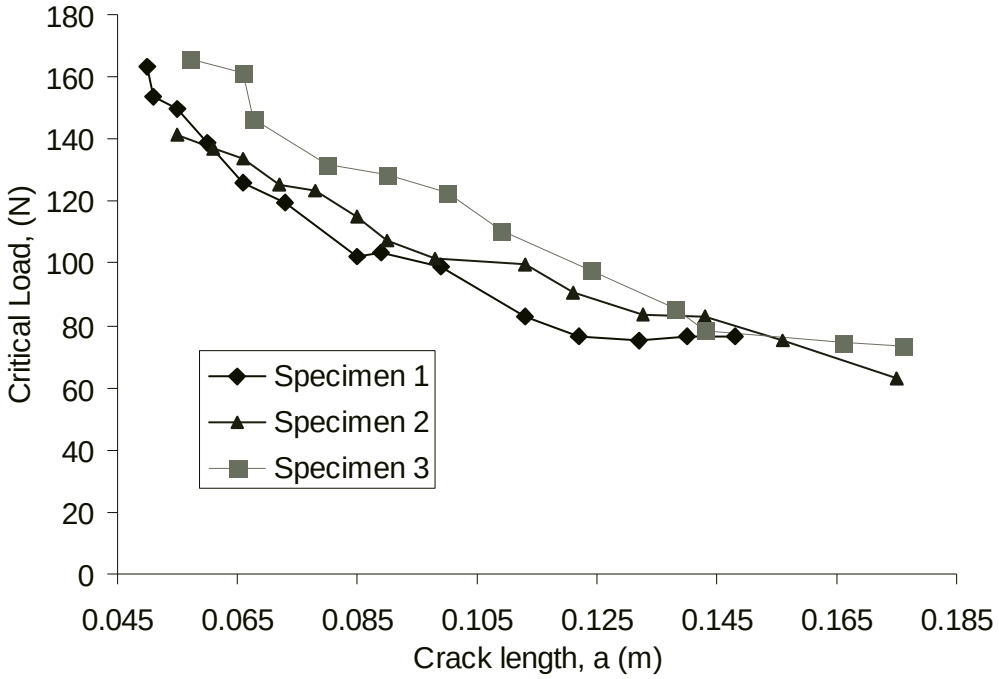

Figure 2.19: Critical load versus crack length from three typical quasi-statically loaded PF-SYP DCB specimens

2.4 Conclusion

The epoxy-SYP DCB's of 10 mm, 15 mm, and 20 mm widths were tested under quasi-static monotonic loading to investigate width dependence for the following properties: the critical and arrest strain energy release rate, G_{Ic} and G_{Ia} respectively; the square of the Pearson product moment correlation coefficient, R^2, from the cube root compliance versus crack length plot; the determined effective stiffness divided by specimen width, EI/*b*; the crack length correction, α; and the beam's calculated average elastic modulus. The only significant dependence was apparent in the statistical scatter of G_{Ic} and G_{Ia}, though the average values were approximately the same and much lower than expected. The scatter was found to decrease as specimen width increased. This indicates specimens should be fabricated with a width of at least 20 mm. PF-SYP DCBs were tested under quasi-static monotonic loading. These specimens were found to have much higher fracture energies than the epoxy-SYP DCB's.

The epoxy's elastic modulus and fracture toughness were experimentally determined to investigate reasons for the epoxy DCB's low fracture energy. The epoxy was found to have a high fracture toughness, K_{Ic}. Under pure tension the epoxy fails in a brittle fashion, with an elastic modulus twice the modulus of SYP's radial grain direction. Plausible reasons for the low DCB fracture energy were given. A cohesive failure crack tip plastic zone size for the epoxy-SYP DCB was estimated to be between 50% and 70% the bondline thickness. The significance and validity of this approximation is questionable considering most failures were interfacial, not cohesive, and the mechanical properties of the epoxy near the interface is uncertain.

Chapter 3: Adhesive penetration analysis

3.1 Introduction

Typically in the formation of a wood-adhesive bond, the adhesive wets and then flows over the wood surface and into the cell lumens. This adhesive penetration promotes mechanical interlocking and the reinforcement of damaged surface cells; it also increases the surface area for adsorption and possible covalent bonding. Depending upon the level of penetration, an interphase comprised of adhesive and wood may be formed, creating a composite layer with mechanical properties different from those of the bulk adhesive and wood. This composite layer could serve to increase the stress applied at the crack tip in a bonded fracture specimen, or act as a toughened layer preventing crack growth into the adherend. Ebewele (1980) noted that for contoured double cantilever beams (DCBs) made from maple bonded with filled phenol-formaldehyde (PF), deep adhesive penetration prevented crack growth into the wood adherend, while bond's with shallow penetration showed crack growth into the adherend.

In this chapter southern yellow pine (SYP) bonded with epoxy and PF is examined by fluorescence microscopy. The epoxy mean effective penetration and maximum penetration depths are determined for earlywood and latewood growth regions. Different dye and fluorescent light combinations are explored for PF-SYP systems. Also investigated is the penetration depth of the oil-based aluminum paint used to cover the PF-SYP DCBs, as described in section 2.2.3. This paint penetration is studied to determine the likelihood of the paint significantly altering the bond.

Photomicrography of dyed microtomed surfaces under fluorescent light provides a means for characterizing adhesive penetration. This reveals adhesive wetting and penetration, providing qualitative insights into the nature of wood adhesion and the bond

fracture resistance.

3.2 Materials and methods

3.2.1 Epoxy and PF wood bonds and dyes

The samples in this work came from the double cantilever beam (DCB) fracture specimens discussed in Chapter 2. Southern yellow pine (SYP) DCBs were made from machined wood lamina and two separate adhesives: a thin film epoxy NB101 U 0.060 from Newport Adhesive and Composites, Inc. and a phenol formaldehyde (PF) impregnated paper 42209/PGF from Dynea Overlays, Inc., both approximately 250 μm in thickness. The exact chemical make up of both adhesives is unknown. The epoxy bonded specimens were formed with a two stage curing process: 20 hours at 55^{o}C followed by 3 hours at 100 ^{o}C. The PF-SYP bonds were formed by hot pressing under 245 kPa at 150^{o}C for 20 min. Three different dyes were available for staining: Safranin-O (0.5% in H_20), Toluidine Blue O (0.5% in H_20), Fast Green FCF (0.05% in H_20).

3.2.2 Sample preparation

A bandsaw was used to cut cross-sections from bonded SYP-DCB's, ranging in width from 10 mm to 20 mm. All laminations were prepared in the manner described in Chapter 2. For the epoxy system, four separate specimens were used from three laminations, with two to six cross-sections used from each specimen. The resulting sections were immersed in water until saturated. This enabled a finer cut and minimized microtome blade dulling. The epoxy bonds failed during water saturation, with the epoxy layer often detaching completely from both adherends. However, the penetrated epoxy remained attached within the wood cells. After microtoming, the epoxy –SYP samples were stained with Safranin-O (0.5% in H_20), while the PF-SYP samples were exposed to various dyes as mentioned below. The surfaces were coated with dye multiple times until

dye absorption appeared to be maximized. The dye was allowed to dry before the specimen was viewed under the microscope.

3.2.3 PF-SYP dye and fluorescent lighting combinations

The dyed surfaces were examined using a Zeiss Axioskop under a 100X magnification. Three different fluorescent light options were available: Triple Dichroic, Ultraviolet (UV), and Rhodamine Texas red. Separate PF-SYP samples were stained with Safranin-O (0.5% in H_20), Toluidine Blue O (0.5% in H_20), Fast Green FCF (0.05% in H_20) in or left unstained, and examined under the three different light options, creating nine different combinations.

3.2.4 Penetration measurements

Effective penetration is defined as the total area of adhesive divided by the bond width, which is equal to the microscopic field of view (Sernek et al. 1999). Image analysis software is used to contrast the adhesive from the wood. The software is calibrated from a reference image to determine the actual area covered by each pixel. The pixels are grouped together based on relative proximity, such as the adhesive shown within an individual cell, and the area of each group is calculated. Tolerances are set so that groupings having too small of an area are discarded as noise.

Another penetration measurement technique is to take maximum penetration depth measurements from the bondline interface at equally spaced distances (approximately 195 μm). Individual lines were drawn from the adhesive-adherend interface to the edge of the penetration depth into the substrate. Both measurement methods were developed by Sernek et al. (1999).

3.2.5 Epoxy penetration

For the epoxy-SYP bonds, photomicrographs were taken of earlywood and latewood regions separately, with 11 to 18 photomicrographs from three beams and two from a fourth. The best images were acquired using Safranin-O dye and UV fluorescent lighting. The choice was based on clarity and epoxy/wood color contrast. The clarity and contrast varied for many possible reasons, including but not limited to: variations in dye absorption into wood, presence of oils released from the wood, and blade sharpness. The epoxy's penetration into the wood adherend was measured using the effective penetration method and maximum penetration measurements.

3.3 Results and discussion

3.3.1 PF-SYP light and stain combinations

Figures 3.1 through 3.4 show examples of various light and stain color combinations from PF-SYP bonds. Some stain and filter combinations showed no contrast, such as Safranin-O under Rhodamine Texas red filtered light which showed everything as red. Others showed differentiation between the adhesive impregnated paper substrate in the bondline and the wood adherend, but failed to highlight the phenolic resin in both the paper substrate and wood adherend. In all cases the phenol formaldehyde penetration was minimal; penetration that occurred was considered too shallow and variable to warrant a penetration analysis.

Typically deeper penetration is considered necessary to ensure mechanical interlocking, an important adhesion mechanism in wood-adhesive bonds. However, as discussed in Chapter 2, the PF-SYP bonds had moderately high fracture energy values, with an average G_{Ic} of 272 J/m^2. This proves that deeper penetration is not necessary for adequate Mode I fracture energy values.

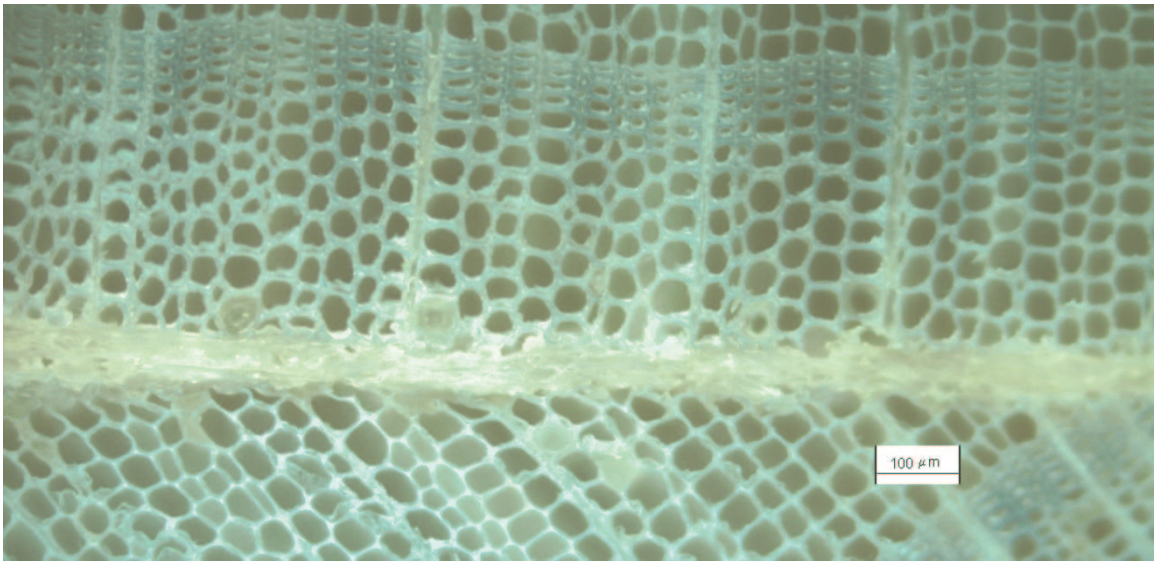

Figure 3.1: Photomicrograph of a microtomed PF-SYP bond under UV light with no stain.

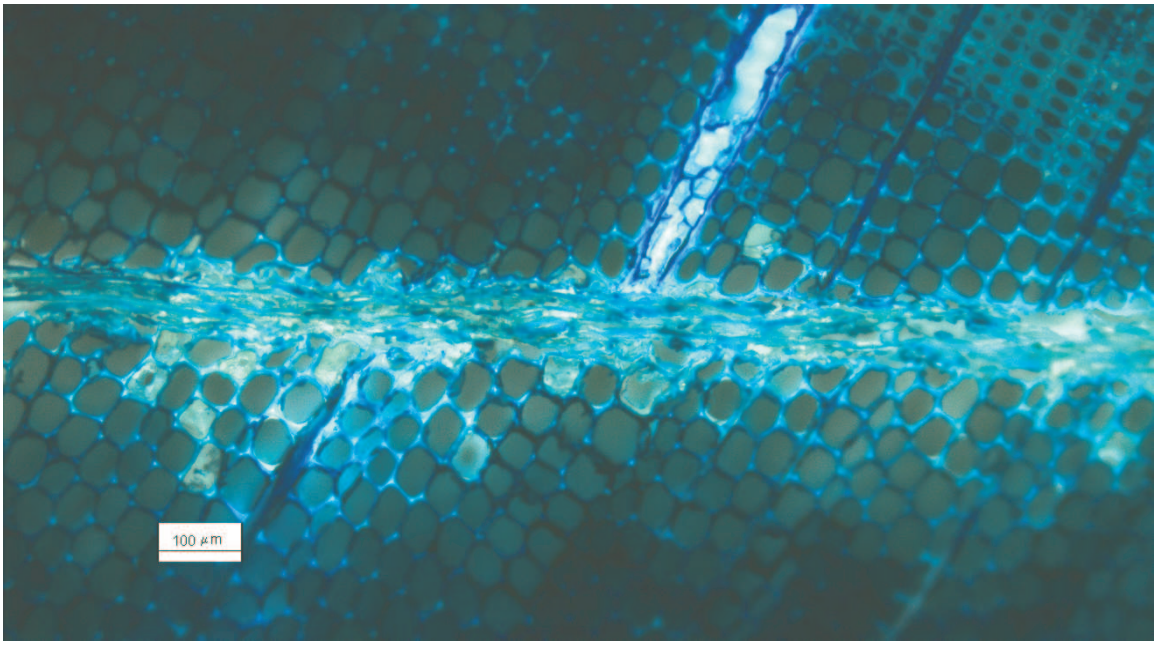

Figure 3.2: A microtomed PF-SYP bond stained with Toluidine Blue O under UV light.

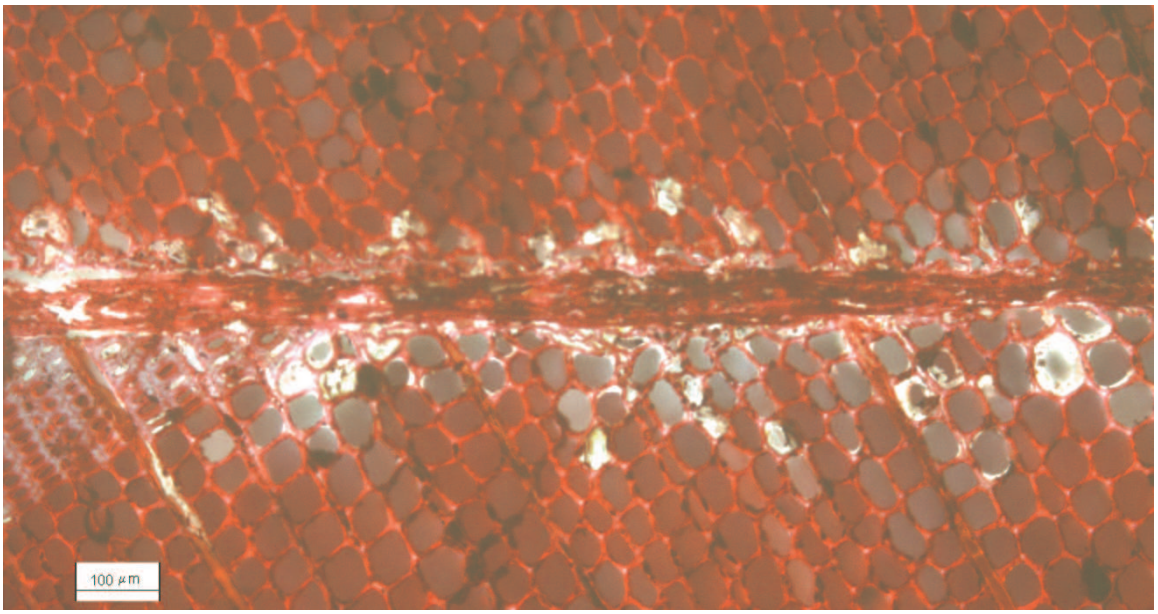

Figure 3.3: A microtomed PF-SYP bond stained with Safranin-O under UV light.

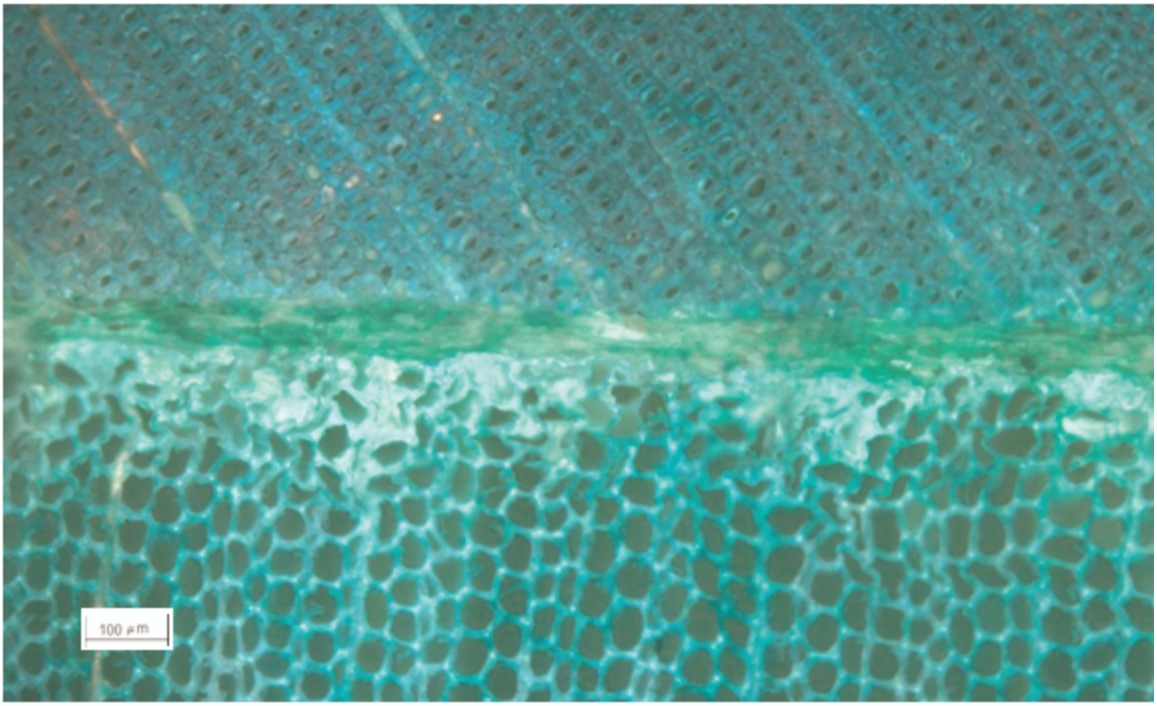

Figure 3.4: A microtomed PF-SYP bond stained with Fast Green FCF under UV light.

3.3.2 Epoxy penetration analysis

Table 3.1 shows the calculated effective penetration, photomicrograph image width, grouping area standard deviation, total area of all groups, and number of groups from 19 sample photomicrograph images taken of earlywood regions. For example,

image 15:2a5A showed 163 similar color groupings, for a total of 2.9E+04 μm^2, with a group area standard deviation of 642 μm^2 from the average; while the entire image width was 1039 μm, yielding an effective penetration of 28 μm. The images are labeled in the order of lamination lay-up, DCB number, cross-section letter, image number, and beam letter (A or *B*). In the case of 15:2b2B shown in Figure 3.5, the image is of beam *B*, the 2nd image from cross-section '*b*' from the 2nd DCB specimen from the 15th epoxy lamination.

Table 3.1: The effective penetration measurements of epoxy into earlywood growth regions.

Sample Image	Groups	Total Area	Group Area Std.Dev	Image Width	Effective Depth
	#	μm^2	μm^2	μm	μm
15:2a3A	72	37298	697	897	42
15:2a5A	163	28959	642	1039	28
15:2a6A	88	38976	1094	1157	34
15:2b2B	141	65996	1233	1362	48
15:2b4A	136	23803	229	1360	17
15:2b6A	101	36849	765	953	39
16:5a3A	93	53302	1497	1209	44
16:5a6A	132	32975	365	1356	24
16:5b2A	144	50792	657	1360	37
16:5b4B	146	37805	489	1360	28
16:5b5B	162	84161	1488	1358	62
18:0a2B	21	123455	19110	1361	91
18:0a3A	31	13793	492	595	23
18:0a5B	52	46320	1564	1360	34
18:0d3B	8	99261	32659	1362	73
18:0f2B	89	102109	1924	1360	75
18:1a1A	77	94024	2752	1360	69
18:1a2B	42	14115	589	1362	10
18:0a4A	76	79603	5715	1358	59
				Average	44.1
				COV %	49.7

The average effective penetration from all 19 earlywood sample images is 44 μm, with a coefficient of variation (COV) of 50%. This depth is more than four times the effective penetration of 10.2 μm into latewood regions, with a COV of 76%, as shown in Table 3.2.

Table 3.2: The effective penetration measurements of epoxy into latewood growth regions.

Sample Image	Groups	Total Area	Group Area Std.Dev	Image Width	Effective Depth
	#	μm^2	μm^2	μm	μm
15:2a2B	76	7549	129	1234	6
15:2a4A	96	12441	142	1360	9
15:2a5A	75	10747	384	505	21
15:2b1B	37	3716	87	1360	3
15:2b3B	52	5355	79	1358	4
15:2b5A	89	7106	80	1358	5
16:5a4A	107	12023	340	1358	9
16:5a5A	69	10689	182	1360	8
16:5b1A	125	20861	483	1360	15
16:5b3A	187	20076	182	1362	15
16:5b6B	134	18322	161	1362	13
16:5b7B	214	31635	217	1362	23
18:0a1A	132	13490	129	1358	10
18:0a3A	41	6992	247	781	9
18:0d2A	144	10064	179	1362	7
18:0e2B	58	42034	1334	1358	31
18:0g1B	74	2886	39	1362	2
18:0g2B	26	1076	40	1360	1
18:0h1A	86	5165	68	1244	4
18:0h2B	217	9978	52	1360	7
				Average	10.2
				COV %	75.9

The penetration depth was also determined using maximum penetration depth measurements. From all images, the penetrated earlywood regions showed an average maximum penetration depth of 111.9 μm with a COV of 35.7%. The penetrated latewood regions showed an average maximum penetration depth of 76.5 μm with a COV of 59.3%. The earlywood depth measurement is less than 1.5 times the latewood depth, though the latewood's greater variation is consistent with the effective penetration measurement. The effective penetration measurement technique does not include the cell walls in its calculation of the total area, though the cell walls are included in the total image width measurement. Therefore the results from the maximum penetration depth measurement technique are greater.

The effective penetration measurement technique indicated greater penetration

into earlywood regions partly because the empty cell's internal diameter is much greater, allowing for a greater amount of epoxy to fill its void. The larger capillaries also offer less restriction to a viscous liquid. The maximum penetration measurement shows the epoxy does penetrate farther into the latewood regions than the effective penetration measurement technique indicates. However, the actual volume penetrated into the denser latewood regions is much lower compared to the volume penetrated into earlywood, which the maximum penetration depth measurement technique does not indicate. Figures 3.5 and 3.6 show samples 15:2b2B and 16:5b5B, typical images of epoxy adsorbed into earlywood, with Tables 2.3 and 2.4 showing the maximum penetration measurement data for that photomicrograph.

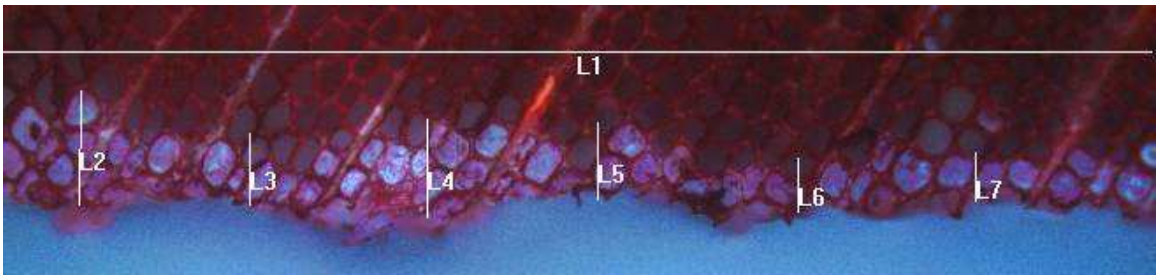

Figure 3.5: **Photomicrograph of sample 15:2b2B stained with Safranin-O under UV light with maximum penetration and image width measurements.**

Table 3.3: **Length measurements for maximum penetration and image width for sample 15:2b2B**

Measurement	15:2b2B Length, ◊m
L1	1360.3
L2	135.0
L3	85.2
L4	116.3
L5	91.4
L6	64.4
L7	58.2

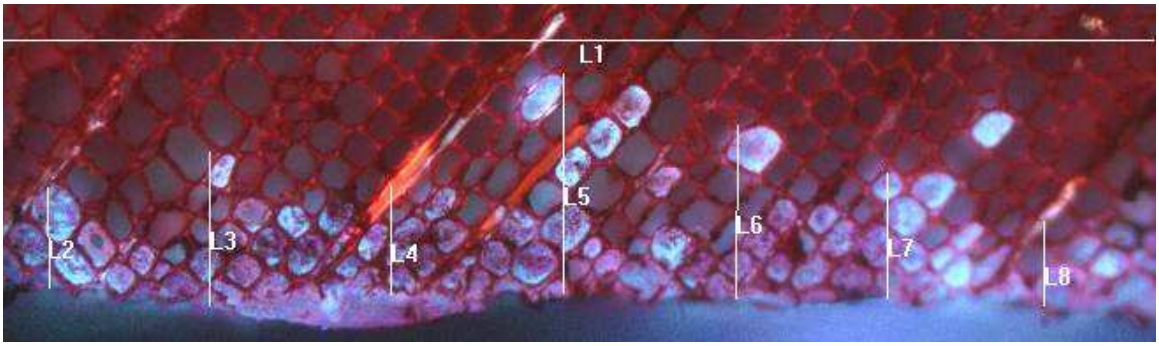

Figure 3.6: **Photomicrograph of sample 16:5b5B stained with Safranin-O under UV light with maximum penetration and image width measurements.**

Table 3.4: **Length measurements for maximum penetration and image width for sample 16:5b5B**

Measurement	16:5b5B Length, μm
L1	1358.3
L2	118.4
L3	180.7
L4	128.8
L5	257.5
L6	203.5
L7	147.5
L8	99.7

3.3.3 Epoxy's preferential adhesion to earlywood plausible influence on fracture

The epoxy-SYP DCB's of 10 mm, 15 mm, and 20 mm widths were tested under quasi-static monotonic loading to investigate width dependence of the critical and arrest strain energy release rate, G_{Ic} and G_{Ia} respectively. The only significant dependence was apparent in the statistical scatter of G_{Ic} and G_{Ia}, though the average values were approximately the same and much lower than expected. The scatter was found to decrease as specimen width increased, reaching a minimum at 20 mm, which is apparent in Figure 3.7, showing G_{Ic} results from individual specimens plotted against their widths.

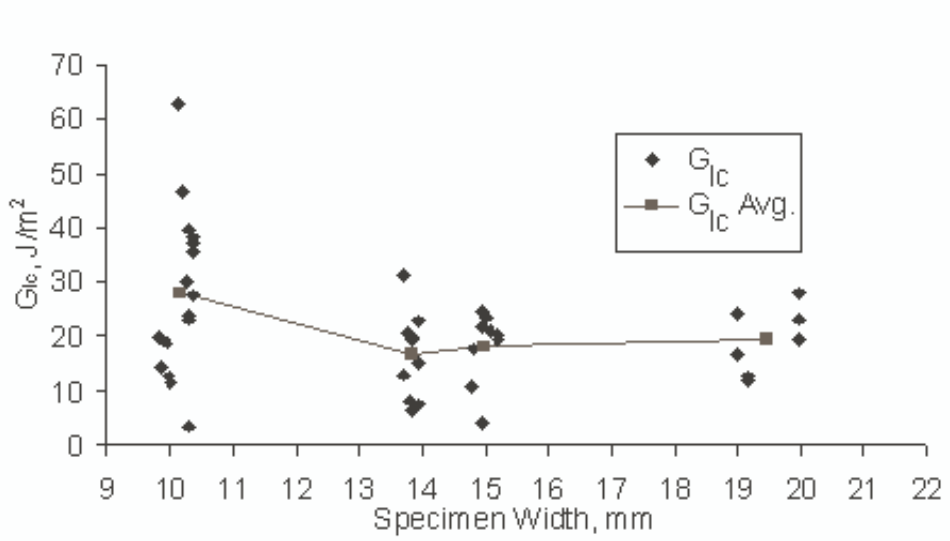

Figure 3.7: Critical strain energy release rate, G_{Ic}, plotted as a function of width.

A plausible reason for the decreased scatter in fracture energy with increased with is the fact that wider specimens have a greater variety of wood growth types exposed on the substrate surface at each crack length. Visual inspection of the fractured surfaces showed more epoxy remaining adhered to earlywood regions than latewood. This indicated the epoxy system preferentially bonded to earlywood. Plausibly the bond fracture energy depends on the growth type to which the adhesive is bonded. As described above, the epoxy penetrated farther into earlywood regions than latewood regions. At some crack lengths a narrow specimen may have a greater proportion of earlywood near the crack tip, while at other lengths there is an abundance of latewood. Some fracture specimens showed growth rings spanning the cross-sections parallel to the bondline, while other specimens showed growth rings intersecting the bondline at an angle. In the latter cases, a wider specimen will have a more consistent proportion of latewood to earlywood exposed on the substrate surface. Greater consistency in growth type proportions at wider widths could cause less scatter in the critical and arrest fracture energies.

3.3.4 PF-SYP and epoxy-SYP fracture energy difference

The critical and arrest fracture energies from PF-SYP DCBs were approximately 272 J/m^2 and 200 J/m^2 respectively. However the epoxy-SYP DCBs had much lower critical and arrest fracture energies, approximately 20 J/m^2 and 14 J/m^2 respectively. This is very interesting considering the fact that the epoxy bond system had good penetration into the adherend while the PF bond system had very shallow penetration. Adequate penetration is considered necessary to ensure mechanical interlocking, an important adhesion mechanism in wood-adhesive bonds. Plausible reasons for the epoxy systems low fracture energy values were discussed in Chapter 2, though no conclusions were made.

Another interesting fact to consider is that the neat epoxy resin has a critical fracture energy of approximately 493 J/m^2. Even if the wood was only flowing into the wood cells but poorly adhering to the cell walls, the good penetration and mechanical interlocking would indicate the epoxy DCBs should still have high fracture energy values. This indicates the possibility that something is influencing the epoxy stoichiometry so that the resin at the bondline interface is mechanically different than the neat epoxy resins tested in bulk form in Chapter 2. The only apparent difference between bulk fracture tests and the epoxy DCB fracture tests is the presence of wood during the specimen preparation. Plausibly it is the wood which influenced the epoxy stoichiometry at the bondline interface, which in turn led to low fracture energy values in the epoxy-SYP DCBs.

3.3.5 Aluminum paint penetration

The PF-SYP DCB specimens were coated with an oil-based aluminum, as described in section 2.2.3. Photomicrographs were taken of microtomed surfaces under

UV light to evaluate the penetration, as shown in Figure 3.8. The paint's penetration was considered to be too shallow to influence the specimen's stiffness or adhesive strength.

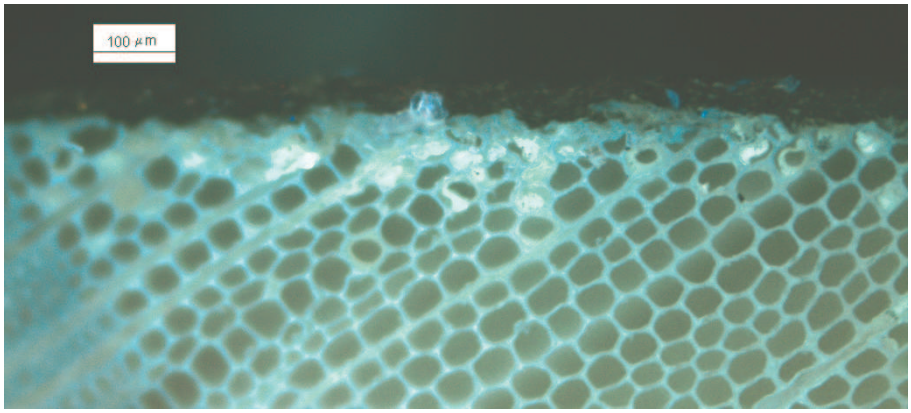

Figure 3.8: Photomicrograph of a microtomed section from a PF-SYP DCB specimen coated with an oil-based aluminum paint, with nominal paint penetration from the side.

3.4 Summary

Cross-sections from epoxy and PF SYP DCB's bond's were microtomed and examined under fluorescent light with a microscope. The epoxy system's latewood regions were found to have an effective penetration of 10.2 µm and a maximum penetration depth of 76.5 µm. The epoxy system's earlywood regions were found to have an effective penetration of 44 µm and a maximum penetration depth of 111.9 µm. This difference in penetration depths could explain the preferred adhesion to earlywood in fractured epoxy bonds, as discussed in Chapter 2. Though the PF-SYP bonds were found to have shallow penetration compared to the epoxy-SYP bonds, the PF-SYP bonds had much higher fracture energy values, as shown in Chapter 2. Dye and light combination choices were explored for PF-SYP bonds, with the phenolic resin being more apparent in both the wood adherend and impregnated paper substrate for some combinations and less for others. The aluminum paint used to cover the PF-SYP DCBs was shown to have nominal penetration depth, be too shallow to influence the specimen's stiffness or adhesive strength.

Chapter 4: Angled latewood/earlywood influences on a specimen

4.1 Introduction

In Chapter 2 southern yellow pine (SYP) double cantilever beam (DCB) specimens were prepared so as to ensure the longitudinal grain converged with the bond line at an approximately 3^o angle, as shown in Figure 4.1 below. Due to wood's natural variability, the grain angle may have varied among and within specimens, but generally remained greater than 0^o and less than 10^o. Also, in many specimens the longitudinal grain converged against the beam side. This chapter focuses on the effects caused by the differences in longitudinal elastic moduli between the latewood and earlywood growth types, and grain angles along the length causing change in growth type proportions within the cross-sections. An appropriate specimen width will be suggested based on effective stiffness changes along the length for specimens with an angled longitudinal grain converging against the specimens sides. The influences on the elastic strain energy stored in an individual beam will be described for different grain orientations. The grain angle dependence of the macroscopic elastic modulus along the beam length will be investigated and compared to the macroscopic longitudinal elastic modulus for SYP. Also investigated will be the grain angle influence on the depth of adhesive penetration into the wood substrate.

As discussed in Chapter 1, for SYP the darker latewood density and stiffness is approximately three times that of the lighter earlywood. Considering that the grain angle against the bondline changes the latewood and earlywood growth ring distance from the neutral axis, the growth type stiffness difference will cause the beam's effective stiffness to vary along its length. If growth ring sizes and distributions remain constant, the

stiffness variations will be periodic, with the period depending on grain angle. Changes in the growth type distribution within the cross-section influences many factors, including local receptibility to strain energy, beam asymmetry, and expected statistical scatter of the specimen's effective stiffness as a function of adherend width. The influences on strain energy and beam asymmetry will influence the critical load and the change in crack length with fracture. Shown below in Figure 4.2 are cross-sections from individual beams at different points along the length. Many growth rings are clearly more horizontal in orientation across the cross-section (such as beams B, C, and D in Figure 4.2); this grain orientation is commonly referred to as being flatsawn.

Figure 4.1: Image of a specimen's side showing the grain angle convergence with the bond line at an approximate 3^{o} angle, with initial crack starting at the end with the drilled holes.

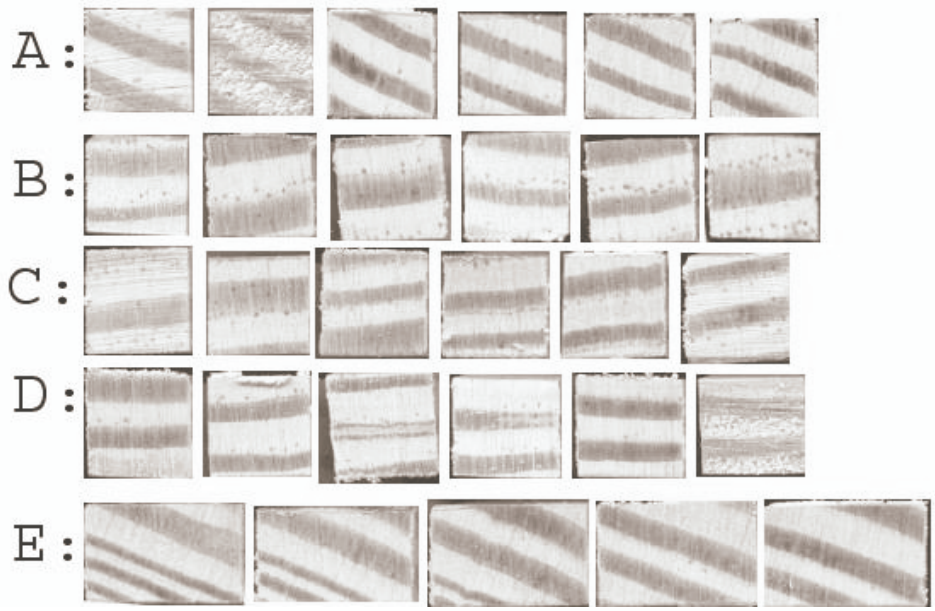

Figure 4.2: Cross-sections from typical adherends, where each row is from a different beam, showing the change in grain distribution along the beam length.

In some beams, the growth rings may not be oriented horizontally across the cross-section; this is commonly referred to as quartersawn, as shown in Figure 4.3. For a more vertically oriented grain, a grain angle against the beam side, as shown in Figure

4.4, will cause latewood or earlywood sections to leave the cross-section. This results in a change in the proportion of latewood to earlywood, thereby changing the beam's stiffness. The proportion of earlywood to latewood is more constant for wider beams with this type of grain orientation.

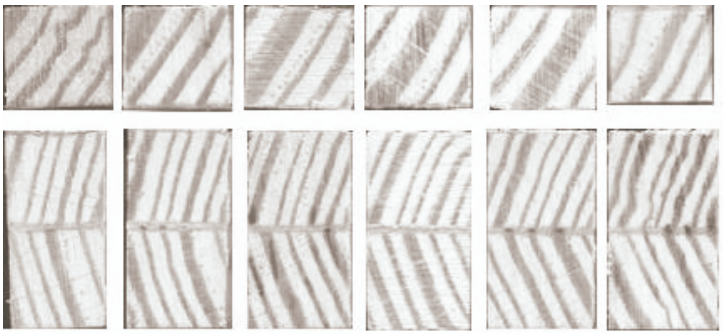

Figure 4.3: Cross-sections from typical adherends with vertically oriented growth rings, where each row is from a different beam, showing the change in grain distribution along the beam length.

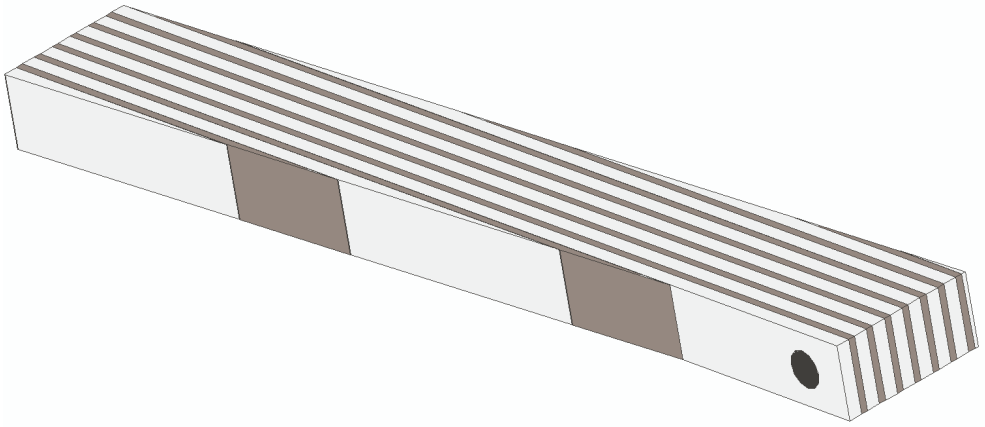

Figure 4.4: Simulated adherend with vertically oriented growth rings converging on the specimen side at a 3^{o} angle.

4.2 Methods

4.2.1 Calculating grain angle influence on E_{xx} and adhesive penetration depth

4.2.1.1 Calculating grain angle influence on E_{xx}

The influence the grain angle converging on the bondline, θ, has on the macroscopic elastic modulus along the beam length, E_{xx}, will be investigated using the modulus transformation equation (Equation 4.1) (Jones 1975). This is an alternative method to the Hankinson equation, a common method in wood mechanics for calculating

the change in modulus of elasticity with a change in grain angle. The longitudinal macroscopic elastic modulus, E_L, radial modulus, E_R, radial-longitudinal plane shear modulus, G_{LR}, and Poisson's ratio, ν_{LR}, will be based on loblolly pine, as given in Table 4.1. The radial-tangential plane elastic moduli and Poisson ratios listed in Table 4.1 do not satisfy the reciprocity relation of Equation 4.1. Instead of being equal to 1, the right hand side becomes 0.728 for the listed values. This means the values from Table 4.1 must be used with the understanding that they may be incorrect.

$$\frac{E_T}{E_R}\frac{\nu_{RT}}{\nu_{TR}} = 1 \qquad \textbf{4.1}$$

Table 4.1: Modulus and Poisson's ratios for different the orthotropic directions and planes (Green et. al, 1999).

Species	E_T/E_L	E_R/E_L	G_{LR}/E_L	G_{LT}/E_L	G_{RT}/E_L	ν_{LR}	ν_{LT}	ν_{RT}	ν_{TR}
Loblolly	0.078	0.113	0.082	0.081	0.013	0.328	0.292	0.382	0.362
Longleaf	0.055	0.102	0.071	0.06	0.012	0.332	0.365	0.384	0.342
Slash	0.045	0.074	0.055	0.053	0.01	0.392	0.444	0.447	0.387

.

$$\frac{1}{E_{xx}} = \frac{1}{E_L}\cos^4(\theta) + \left(\frac{1}{G_{LR}} - \frac{2\nu_{LR}}{E_L}\right)\sin^2(\theta)\cos^2(\theta) + \frac{1}{E_R}\sin^4(\theta) \qquad \textbf{4.2}$$

4.2.1.2 Calculating grain angle influence on adhesive penetration depth

Frequently adhesives penetrate into the wood adherends through the empty cell lumens, not by diffusion through the cell walls. For this reason the angle at which the grain converges on the bondline will greatly influence the penetration depth measurements used in Chapter 3. The adhesive maximum penetration depth measurement determined the depth the adhesive penetrated into the adherend by measuring a distance perpendicular to the bondline as viewed from a specimen cross-section. Presuming that the adsorption into the cell lumens is controlled by pressure and adhesive viscosity, the distance penetrated along the cell length, L, will be independent of grain angle. For this reason L can be regarded as the hypotenuse of a right triangle, as

depicted in Figure 4.5 and the maximum penetration depth, d_p, can be estimated with Equation 4.3.

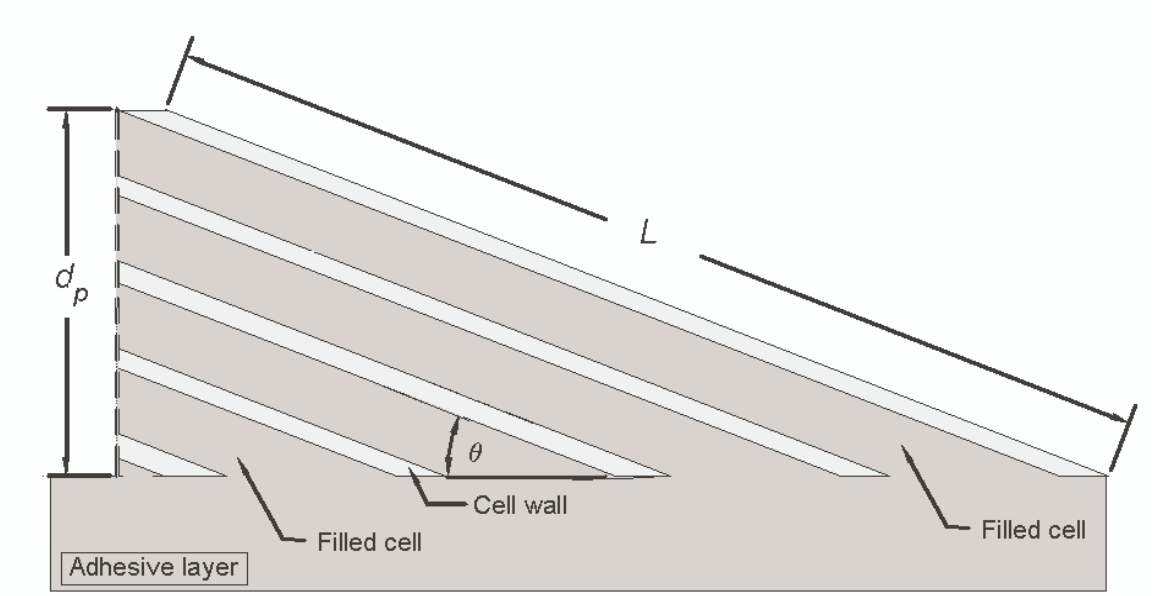

Figure 4.5: Represenatation of adhesive penetration into cell lumens along the cell for a length, *L*, with the maximum penetration measurement, d_p, as determined in Chapter 3, and the grain angle *θ*.

$$d_p = L\sin(\theta) \qquad \textbf{4.3}$$

4.2.2 Calculating the second moment of area (SMA)

When calculating the cross-section second moment of area (SMA) and centroid height, the stiffness difference between the latewood and earlywood must be taken into account. This is done by multiplying the latewood section width by the ratio of latewood longitudinal modulus to earlywood longitudinal modulus, and then assuming the modulus for the entire cross-section is uniformly equal to a reference modulus, which arguably is an erroneous assumption. For the work done in this project, the modulus ratio was taken to be 3, with an earlywood stiffness of 6.24 GPa serving as the reference modulus.

The SMA will be calculated for the cross-section at discrete increments along the beam length, as in the following example. Figure 4.6 provides an illustration of the relative weighting for each growth ring and the resulting SMA for the different cross-

sections along the length of a 20 mm beam with a 3° grain angle. In the right hand column, the latewood sections (dark) are three times wider than the earlywood sections. At a beam length of 115 mm the outer edges are earlywood, leaving in the center three 1 mm thick latewood growth rings and two 2 mm thick earlywood growth rings. The resulting SMA is 2397 mm^4. Farther down the beam at 130 mm, a new latewood growth ring has begun to enter the cross-section at the top while all growth rings have moved down, partly removing a softer earlywood ring and positioning a stiff latewood ring further from the neutral axis. This results in a greater SMA of 2765 mm^4. And at a length of 150 mm, four nearly full latewood growth rings are present, with two far from the neutral axis, effecting a SMA of 3113 mm^4. Because the relative position of each grain type changed with each change in length, a new calculation was required for each point along the beam's length.

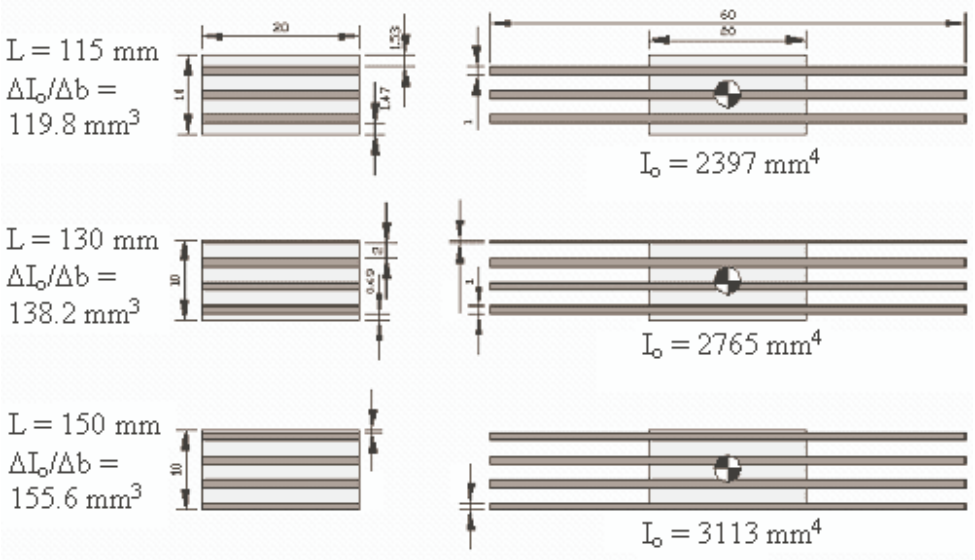

Figure 4.6: Stiffness determination for composite beam showing relative proportions of regions having different stiffness values

4.2.3 Calculating the stored elastic strain energy

Assuming uni-axial loading with negligible shear stresses, the strain energy stored in a beam under load, P, can be represented by Equation 4.4, where x is measured along

the beam length, y in the height direction, and z measured across the constant beam width, *b*.

$$U = \frac{1}{2}\int_0^L \int_{-h/2}^{h/2} \frac{(Pxy)^2}{I^2 E_x} b dy dx = \frac{P^2 b}{2}\int_0^L \left(\frac{x}{I(x)}\right)^2 \int_{-h/2}^{h/2} \frac{y^2}{E(x,y)} dy dx \qquad \textbf{4.4}$$

Because I varies only along the x direction, and the reference modulus, E_o, is constant, Equation 4.4 can be reduced to:

$$U = \frac{P^2}{2}\int_0^L \left(\frac{x^2}{E_o I(x)}\right) dx \qquad \textbf{4.5}$$

Using the Matlab scripts given in Appendix A1 and A2, for flatsawn and quartersawn beams respectively, Equation 4.5 was numerically integrated at each point along the beam's length to calculate the strain energy stored in the beam.

4.3 Results and Discussion

4.3.1 Grain angle influence on E_{xx} and adhesive penetration

4.3.1.1 Grain angle influence on E_{xx}

Using the average longitudinal and radial grain macroscopic material properties for loblolly pine, the influence grain angle has on the macroscopic elastic modulus along the beam length, E_{xx}, was investigated using the modulus transformation equation (Equation 4.2). The ratio of the calculated E_{xx} to E_L is plotted against grain angle, as shown in Figure 4.7. A 3^o grain angle leads to approximately a 3% difference between E_{xx} and E_L. This small variation is well within reason considering the longitudinal elastic modulus has a coefficient of variation in the range of 22%. For comparison, a 10^o grain angle leads to approximately a 22% difference between E_{xx} and E_L.

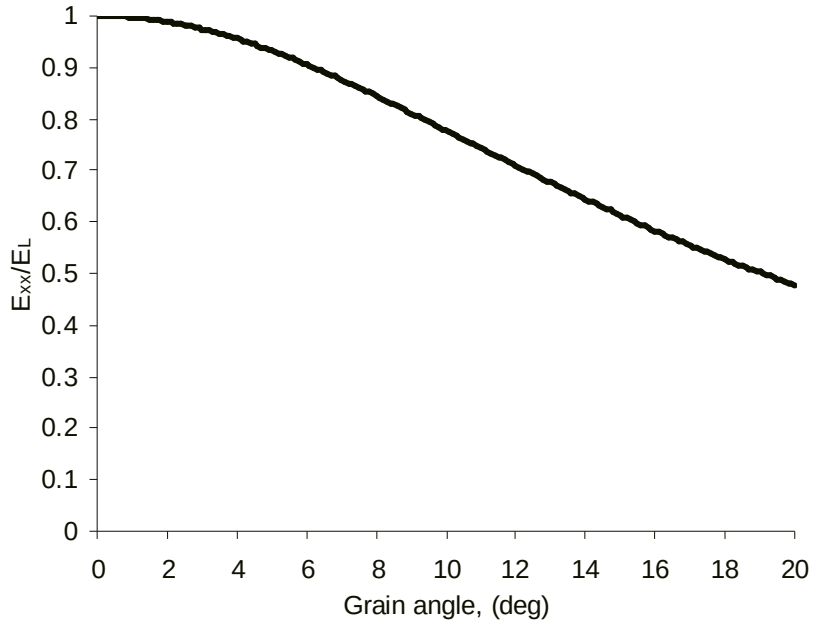

Figure 4.7: **The plot of the beam longitudinal stiffness, E_{xx}, to loblolly pine longitudinal elastic modulus, E_L, based on the modulus transformation equation (Equation 4.2) and the loblolly pine material constants given in Table 4.1.**

4.3.1.2 Grain angle influence on adhesive penetration depth

For the epoxy-SYP bond system analyzed in Chapter 3, the average maximum penetration depth of the epoxy into the earlywood regions was 111.9 μm. Using Equation 4.3, with d_p = 111.9 μm and presuming the grain angle, θ, was, 3°, the distance penetrated along the cell length, L, was 2138 μm. Presuming L to be constant for all grain angles when adhesive penetration is controlled by viscosity and bondline pressure, Equation 4.3 was used to calculate the maximum penetration, d_p, for a range of angles, θ, shown in Figure 4.8. Clearly the grain angle influences the adhesive penetration depth.

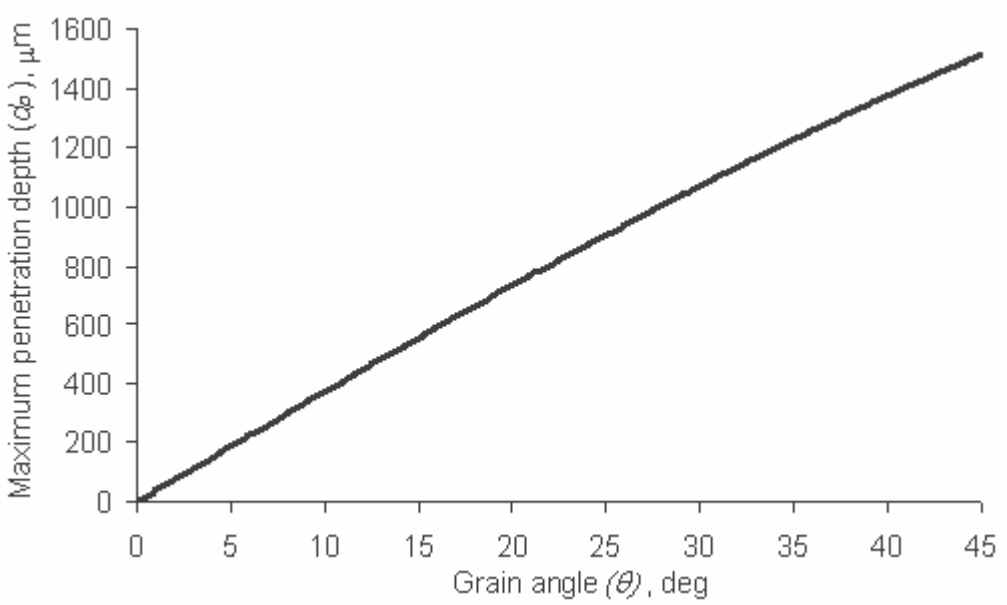

Figure 4.8: Maximum penetration, d_p, as a function of the grain angle converging on the bondline, θ, using Equation 4.3.

Chapter 3 shows that when comparing bonds with two different adhesives, the adhesive penetration depth is not an indicator as to which bond system will show higher critical strain energy release rates (G_{Ic}). For instance, SYP bonded with phenol-formaldehyde (PF) showed much deeper penetration depths compared to the epoxy-SYP bonds. However, the PF bonds had G_{Ic} values over 13 times greater than the epoxy-SYP bond system. But for comparing different adhesive penetration depths for the same bond system, the penetration depth could still influence the fracture behavior in various ways. For instance, the penetrated region will form a composite layer with mechanical properties different from both the empty wood and bulk adhesive. How this composite layer influences fracture behavior is dependent on the thickness of the layer. The thickness of the composite layer is dependent on how far the adhesive penetrates into the wood substrate. Clearly the grain angle influence on the adhesive penetration depth is an important issue to consider.

4.3.2 Appropriate width determination through SMA analysis

An analysis of second moment of area's (SMA) dependence on grain angle, orientation, and relative position will prove useful for multiple reasons. As discussed in Chapter 2, the DCB fracture tests produced strain energy release rate (G_{Ic}) values that were deemed too small to sufficiently comment on the appropriate beam width. Though each fracture test was considered valid, the concern is caused by the average G_{Ic} value being about a fifth to a twentieth of other wood adhesion fracture tests. The plastic zones created by the comparatively smaller critical loads may have been too small to play a significant role in fracture behavior. So the influence of plane stress from edge effects, as investigated in a width variation experiment, was not determined.

An appropriate specimen width can still be suggested based on two criteria. The first criterion, the importance of which is evident in Figure 4.9, is the increase in statistical scatter with a decrease in width. As discussed in Chapters 2 and 3, the scatter may be due to bond strength being dependent on the growth type to which the adhesive is bonding. Wider specimens will have better consistency in the proportion of growth types exposed across the width of the adherend's surfaces, meaning there will be greater consistency in bond strength and fracture energy. The second criterion is based on a beam stiffness analysis considering the stiffness changes along the beam.

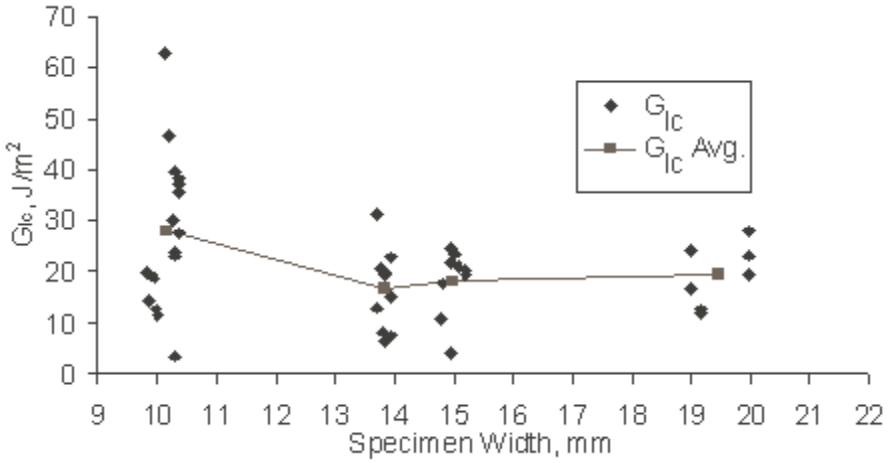

Figure 4.9: **G_{Ic} as a function of specimen width for epoxy and SYP DCB. Each data point represents the average G_{Ic} value from one specimen.**

The 10 mm wide fracture specimens produced a coefficient of variation of 54.4% between 3.48 J/m^2 and 62.6 J/m^2, minimum and maximums, respectively. The variation decreased as width increased, showing 42.0% and 31.6% for 15 mm and 20 mm widths respectively, with range decreasing as well. As expected for horizontally oriented (flatsawn) grain, the second moment of area's value will increase linearly with changes in width, assuming the position and thickness of each latewood section remains the same. For an isotropic material the rate of increase would be $h^3/12$, since for a rectangular cross-section:

$$I = \frac{bh^3}{12}$$

But because a composite beam calculation for the second moment of area has a dependence on the relative positioning and thickness of each growth ring, the rate of increase in I for a change in width will depend on these values. Since these values can vary greatly among beams, the rate of increase may be significantly different for any two beams.

Also of importance is a stiffness variation within an individual beam. Figure 4.10

shows the variation in the second moment of area along the length of a 20 mm wide beam with a vertically oriented end grain. The longitudinal grain angle against the beam side, of the kind shown in Figures 4.3 and 4.4, is set to 3^{o}. The growth ring thicknesses and distributions are assumed to be constant, with latewood and earlywood growth rings of 1 mm and 2 mm thickness, respectively. In all cases the earlywood is chosen as the reference material when using the composite beam method to calculate the SMA.

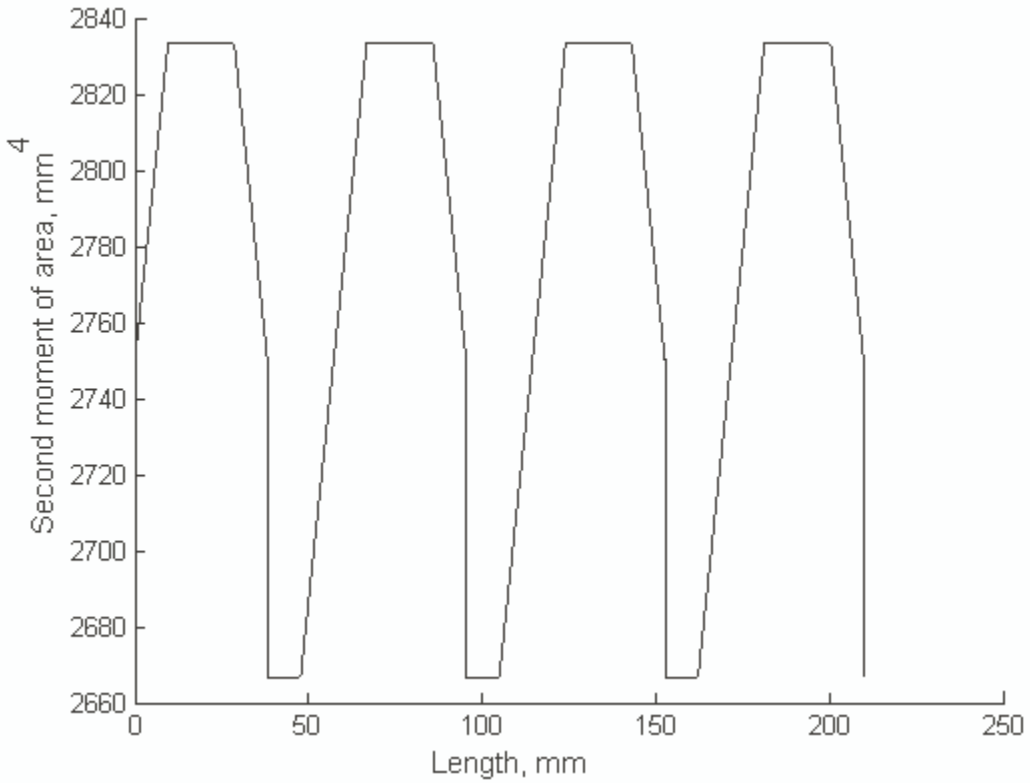

Figure 4.10: **A plot of a 20 mm wide beam's second moment of area along its length, assuming a vertically oriented grain, with a grain angle against the beam side as measured from the top.**

A periodic nature is apparent, and logically there would be a greater frequency if the grain angle was greater. The amplitude is dependent on the proportion and spacing of latewood to earlywood, with the amplitude decreasing towards zero as the beam becomes more isotropic. For the case displayed in Figure 4.10, there is a 5.9% drop from the maximum value of approximately 3415 mm^4.

The appropriate specimen width may be suggested by looking at the extreme situation of completely vertically oriented growth rings, with latewood regions waxing and waning in and out of the cross-section due to a grain angle against the side measured from the top. Plotting $\Delta I = I_{max} - I_{min}$ vs. beam width results in inconsistent lines which never converge. This is due to the difference between the maximum and minimum stiffness values being at most one latewood growth rings contribution, regardless of beam width. But plotting I_{min} / I_{max} vs. beam width shows a convergence toward unity as width increases. For a specimen width of 20 mm the greatest percentage difference between I_{min} and I_{max} is approximately 7%. For a specimen width of 25 mm the greatest percentage difference is approximately 5%. The specimens modeled with the Matlab script in Appendix A2 represent extreme cases considering that compared to other species SYP shows a much greater latewood/earlywood difference and distribution, and that most grain orientations across a cross-section are between quartersawn and flatsawn. For this reason, a specimen width of 20 mm should be adequate. However multiple standards, including ASTM D3433-93, recommend a specimen width of 25 mm. The analsysis in this chapter did not prove specimens should be specimens should be narrower than conventional standards.

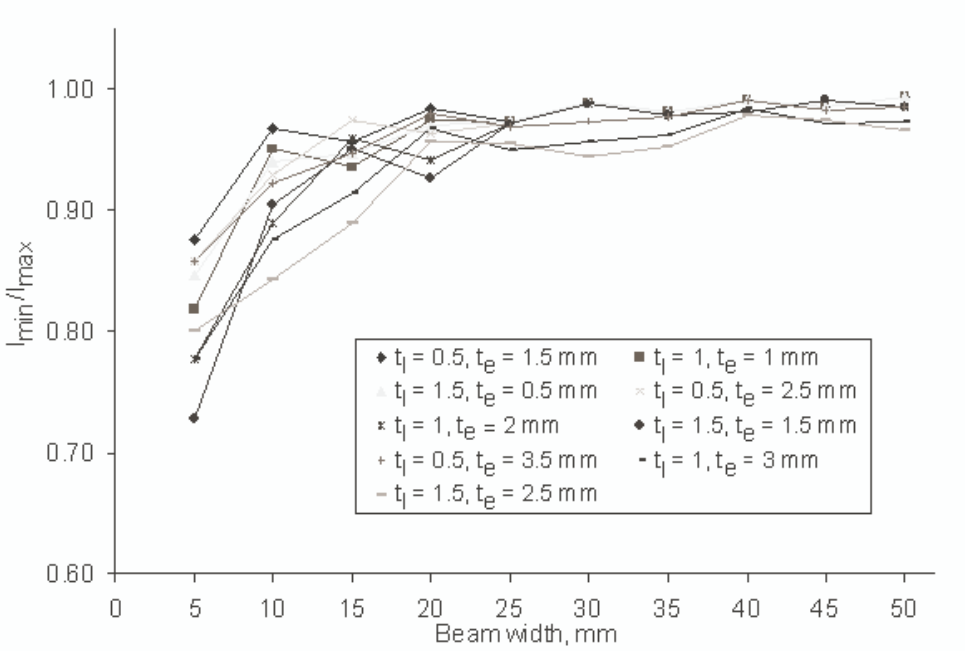

Figure 4.11: The minimum to maximum second moment of area ratios within individual beams at different widths for vertically oriented end grain with different latewood growth ring thicknesses, t_l, and earlywood growth ring thicknesses t_e.

4.3.3 Strain energy influences

4.3.3.1 Horizontally oriented grain

A Matlab script, given in Appendix A1, was used to explore the effects of grain angle and growth type distribution had on strain energy for beams with growth rings horizontally spanning the cross-sections (flatsawn). An effective means for demonstrating the influence grain angle will have on a composite beam is to plot strain energy as a function of length under a defined load. For an isotropic material, the log-log plot of the beam's stored strain energy versus length is a straight line, with a slope of three decades to one, as shown in Figure 4.12. This is because, for the case of an isotropic beam, Equation 4.5 reduces further to

$$U = \frac{P^2 L^3}{6EI} \qquad \textbf{4.6}$$

Equation 4.5 was numerically integrated at each point after calculating the new second moment of area, *I(x)*. The results show that generally, the slope is the same as the

isotropic case. However beyond 10 mm there are some regions where the slope was greater than 3 decades to 1, and others where the slope was less, as seen in the slightly varying line of Figure 4.12.

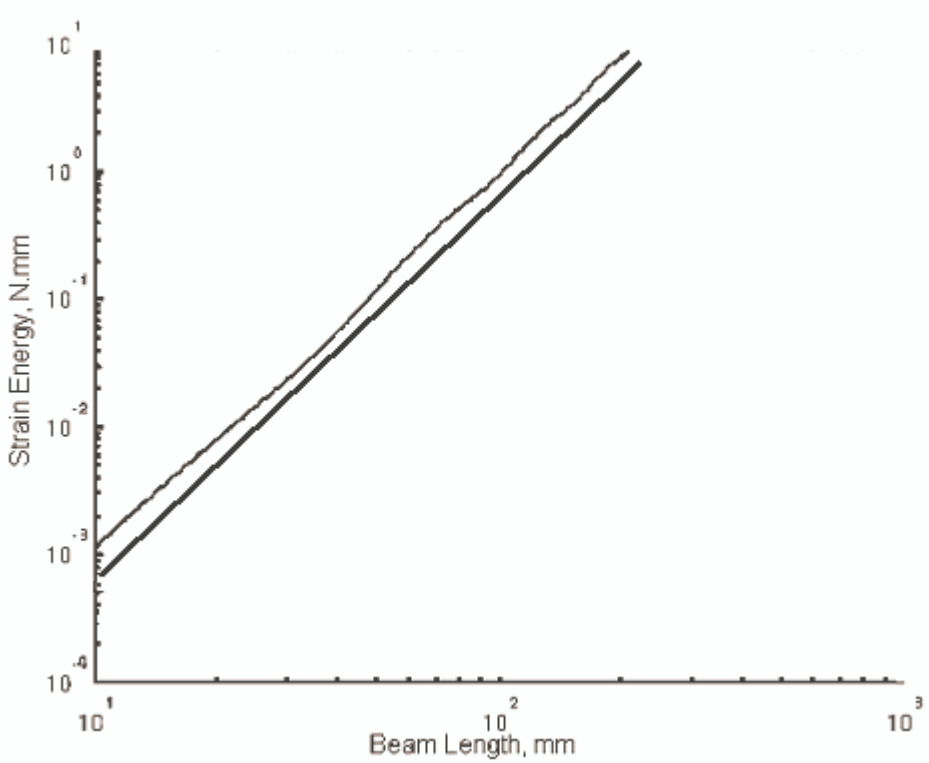

Figure 4.12: **The log-log plot of strain energy stored in the beam versus the beam or crack length. The bottom line is from a simulated beam made completely of earlywood, while the upper line is from a simulated beam with latewood ring thickness of 1 mm spaced 3 mm apart.**

From the apparent waviness, regions of lesser slope correlate to regions where the beam stiffness is greater. Likewise the greater slopes correlate to lesser beam stiffnesses. The greater stiffness region's jumps correspond to situations where latewood rings lose their prominence near the edges, either by approaching the beam's centroid, or waning past the edge. Figure 4.13 attempts to illustrate such an example by showing strain energy as a function of length, periodic stiffness values along the length, and the grain distributions for three cross-sections before, during and after significant slope changes in the strain energy and stiffness plots respectively. The second moment of area shows an

approximate increase of 42% measured from the minimum. The round bottom regions correspond to places where no latewood is waxing into or waning out of the cross-section but merely changing position.

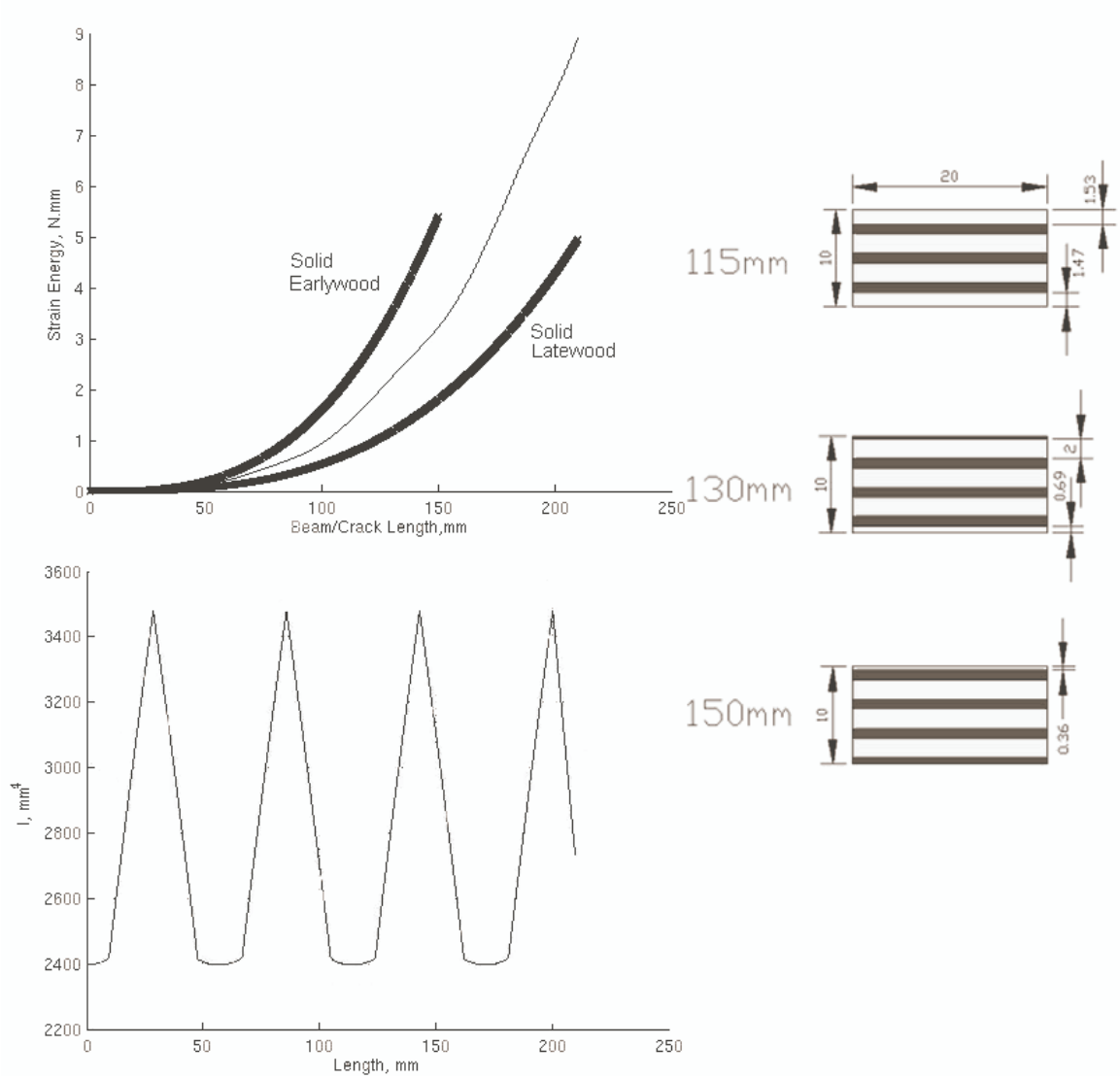

Figure 4.13: **The top graph shows the strain energy stored in the beam when the crack has reached that length, while the bottom graph shows the stiffness values along the beam length. The cross-sections to the right show the latewood (dark) distributions at different points along the flatsawn beam used in this analysis.**

The nonlinear strain energy plots of Figures 4.12 and 4.13 shows a continuous increase in stored energy, even when there is a decrease in slope. This is because the beam's energy as a function of length is the summation of the energy stored in all regions prior to that

point.

But it is the local strain energy that determines whether or not fracture will occur. For this reason the numerical integration *dU/dx* from Equation 4.7 was used to create Figure 4.14, where P = 10 N, b = 20 mm, and E_o = 6.24 GPa. The periodic waviness caused by the angled composite non-homogeneity is more pronounced in the local strain energy. It should also be noted that a change in *dU/dx* with a change in *x*, or d^2U/dx^2, are greater for larger values of *x* due to *dU/dx*'s dependence on x^2.

$$\frac{dU}{dx} = \frac{P^2}{2}\left(\frac{x^2}{E_o I(x)}\right) \qquad \textbf{4.7}$$

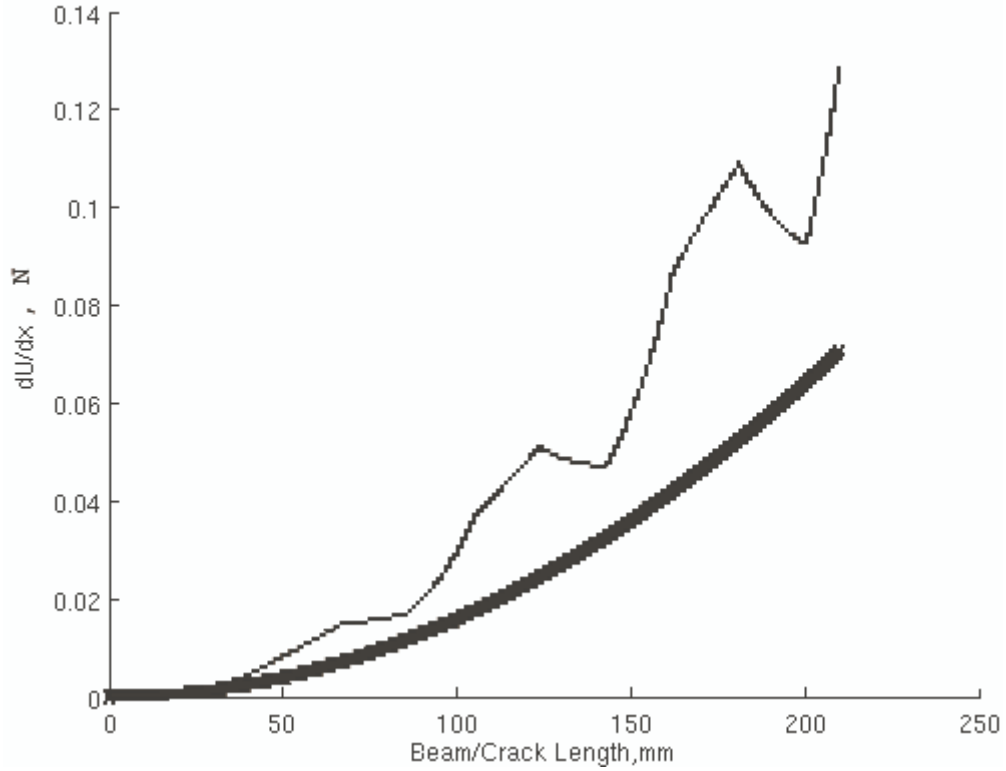

Figure 4.14: A plot of *dU/dx* vs. beam/crack length for a beam with a 3° grain angle and a beam assuming solid latewood (smooth lower bound line).

Noting *dU/dx*'s dependence on P^2, and assuming a constant critical *dU/dx* value necessary to initiate crack growth, it becomes apparent that from lower *dU/dx* values

larger loads are necessary to achieve the critical value. For both the isotropic and angled orthotropic cases this explains the greater loads necessary for fracture at small crack lengths in a DCB. But the periodic drops in *dU/dx* for the angled composite could also affect the length the crack extends, depending on the bond's arrest fracture energy and the position of the initial crack. The stiffness variations could also explain the phenomenon of critical loads at a subsequent crack length possibly being greater than the previous critical load. Rewriting Equation 4.7, Equation 4.8 was used with a Matlab script (Appendix A1) to solve for critical load P_c. Figure 4.15 was made by assuming a G_{Ic} value of 270 J/m^2 (the average G_{Ic} value from the phenol formaldehyde SYP bonds from Chapters 2 and 3) for a flatsawn system with a 3^o grain angle converging on the bondline and a growth type distribution shown in Figure 4.13.

$$P_c = \frac{\sqrt{bE_{xx} I G_{Ic}}}{x} \qquad 4.8$$

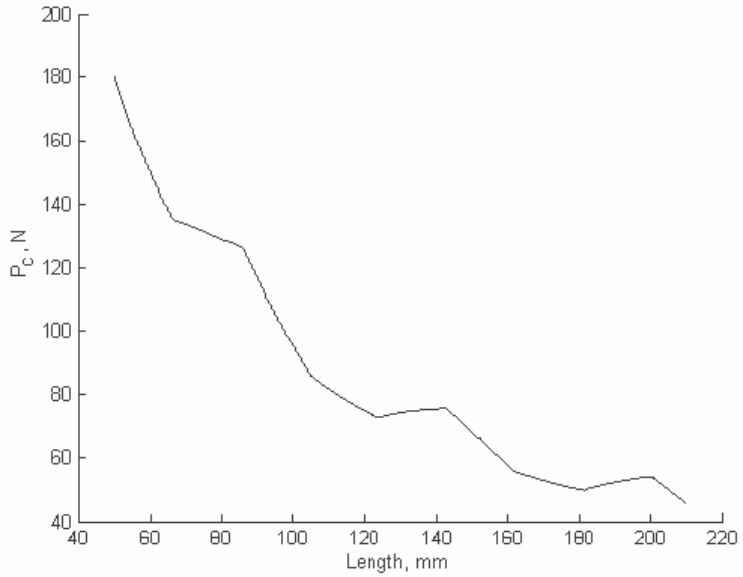

Figure 4.15: The calculated critical load, P_c, for a specimen with a flatsawn grain orientation and longitudinal grain converging on the bondline at 3^o angle, assuming a strain energy release rate, G_{Ic}, of 270 J/m^2.

Shown in Figure 4.16 are the cross-sections from fractured specimens which showed the behavior described above. For example, specimen Bd18s4 at a crack length of 14.7 cm, the 10th cycle had a lower critical load than the 11th cycle, as can be seen in the load vs. displacement profiles in Figure 4.17. The cross-section at the crack tip for the 11th cycle showed a greater amount of latewood at the outer edges of the individual beams than the cross-section at the crack tip of the 10th cycle, indicating a greater effective stiffness, $(E_{xx}I)_{eff}$.

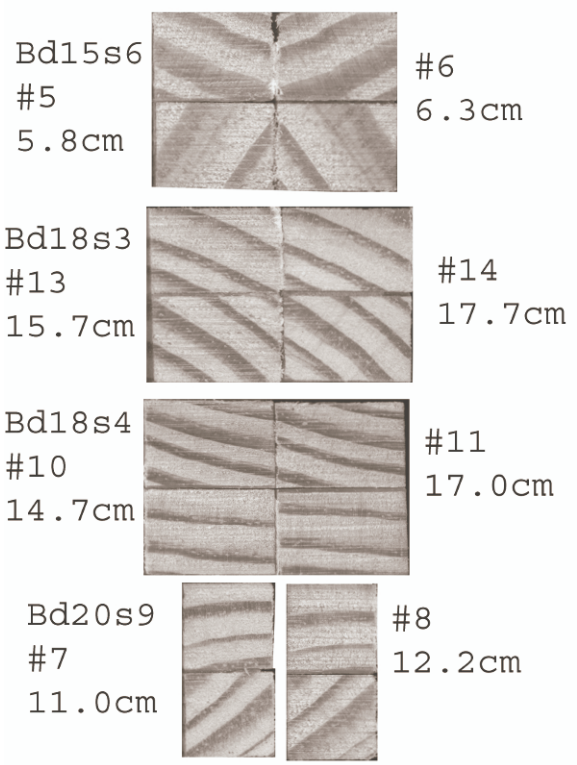

Figure 4.16: **Cross-sections from various specimens at the crack lengths showing higher critical loads in the later cycle.**

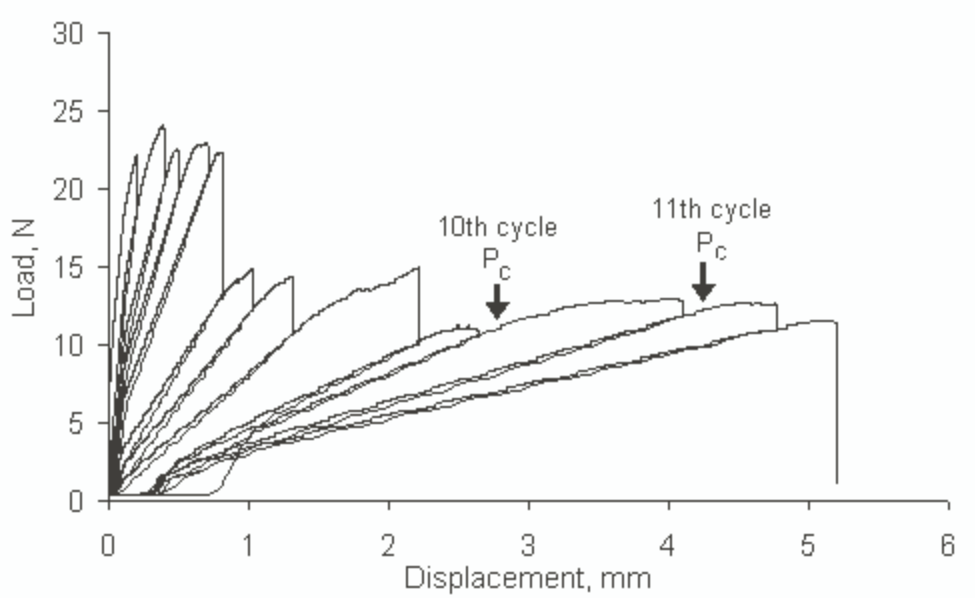

Figure 4.17: Load vs. Displacement profiles from Epoxy-SYP DCB specimen Bd18s4, with the 11th cycle's critical load being greater than the 10th.

Figure 4.17 shows an example of the phenomenon observed in Figure 4.15, where subsequent critical loads can be greater than the previous. Of course depending on the initial crack locatation, the critical load could actually be less than what would be expected, if *dU/dx* was at a local maximum. Also potentially affected is the arrest load, arrested crack length, and the amount load drops with crack extension. Stable slow crack growth during the hold period following crack initiation was frequently observed. The stable growth indicated a slower release of the strain energy stored in the beams. If a crack extension leads the specimen deeper into a *dU/dx* valley, there may be an insufficient amount of local energy for further growth. Stunting crack growth in this manner would be a source of variation for the change in crack length for a cycle.

Ultimately the system's dependence on the above considerations does not indicate wood DCB's are unreliable or invalid. The stiffness difference between late and earlywood grain is inherent in the nature of wood. Since the nature of wood cannot be removed from this experiment without removing the wood itself entirely, the stiffness

variations must be considered a property of the wood DCB. Error originates because current analytical methods are unable to take into account the local variations while using global variables such as crack length correction, α, specimen compliance, C, and effective stiffness, $(E_{xx}I.)_{eff}$.

4.3.3.2 Vertically oriented grain

Examples of more vertically oriented end grain converging against the specimen side are shown in Figures 4.3 and 4.4, also illustrating the grain angle against the specimen side as viewed from the top. A Matlab script, given in Appendix A2, was used to explore the effects of grain distribution and angle, assuming a quartersawn beam. The results were similar to the analsyis of flatsawn beams, however simply not as pronounced. This is because the changes in stiffness of quartersawn beams with longitudinal grain converging against the beam side at an angle were not as great as the stiffness changes in the flatsawn case, as shown in Figure 4.10.

Assuming a G_{Ic} value of 270 J/m^2, the critical load, Pc, at different crack lengths was calculated with Equation 4.8 for a quartersawn beam with a 3^o grain angle. The latewood and earlywood distribution was the same presumed to produce Figure 4.10, with latewood growth 1 mm thick and earlywood growth 2 mm thick. Clearly the curve is much smoother, lacking the pronounced waviness of the flatsawn case.

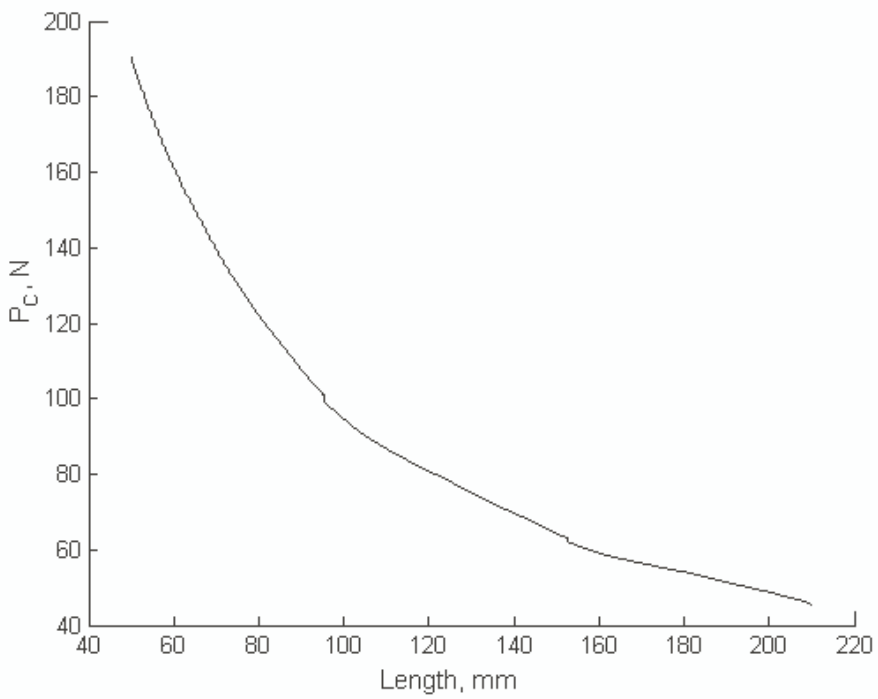

Figure 4.18: Calculated critical load, P_c, assuming a G_{Ic} value of 270 J/m^2, for a quartersawn beam with longitudinal grain converging against the beam side at 3^o angle, and simple beam theory assumptions.

Obviously assuming strictly horizontal or vertical grain orientation is only a rough approximation. Within the width of a beam, the growth ring's curvature is noticeable, though not dominating. The end grain angles can actually be any value between 0^o and 90^o, and the grain angle measured against the bondline and specimen side can differ from 0^o to 10^o. Furthermore the two beams of a DCB may actually have great differences between their end grain angles, latewood growth thickness, and grain angles as measured from the sides and bondline. This will lead to asymmetries regarding strain energy stored in the specimen as a whole and the region local to the crack tip. The places along the length of one beam where *dU/dx* is at a local minimum or maximum will most likely not match up with the other beam. Asymmetry in the strain energy stored in the two beams will cause Mode II loading at the crack tip. This in turn may determine which interface the crack will propagate along.

4.4 Summary

The grain angle dependence of the macroscopic elastic modulus along the beam length was investigated and compared to the macroscopic longitudinal elastic modulus for SYP. For small angles, the difference between E_{xx} and E_L was considered to be negligible. Also investigated was the adhesive penetration depth's dependence on the grain angle converging on the bondline.

The influence from wood DCB specimen's grain angle when there is a stiffness difference between latewood and earlywood growth rings was explored. Particularly investigated was the effect on the stiffness variation along the length, stored strain energy at a particular load, changes in strain energy with changes in beam/crack length. These influences are used to propose a plausible explanation for the occasionally observed phenomenon of a cycle's critical load being greater than the critical load from the previous cycle. Also examined was the difference in effects between growth ring orientations that are vertically oriented as opposed to horizontally oriented across the cross-section. Vertically oriented growth rings showed less variation along the length, but it is extremely difficult to intentionally fabricate specimens with vertically oriented growth rings. Based on probable stiffness variations along an individual specimen's length, SYP DCB specimens are recommended to be fabricated with a width of 25 mm.

Chapter 5: Cyclic loading of bonded wood DCB specimens

5.1 Introduction

This chapter focuses on the cyclic loading of wood double cantilever beam (DCB) fracture specimens. An in depth literature review failed to show research on cyclic testing of wood-wood DCBs. There are strong reasons to develop a test method for cyclically loaded Mode I fracture specimens consisting of bonded wood adherends. For cracked loaded materials, cycling at loads less than the critical static load could still cause crack propagation, though at a different growth rate. A fractured system may show excellent resistance to failure from monotonic loading and poor resistance to cyclic loading. Considering the wide range of real world applications in which wood adhesive bonds with potential cracks are subjected to cyclic loading, characterizing a wood-adhesive system's behavior during cyclic loading is extremely important. The specimen geometry used in this chapter will be the flat DCB geometry developed by Gagliano and associates (2001), which was further investigated for quasi-static loading in previous chapters.

In the early 1960's Paris first proposed analyzing the crack growth rate, *da/dN*, of a fracture specimen under cyclic loading in relation to the range of applied stress intensity factor, ΔK. The research described in this Chapter used the range of applied Mode I fracture energy ΔG_I, based on Mode I fracture energy G_I derived in Chapter 1 and given in Equation 5.1, where $(E_{xx}I)_{eff}$ is the adherend effective stiffness, *b* the specimen width, P the applied load, *a* the crack length, and α the crack length correction factor. ΔG_I is proportional to the square of ΔK_I. If the ΔG_I range applied is wide enough, plotting *da/dN* against ΔG_I on a log-log graph should show three distinct regions, as illustrated in

Figure 5.1 (Dowling, 1999).

$$G_I = \frac{P^2(a+\alpha)^2}{b(E_{xx}I)_{eff}} \qquad \textbf{5.1}$$
$$\Delta G_I = G_{I\max} - G_{I\min}$$

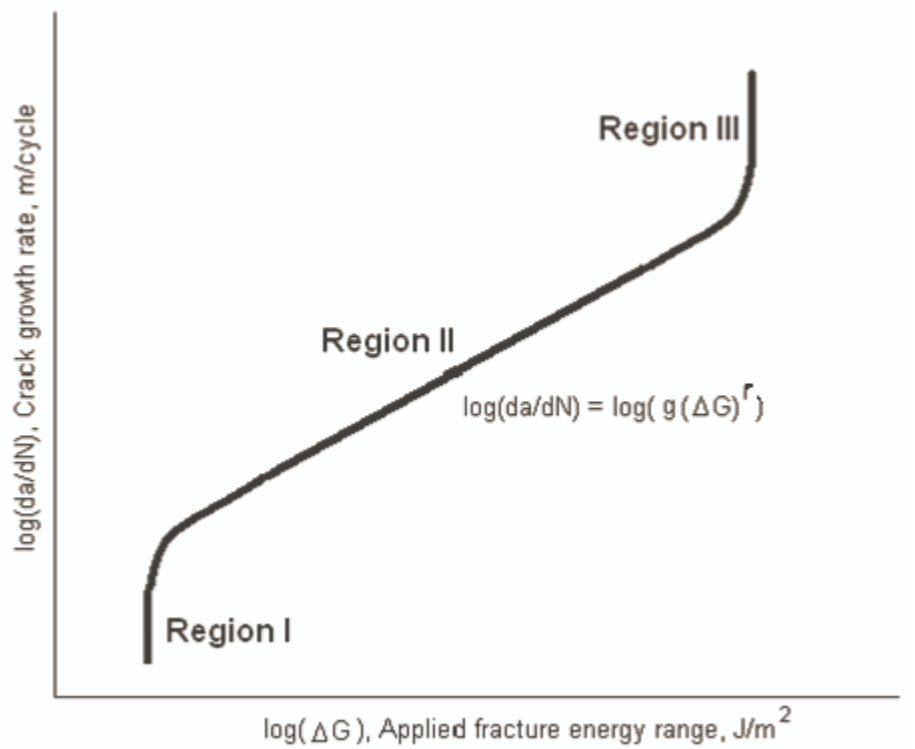

Figure 5.1: Paris plot showing three distinct regions of crack growth rate, da/dN, behavior under applied Mode I fracture energy range ΔG_I.

Region I indicates the lower bound threshold value for applied ΔG_I, meaning the crack essentially does not grow if the applied ΔG_I is less than this amount. Likewise Region III indicates the upper bound critical value, corresponding to the fracture energy from monotonic loading. Typically the crack growth rate in Region II is linear, becoming nonlinear near Regions I and III, following Equation 5.2, where *g* and *r* are constants particular to the fracture system.

$$\frac{da}{dN} = g(\Delta G_I)^r \qquad \textbf{5.2}$$

A typical DCB specimen under load control conditions will experience increases in applied ΔG_I with crack growth due to the longer moment arms leading to a greater applied stress at the crack tip. Under displacement control ΔG_I decreases with crack extension due to the increased compliance requiring less applied load to reach the same displacement. For the typical specimen this means that if the initial data point falls in Region II, then the fracture energy applied to the advancing crack length should increase (or decrease for displacement control), until the critical limit is reached or the entire specimen is fractured.

Region II's slope, domain and ΔG_I range can be used to indicate an adhesive system's suitability for different applications. For instance a bond may have a high critical fracture energy value, but if Region II has a wide ΔG_I range and a low slope within a high *da/dN* domain, a lower cyclically applied ΔG_I will propagate crack growth more quickly, leading to earlier failure. But if a bond system with a low critical fracture energy, G_{Ic}, has a large Region II slope within a low *da/dN* domain, cyclically applied loads below G_{Ic} will take much longer to propagate crack growth. If the cyclic load is to remain constant with increases in crack length, it may be better to use the latter system due to its superior durability. If the quasi-static G_{Ic} and arrest energy, G_{Ia}, values were the only determining design criteria for a real world application, the former bond system would be mistakenly chosen.

Typically for metal fracture specimens, increasing the load ratio, *R*, (defined as the minimum applied load, P_{min}, divided by the maximum applied load, P_{max}) shifts all Paris plot data points to higher ΔG_I regions without changing the Region II slope.

However the tests should be independent of changes in the load range, ΔP, as long as the R ratio remains constant (Dowling, 1999).

For this work phenol formaldehyde (PF) southern yellow pine (SYP) double cantilever beams (DCB) were constructed as described in Chapter 2. The specimens were fabricated to a width of 20 mm, following the recommendations of Chapters 3 and 4. At anticipated load levels, cyclic loading fracture tests on an individual specimen were expected to last for a couple weeks in an open environment with uncontrolled relative humidity. For this reason the specimens were coated with oil-based aluminum paint, shown to have negligible penetration depth in Chapter 3, to maintain near constant moisture content within the specimen during a test. This minimized the influence moisture adsorption or de-adsorption would have on the observed behavior.

5.2 Methods and Materials

5.2.1 PF-SYP DCBs

In Chapter 2 three PF-SYP DCBs were tested under quasi-static loading to determine the critical and arrest fracture energies. For the present study of fatigue testing, PF-SYP DCBs were prepared in the same manner described in Chapter 2. Within 90 minutes of being removed from the hot press all specimens were coated with aluminum paint to maintain moisture control. In Chapter 3 the paint penetration was shown to be negligible. A clamp was applied at approximately 50 mm past the fixture holes in order to restrict crack growth beyond that point while a sharp wedge was tapped into the bondline to make an initial crack.

As reported in Chapter 2, the G_{Ic} values from individual crack lengths ranged from below 200 J/m^2 in one specimen to above 360 J/m^2 in another, with an approximately 10% coefficient of variation for each specimen. The average G_{Ic} value for

the three specimens was 272 J/m^2. The plots of the cube root of compliance, *C*, versus crack length, *a*, had very good linear fits. The square of the Pearson product moment correlation coefficient, R^2, was over 0.98. No trends, such as increasing fracture energy values with increasing crack length, were apparent in the specimens taken as a whole. As discussed in Chapter 2, a specimen may have a higher critical load but lower critical fracture energies compared to other specimens. This is due to variations in effective stiffness, $(E_{xx}I)_{eff}$, and crack length correction, α, which ranged from 17 mm to 33 mm.

5.2.2 Cyclic loading and fracture of PF-SYP DCB

Cyclic loading was performed using a horizontal MTS Tytron 250 Microforce Testing System with a 250 N load cell and a linear induction motor on air bearings controlled by a dual loop PID control system. A Matlab script (Appendix *B*) was used to extract from the computer-recorded data array the maximum and minimum load and displacement points. The script also calculated the average cycle compliance from the data points lying between the two extremes.

Prior to mounting, typewriter correction fluid was painted along the bondline and a graduated paper scale was bonded to the side. A sharp wedge was used to create an initial pre-crack of about 50 mm. After mounting, the specimen was enclosed in two large plastic bags and sealed with vacuum tape, with a humidity sensor running to the inner bag, as shown n Figure 5.2. A small amount of anhydrous calcium sulfate desiccant was placed in the outer bag. A string, shown in Figure 5.3, leading from a ring stand held up the beam's end. The string moved with specimen end and was long enough to ensure out of plane displacements caused by the swinging string were negligible for large horizontal movement. Testing was performed under load control, using sinusoidal

loading with a frequency of 3 Hz and a load ratio, *R*, or 0.5. A lighted magnifying glass was used to measure the crack length from the specimen's side while the test was running.

Figure 5.2: **Photograph of a PF-SYP DCB fracture specimen inside two plastic bags mounted in the cyclic testing system, with desiccant, humidity sensor, and load cell indicated.**

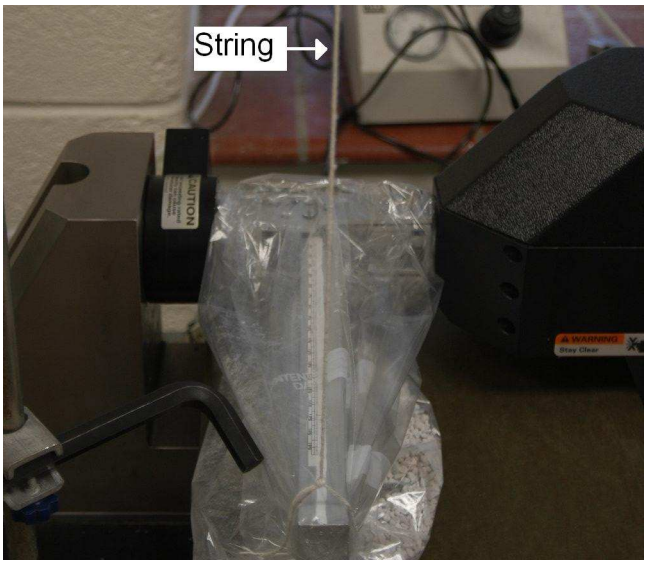

Figure 5.3: **Another view of the PF-SYP DCB fracture specimen, with the long support string indicated.**

5.3 Results and Discussion

5.3.1 Moisture control of specimens

The wood DCB fracture specimens used in this work were coated in aluminum paint to control moisture content. The moisture content control was necessary because wood mechanical properties are dependent on moisture content and the specimens were tested for long durations in a lab with fluctuating environmental conditions. According to Green et al. (1999), oil type preservatives do not react with the wood and cause significant loss in strength. Green and colleagues estimate for SYP that wood with a 17% moisture content by weight has an elastic modulus 14.1% greater than the modulus of wood with a 12% moisture content. SYP with a 7% moisture content has an elastic modulus 12.3% less than the modulus of SYP with a 12% moisture content. However, they also note that mechanical characteristics can reach peak values, decreasing with further decreases in moisture content. Fluctuating stiffness changes throughout the duration of the test is a source of error for determining critical strain energy release rate. After the paint dried, all specimens were weighed and then stored in two sealed plastic bags to provide further protection against moisture content change. Over a period of 90 days, the specimen weight gain due to moisture absorption was approximately 0.6%. For SYP this causes a 1.6% drop in elastic modulus, which was considered negligible. Consequently, the experimental conditions prevented any significant changes in wood moisture.

5.3.2 Softening behavior

Initial attempts to perform testing using displacement control were abandoned because maintaining a constant load ratio was too difficult. The difficulty was attributed to the softening of the wood adherends. For this reason subsequent testing was

performed using load control. Under load control, as the crack grows the applied strain energy increases. Therefore the expected crack growth rate should increase as the crack grows, though this work shows crack growth to be a more complicated matter for fatiguing wood DCBs. A load ratio, defined as the minimum applied load, P_{min}, divided by the maximum applied load, P_{max}, of $R = 0.5$ was chosen due to difficulties in having the testing machine maintain lower load ratios. The average load ratio applied for all data points recorded was R = 0.501 with a coefficient of variation of 0.38%.

Shown in Figure 5.4 are the load vs. displacement curves for two loading cycles acquired while the crack length remained constant at 51 mm. A slight hysteresis is visible, apparently not changing in size with cycling. The hysteresis shifted to the right from the 200th cycle to the 1900th cycle, while load control maintained relatively constant peak and valley loads. The displacement range of the testing machines loading arm was approximately 100 mm. Because the shift was only a fraction of a millimeter, and such a small percentage of the possible displacement range, the shift could have been caused by a drift in the testing machines set origin. However there is a likelihood the shift was caused by a softening of the wood adherends due to fatigue or damage. This is supported by the fact that the shift was continually to the right, as observed in many specimens at different crack lengths, and that the increases in displacement were outside the range of machine error and sensor background noise, as will be shown later. A drift in the machine set origin would have been in the positive or negative direction, not only continuously to the right.

The hysteresis could have been due to a viscoelastic damping in the wood adherends, but was more likely caused by the set up of the testing machines control

system. A low pass filter was applied to the load signal while no filter was applied to the displacement signal. This caused a phase lag between the two signals, possibly resulting in a hysteresis. Whether or not the hysteresis was caused by viscoelastic damping or only by the phase lag between the load and displacement signals is significant. A hysteresis caused by damping represents a dissipation of energy with each cycle. The fracture analysis methods for calculating ΔG_I used in this research do not take into account energy being lost to damping. Instead ΔG_I was calculated using the average cycle compliance, which was calculated using only the changing peak and valley load and displacement points. Regardless, the hysteresis size and shift was small, meaning the amount of energy possibly dissipated by damping or damage from an individual cycle was small. However, considering that millions of cycles were applied, the accumulated energy loss may have been significant.

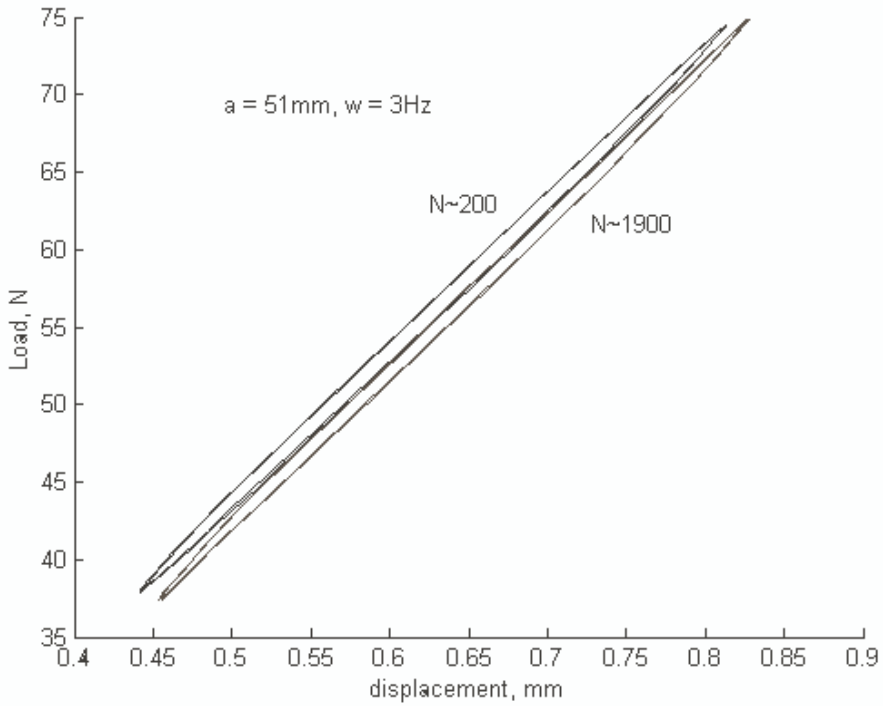

Figure 5.4: Shifted load-displacement hysteresis loops from the 200th and 1900th cycle prior to crack growth in a PF-SYP DCB specimen.

5.3.2.1 Wood softening background

A literature search failed to show any research exploring softening specifically in wood's radial or tangential directions, the orthotropic directions which determine E_{yy}. However, Tsai and Ansell (1990) published a broad review of the fatigue behavior of wood and wood products in longitudinal bending. Softening was typically attributed to decreases in the longitudinal stiffness, E_{xx}. For research with the bending loads near the static strength, Tsai and Ansell noted that the ultimate strength did not decrease while the modulus of elasticity decreased with each cycle. The greatest decrease occurred after the first cycle. However they note other research showing increases in modulus. And they cite other examples where the modulus remained constant but the residual strain after each cycle increased according to a power law model. This behavior was found to be independent of species if the fatigue strain, not the fatigue stress, was the same. Decreases in acoustic emissions, creep, strain rate, and modulus rate with each cycle all indicate the damage contribution from each successive cycle decreases.

Tsai and associates performed bending fatigue tests on Sitka spruce at 75% of static flexural strength. Damage was visually observed in the form of compression kinks within 500 cycles, though the estimated life is 10^7 cycles. A compressed kink in one cell creates stress concentrations and early failure in adjacent cells, starting from the edge and leading to the neutral axis. The weakened compressive region required a greater area to bear the same bending load, moving the neutral axis towards the tension side (Tsai et al., 1990). However this mechanism does not occur in the fatigue testing described in this chapter since the compliance drops with crack growth, as discussed above. As would be expected, experimentation showed that maintaining the same peak load and increasing the R ratio increases the number of cycles to failure, with negative ratio's failing the

quickest. For a measure of comparison, assuming simple beam theory and ignoring stress concentrations at the crack tip, a 75 N load on a SYP-DCB specimen with a 100 mm crack length causes +/- 12.5 MPa of maximum bending stress, or 16% of tensile and 25% of compressive failure stresses (Green, 1999).

5.3.3 Cycle compliance changes

Also of interest is the change in compliance with each cycle for the same crack length. The hysteresis loop shift leads to changes in three different compliances: peak compliance, valley compliance, and cycle compliance. Figure 5.5 illustrates the three compliances on a load versus displacement plot. The peak compliance is defined as the compliance between the load-displacement origin and the peak load-displacement point. The valley compliance is similarly defined, but using the valley load-displacement point. The cycle compliance, which in this research is the compliance used to calculate G_I, is the compliance between the peak and valley load-displacement points. As can be seen from Figure 5.6, within 1800 cycles, the cycle compliance drops 3.1%. The roughness of the plots is attributable to fluctuations in machine control and sensor background noise.

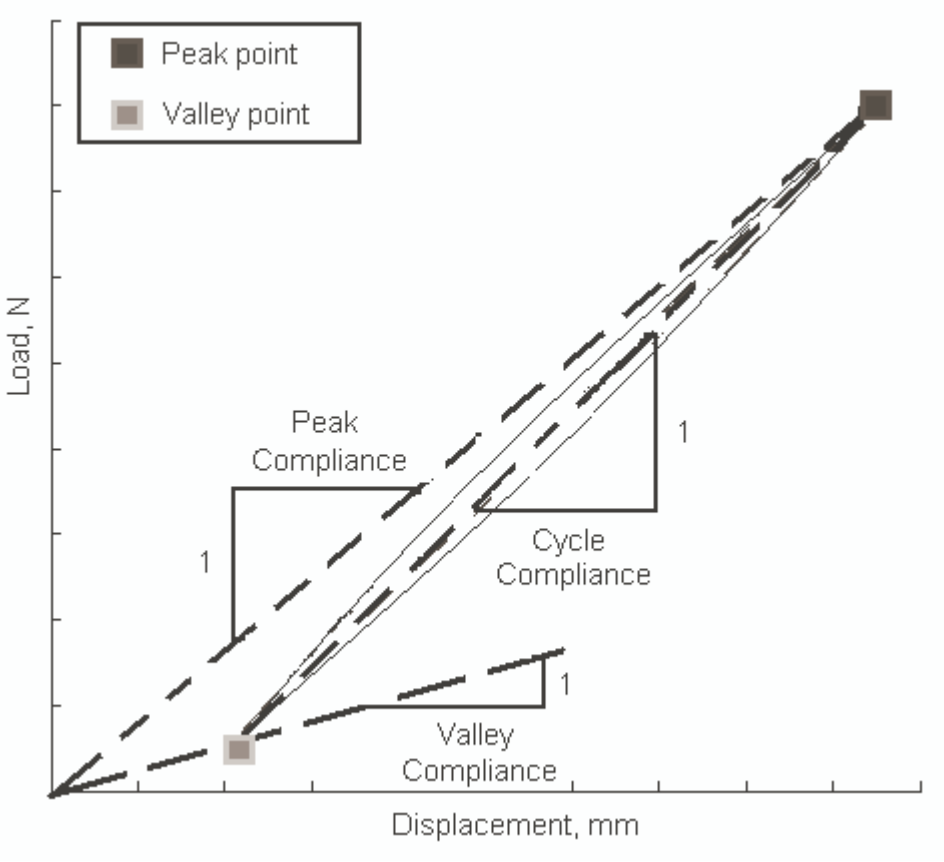

Figure 5.5: Illustration of the peak, valley, and cycle compliances on a load versus displacement plot.

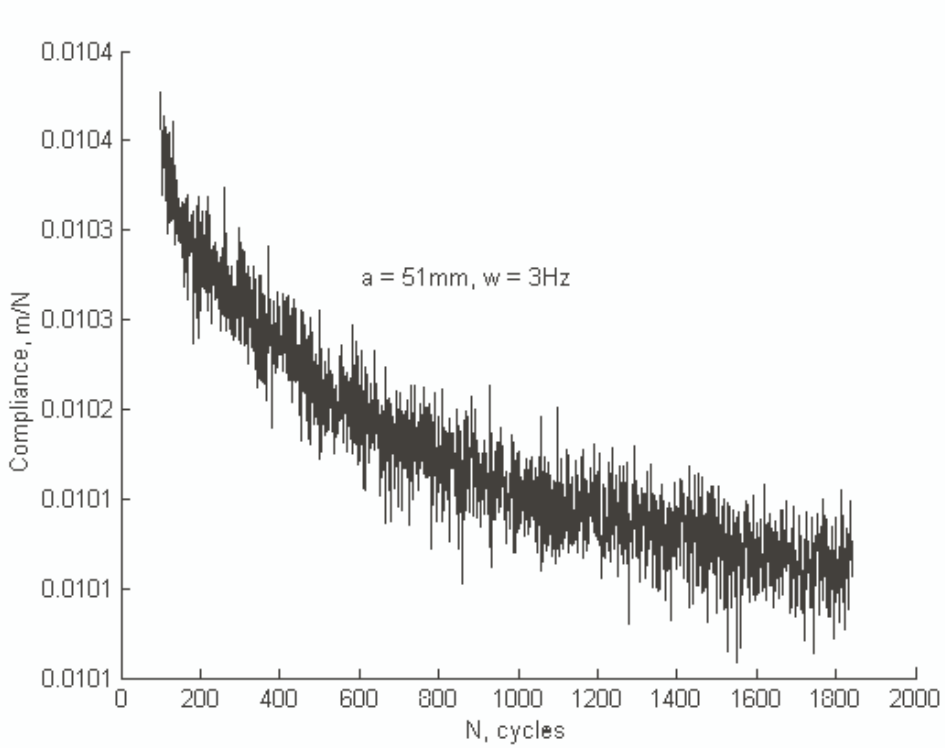

Figure 5.6: The decreasing cycle compliance plotted against cycle count, N, from a PF-SYP DCB fracture specimen with a crack length of 51 mm loaded at 3 Hz.

Figure 5.7 shows a plot of the normalized cross-head displacement for lower bound, δ_{min}, and upper bound, δ_{max}, displacements as a function of cycle count, *N*. Clearly δ_{min} shows a greater proportional increase than δ_{max}. While all displacements are increasing, meaning the peak compliance and valley compliance are increasing, the cycle compliance is decreasing, resulting in the drop shown in Figure 5.6. Plausible reasons for this behavior will be discussed later. Obviously the average increases in peak and valley displacements are outside the range of machine control and sensor background noise.

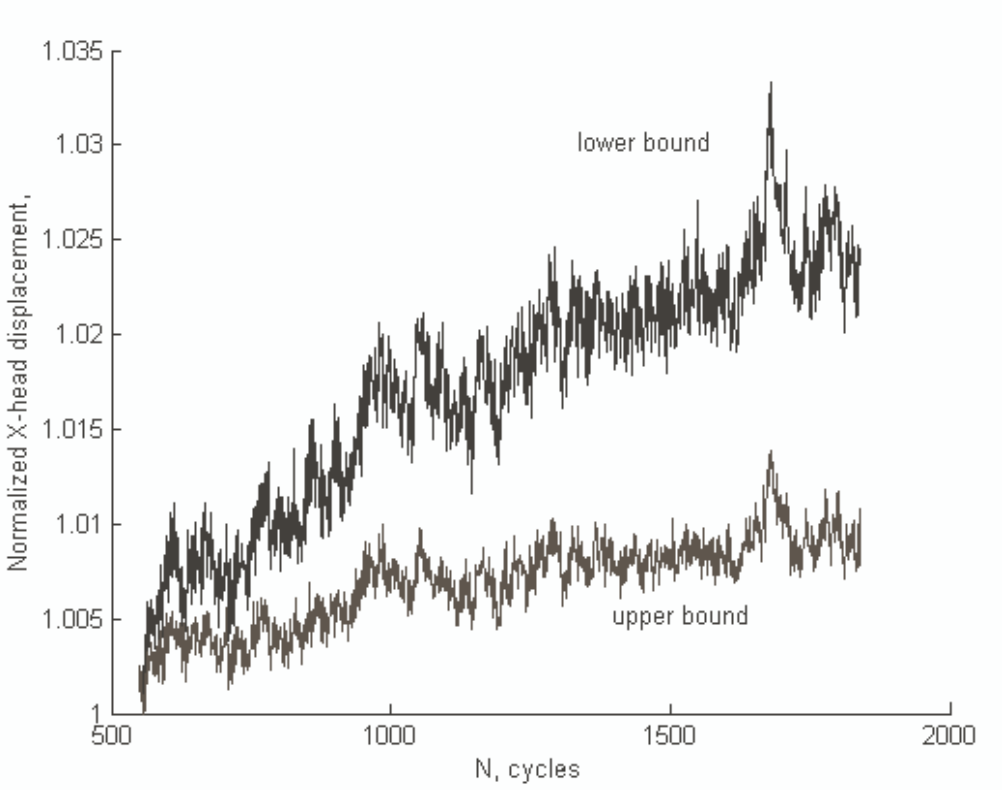

Figure 5.7: **The normalized lower bound and upper bound displacements plotted against cycle count, N, from a softening PF-SYP DCB fracture specimen maintaining constant crack length.**

A cycle compliance change during constant crack length is relevant considering the strain energy release rate is calculated from the change in cycle compliance with a change in crack length. The cycle compliance is calculated from load and displacement data recorded from the testing system user interface, not from machine recorded data. This is because recording the necessary information would produce an overwhelming amount of data. If the cycle compliance changed before the crack length extended, the actual and calculated change in cycle compliance would not be the same. Furthermore the crack length correction, α, most likely changed with cycling because of its dependence on the changing material properties. So the initial and final crack length correction differed from the averaged correction value obtained from the cube root compliance versus crack length plot. Both of these issues are contributions to error in

calculating ΔG, the significance of which has not been determined.

Figure 5.8 shows crack lengths and normalized compliance plotted against the cycle count. As expected, the cycle compliance increased overall as the crack length increases. However there are several examples of decreases in cycle compliance, corresponding to recent increases in crack length. If local changes in cycle compliance were used to calculate the applied fracture energy, G_{Ic} would be negative because at these points, dC/da is negative. For this reason the global increase in cycle compliance is used to determine dC/da, as determined from the plot of $C^{1/3}$ vs. crack length, a.

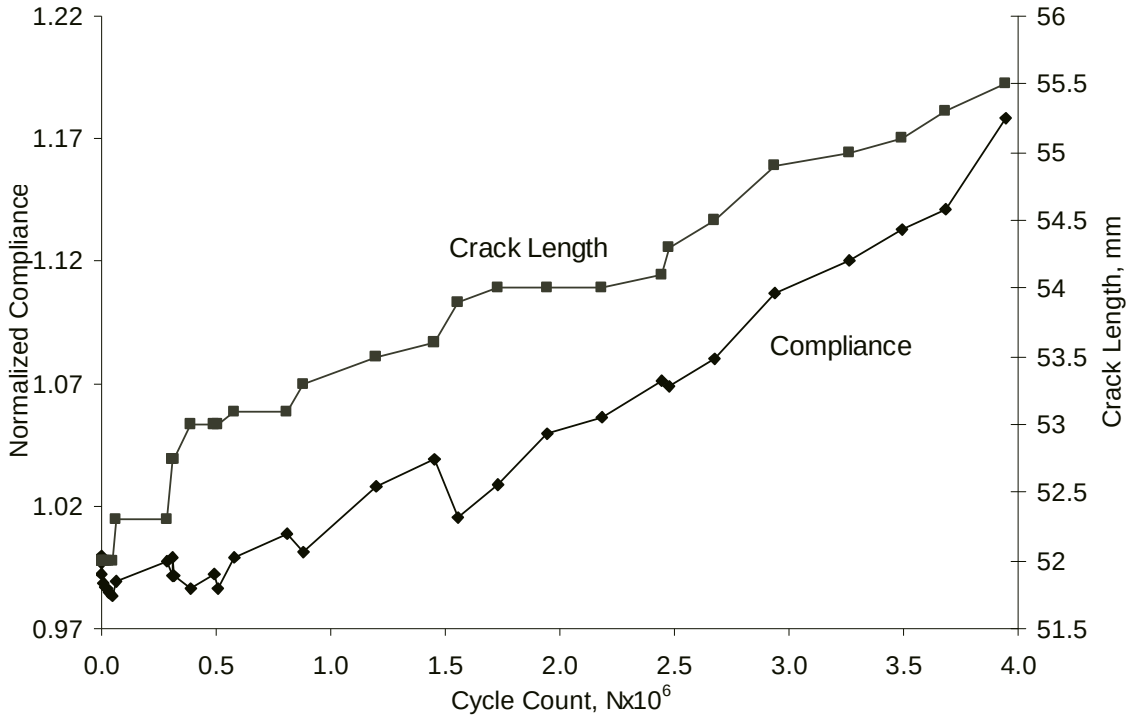

Figure 5.8: Measured crack length and corresponding normalized compliance as a function of cycle count, *N*, with a load ratio *R* = 0.5, and peak load of 75 N.

The crack lengths in Figure 5.8 are approximately 53 mm in length, with low applied fracture energy. Specimens tested at greater crack lengths and higher applied fracture energy with faster crack growth rates demonstrated different compliance changes with crack extension, as shown in Figure 5.9. The dependence of dC/da on crack length

and crack growth rate could influence the Region II slope values and the toughening behavior discussed later.

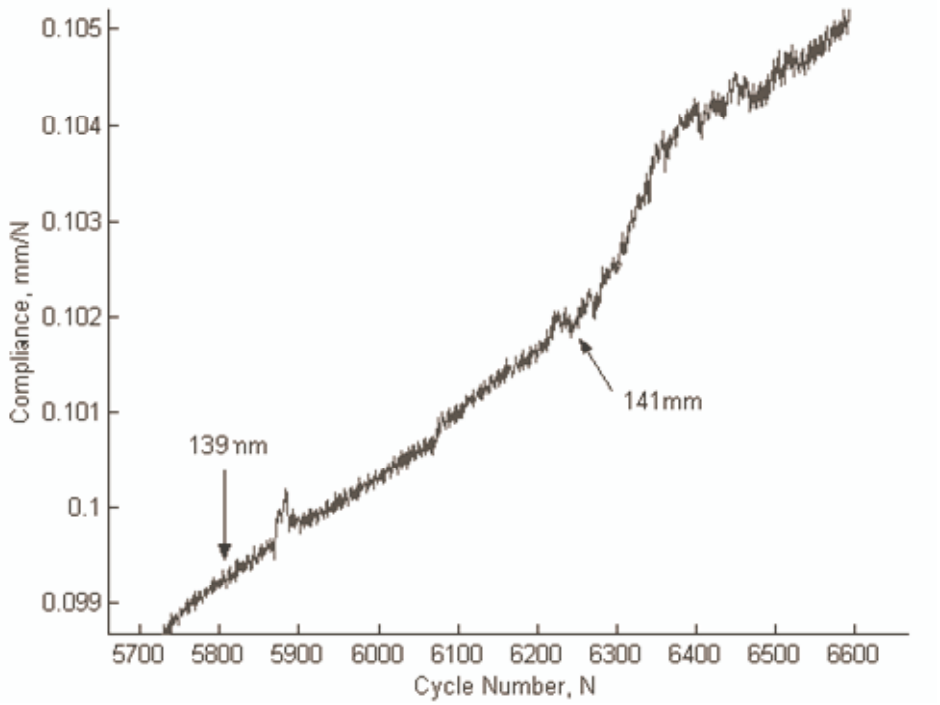

Figure 5.9: Calculated compliance plotted against cycle count from a softening PF-SYP DCB, with indicated crack lengths of 139 mm and 141 mm, with a load ratio *R* = 0.5, and peak load of 60 N..

Plotting the load and displacement in conjunction for cycles around a known crack extension shows interesting behavior, as shown in Figures 5.10 and 5.11. Prior to 5650 cycles, the crack length was measured to be 138 mm; after 5725 cycles the crack length is 139 mm. With crack extension, the maximum displacement dropped, which is understandable because the max load also dropped. However, the minimum load increased while the minimum displacement decreased. This indicates stiffening with crack growth. When the crack arrested, the softening resumed with the peak and valley loads remaining relatively constant while peak and valley displacements increased.

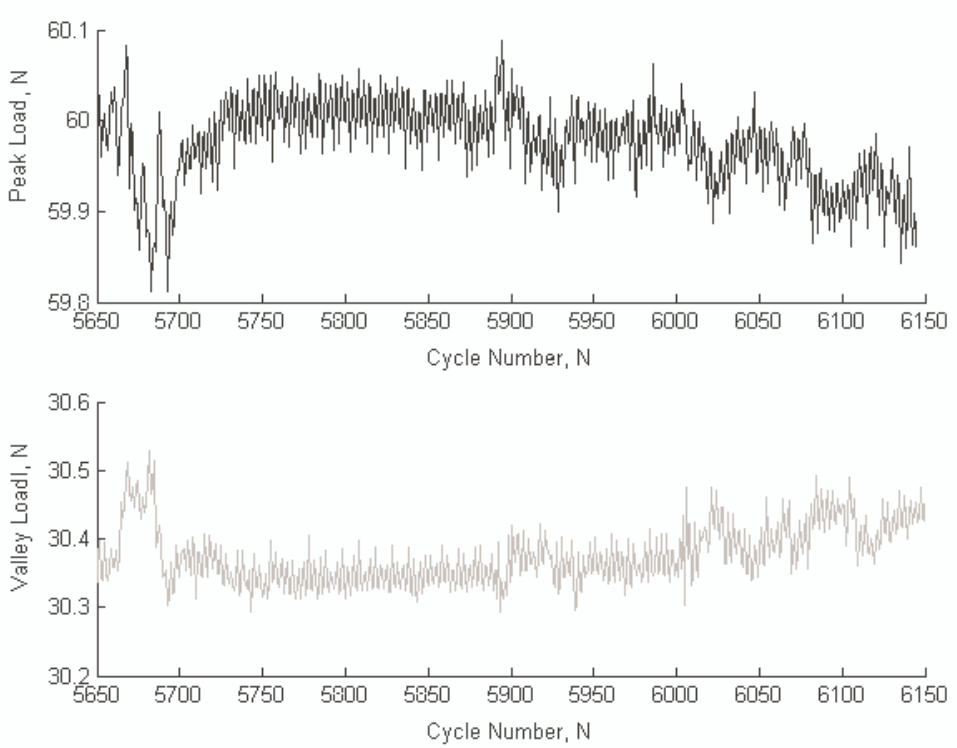

Figure 5.10: Lower and Upper bound loads applied, with crack growth at cycle counts of 5650 and 5725.

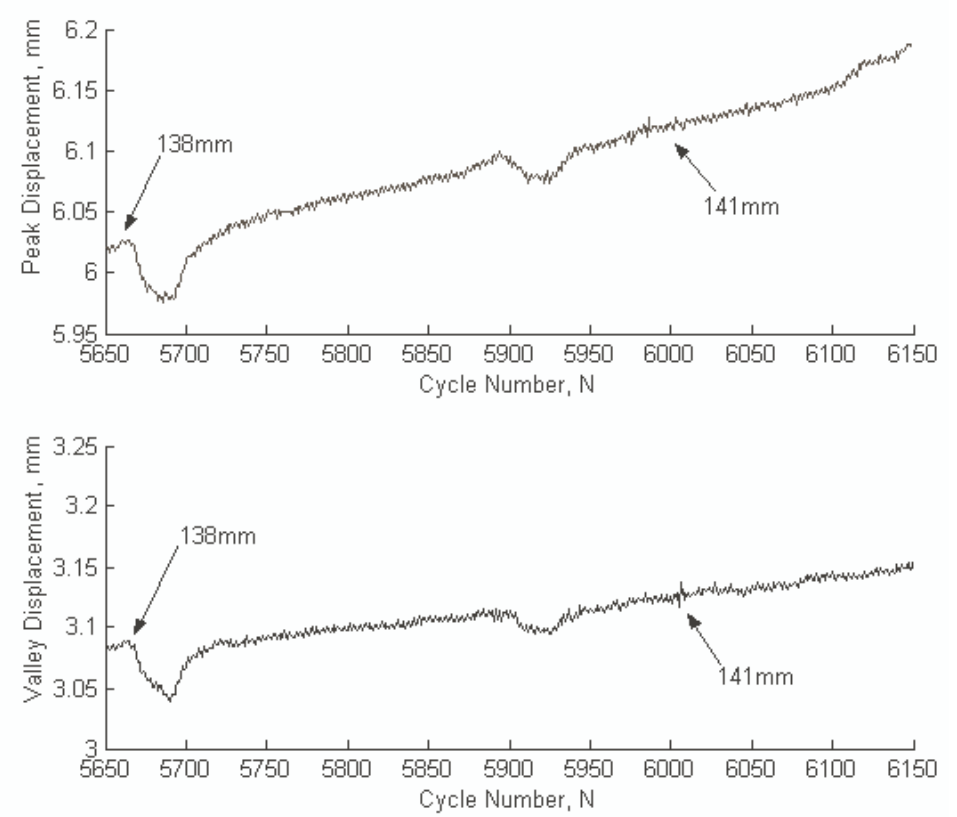

Figure 5.11: Lower and Upper bound displacements applied, with crack growth at cycle counts of 5650 and 5725.

The load deviation from the set constant is typical of dual loop PID controlled systems. When a loaded specimen changes stiffness, several cycles are required for the control system feedback response to return the system to the desired state. The number of cycles required to return to the set load will depend on the specimen stiffness change and the accuracy of the controller's "tuning", which refers to the appropriateness of the outer loop's control settings. When the control system was not able to make self-adjustments quickly enough, the proportional control value, P, was manually adjusted during testing to maintain the correct applied load.

For quasi-statically loaded PF-SYP DCBs, crack length correction, α, values range from 17 mm to 33 mm, as discussed in Chapter 2. If α is taken to indicate the scale of the region in the wood adherend bearing load ahead of the crack tip, this means a static test crack extension of 10 mm brings the crack tip stresses into a new region of the substrate. But fatigue crack extensions are typically 0.5 mm or less, meaning crack growth is considerably smaller than the regions experiencing fatiguing strains created by the crack tip and beam rotation. Whether the compliance will increase or decrease is only dependent on which increases more, the minimum or maximum displacements. The rate at which displacement values increase may be dependent on several factors and complicated fatiguing mechanisms – the determination of which is beyond the scope of this project. However, the position of wood growth types does not change greatly with 0.5 mm extensions, indicating cyclic loading induced crack extensions would not bring the crack tip near different growth types.

The softening is not believed to be caused by a decrease in longitudinal shear moduli, but rather the vertical modulus, E_{yy}. This is supported by the observation that the

beam stiffness increased with crack growth. The beam's compliance is dependent on the longitudinal and shear moduli along its entire length, whereas the local compliance is only dependent on E_{yy} in the crack tip region. If the longitudinal or shear moduli had decreased, then the beam's stiffness would be permanently decreased, never increased with crack growth.

5.3.4 Paris plot results and discussion

Initial crack lengths were created in the DCBs by tapping a wedge into the bondline with a clamp near 50 mm past the specimen's fixture holes, preventing crack growth past that point. The specimen was then cyclically tested at that crack length. When performing the fatigue testing, the variations in bond strength caused a minor difficulty because the specimen's quasi-static critical fracture energy could not be calculated until the specimen was already broken. Considering the cyclic loading was performed under load control, the applied fracture energy increased with crack length. This means the variability in bond strength frequently led to a specimen failing rapidly along the entire length when a greater fracture resistance was expected. Similarly, fatigue crack growth was often much slower than expected because the fracture energy needed to propogate the crack was actually much higher than expected.

Frequently, after several crack extensions had been acquired and a toughening behavior was apparent, the test was stopped and the crack was monotonically driven further down the bondline (15 mm to 70 mm). The cyclic testing was then resumed at the new crack length. Crack lengths were not determined by measuring the compliance using a reference to solve for crack length, a. Instead all crack lengths were measured visually with a lighted magnifying glass.

As mentioned before, the compliance was calculated using the maximum and

minimum load and displacement values recorded from the testing system's user interface. The crack length was measured from the specimen's side with a lighted magnifying glass. As discussed in Chapters 1 and 2, the slope, m, and abscissa intercept, α, from the cube root of compliance versus crack length plot ($C^{1/3}$ vs. a) are used to calculate the range of applied Mode I fracture energy, G_I, of Equation 5.3

$$G_I = \frac{P^2(a+\alpha)^2}{b(E_{xx}I)_{eff}} \qquad \textbf{5.3}$$
$$\Delta G_I = G_{\mathrm{Im}ax} - G_{\mathrm{Im}in}$$

Figure 5.12 shows the cube root of compliance versus crack length for a cyclically tested specimen PF5-1, which was given an initial crack length of about 51 mm tested for seventeen crack extensions before having the crack monotonically driven to 129 mm and tested for 22 more crack extensions. As derived in Chapter 1, the beam's effective stiffness $(E_{xx}I)_{eff}$ and crack length correction, α, were determined using crack lengths from both crack extension groupings. The linear regression showed slopes and intercepts similar to those from the quasi-static testing, with a fit of $R^2 = 0.9998$.

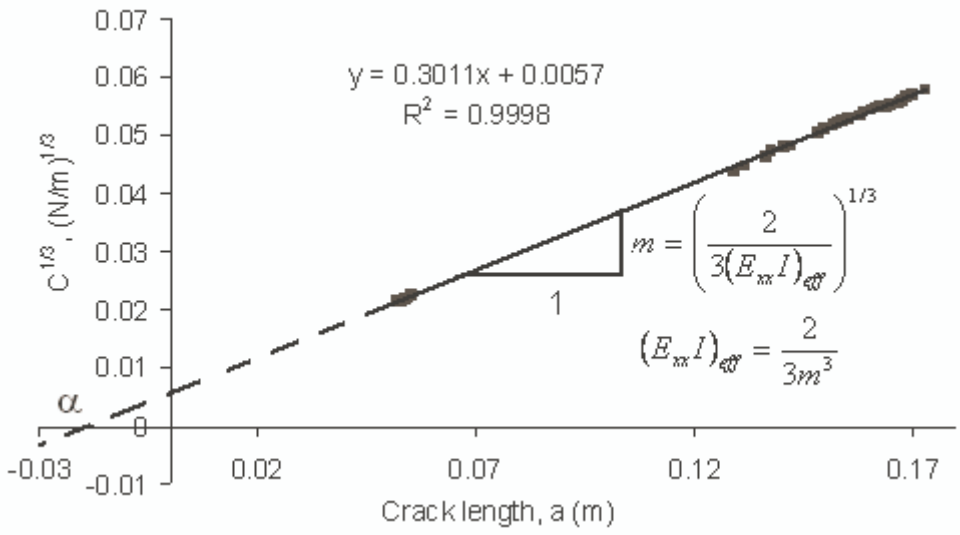

Figure 5.12: Cube root of compliance versus crack length from a cyclically loaded PF-SYP DCB specimen, with monotonically initiated cracks at 51 mm and 129 mm.

Atypical behavior is apparent plotting the logarithm of applied fracture energy range, ΔG, against the logarithm of the crack growth rate, *da/dN*. A fresh crack is initiated and then fatigued. For some specimens, as the crack extends due to fatigue, ΔG_I increases, while *da/dN* does not increase linearly, eventually leveling out or possibly declining. When new fresh crack was initiated through monotonic loading, the crack growth rate *da/dN* was much higher. But as before, with fatiguing *da/dN* does not linearly increase with ΔG_I for successive crack extensions. However, other specimens have shown linear behavior, with no apparent toughening. Figure 5.13 shows log *da/dN* vs. log ΔG_I for fatigue started from different initial crack lengths for four different specimens. The linear fit shown uses the first data points from each initial crack length, with the slope of 7.6 *da/dN* logarithmic decades to 1 ΔG_I logarithmic decade to be taken as the Paris plot's Region II slope.

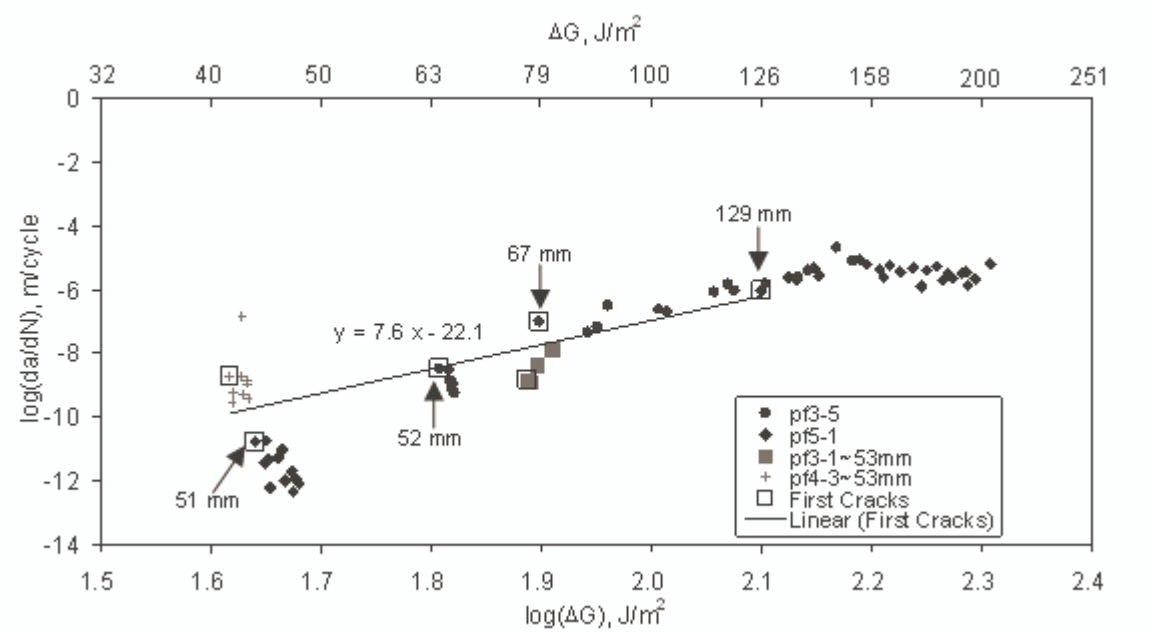

Figure 5.13: Logarithmic crack growth rate, *da/dN*, plotted against the logarithmic applied fracture energy range, ΔG, with three specimens showing toughening behavior.

There are currently four plausible components for explaining the atypical

behavior, none being mutually exclusive. The first observation is that linear behavior only occurs for a crack initiated towards the beam's center (specimen pf-3 at approximately 67 mm), while all atypical/toughening behavior comes from cracks initiated at the beam's beginning or end (51 mm or 129 mm). Though quasi-static testing showed no crack length dependence for G_{Ic}, fatigue characteristics may not have been apparent from a quasi-static test.

Also of importance is the crack opening rate, a function of crack length and cross-head displacement rate controlled by the set loading frequency. Under load control, shorter crack lengths result in slower crack opening rate while increasing crack length moment arms increases the crack opening rate. Faster loading of visco-elastic adhesives results in smaller plastic zones at the crack tips. However this alone does not explain the atypical Region II behavior because nonlinearities were apparent for both small and large but not medium crack lengths. Plausibly the calculated ΔG_I values are incorrect because the crack length correction, α, from individual crack extensions are different from the averaged value.

Another plausible explanation is that the growth rate is controlled by the degree of softening, which itself is controlled by the magnitude and duration of stress applied. Low applied fracture energy will cause little softening with each cycle, but a greater number of cycles were required to initiate crack extension. Inversely, high applied fracture energy will cause a large amount of softening with each cycle, but fewer cycles were required to initiate crack extension. Perhaps medium applied fracture energy with a moderate crack growth rate allows for the crack extension to occur before the softened region grows to a size which prevents the necessary loading being transferred to the crack tip. The actual

size and shape of the softened region is unknown, though as discussed earlier the softening is not believed to be caused by a decrease in either the longitudinal or shear moduli.

Du, Thouless, and Ya (1998) researched a crack toughening mechanism by which an energy absorbing process zone is formed in rubber-modified epoxy polymer DCBs by the crack tip and leaves a deformed wake with crack extension. Specifically the material in the process zone must experience a strain reversal if a greater load is required to initiate fracture. Monotonically increasing strain or nonlinear stress-strain behavior will not cause toughening. However, their research used quasi-statically, not cyclically, loaded specimens. Plausibly a similar phenomenon is occurring in the wood DCB's with a permanent vertical strain, as evidenced by the increased compliance and the deduced softening in the E_{yy} modulus, causing a residual contraction in the longitudinal direction. This residual compression in the longitudinal direction could create a similar energy absorbing process zone.

5.3.5 Recommendations for future work

There are several obvious weaknesses in the research described in this chapter, which is understandable considering this appears to be the first time bonded wood fracture specimens were tested using cyclic loading. The weaknesses are not necessarily inherent in the wood DCB geometry chosen, but rather possibly due to inappropriate test method choices and the inability of the applied analytical model to take into account several issues. These issues include dampening, softening and local compliance changes prior to crack growth, re-stiffening and frequent local compliance decreases with crack growth, and the residual stresses which are most likely the causes for the observed toughening mechanism.

The softening appeared while cycling at a constant crack length in tests using load control resulting in load vs. displacement curves shifted to greater displacements. The re-stiffening with crack extension strongly indicates that the softening is due to a reduction of the vertical elastic modulus, E_{yy}, as discussed earlier. The adherends around the crack tip were stretched with each cycle (which in part leads to the necessity of the crack length correction, α). Plausibly this repeated stretching lead to permanent deformations in the vertical direction, with the stress concentrations at the crack tip causing the material closest to the crack tip to undergo the greatest deformations. For this reason the adherend thickness should be increased. Assuming this does not greatly increase the vertical stresses at the crack tip, the proportion of plastically deformed material relative to the total adherend thickness would be reduced. This in turn should reduce the softening effect.

However, the toughening behavior was not always observed. This may be because the rate dependence of wood's viscoelastic nature is influencing the effective moduli, stresses, and strains and therefore yielding behavior of the wood. By controlling the loading rate at the crack tip, which is a function crack length and cycle frequency, the toughening effect could be minimized by controlling the vertical direction plasticity. However, this means there is plausibly a loading rate influence on the Paris plot Region II range and slope. Even if the toughening behavior was eliminated, the Paris plot generated by testing at one rate may not overlap the Paris plot generated at a different rate. Future work should be focused on determining if there are appropriate loading rates at the crack tip, and the influence these rates have on Region II behavior.

The plasticity in the vertical direction could also be dependent on the grain type

dominating the vertical direction. As shown in Chapter 4, the growth ring orientation spanning the cross-section is variable. The vertical direction could be dominated by radial grain, tangential grain, or any combination of the two depending on the grain angle in the cross-section. A literature review failed to show any research dedicated to studying the fatigue behavior of wood in the radial and tangential directions. Given that the radial direction elastic modulus is approximately twice the tangential direction radial modulus, the stresses in the vertical direction are dependent on growth type in vertical direction. Likewise the yielding behavior, and therefore the plausible toughening mechanism around the crack tip, are dependent on the vertical direction growth type.

Another recommendation is to investigate the influence on crack length correction, α, from both the growth type distribution near the crack tip and the plastically deformed material at the crack tip. As shown in Chapter 1, analytical models show α to be dependent on orthotropic properties from the x-y plane, including E_{yy}, longitudinal elastic modulus, E_{xx}, and the shear modulus, G_{xy}. In the research described above an averaged global crack length correction was used based on the $C^{1/3}$ versus crack length plot based on all crack lengths from the entire specimen length. For a test specimen with relatively constant mechanical properties along the length, this is an acceptable practice. But the mechanical properties of the wood adherends are changing along the entire length. This is not due just to the natural variability of wood, but also due to angles the longitudinal grain make against the bondline and specimen side, as discussed in Chapter 4 for the variations in effective stiffness, $(E_{xx}I)_{eff}$. Because α is used to take into account the material displacements behind the crack when calculating the applied fracture energy, the α associated with each particular crack should be used when calculating G_I.

Significant differences in α, caused by differences in growth type and vertical direction softening, will result in significant differences in the applied G_I calculated. The averaging α used in this research did not take those differences into account. Future research should be directed towards understanding how to take into account changing values of α and $(E_{xx}I)_{eff}$.

5.4 Summary

A novel method for performing cyclic fatigue fracture testing of wood double cantilever beams has been developed. Precautionary measures have been taken to prevent moisture content changes in the specimen during the testing period, which could last for several days. This ensures the behavior observed is not due to moisture adsorption or desorption. During cycling at the same crack length a softening was observed, whereby the average displacement increased while the average load remained constant. In some instances the maximum displacement increased faster than the minimum, causing the local compliance between the points to increase. In other instances the minimum displacement increased faster than the maximum displacement, causing the local compliance between the points to decrease. Recommendations were made for future research to make testing bonded wood-wood DCBs using cyclic loading a more viable and valid test choice.

Chapter 6: Summary

The primary direction of this thesis was towards exploring qualitative and quantitative characteristics necessary for refining and understanding the flat wood double cantilever beam (DCB) as a valid means for testing Mode I fracture energy in wood adhesive bonds. This research should be considered an extension of Gagliano's (2001) research into using the same specimen geometry for quasi-static testing. Investigated was appropriate specimen width, angled latewood/earlywood growth distribution influences, significance of adhesive penetration, and system behavior under cyclic loading. Both epoxy and phenol formaldehyde (PF) impregnated films were used with southern yellow pine (SYP) adherends, providing two systems with different characteristics.

Epoxy DCBs were quasi-statically tested with varying widths (10 mm, 15 mm, and 20 mm) to determine if the critical and arrest strain energy release rates, G_{Ic} and G_{Ia}, showed any dependence on width. For all widths the fracture loads of the epoxy bonds were too low to presume the crack tip plastic zone sizes were large enough for the plane stress edge effects to influence the critical and arrest loads. However, it was noted that the scatter in data decreased as width increased. Various reasons for this width dependence were investigated and explanations proposed.

An adhesive penetration analysis was performed for the epoxy bonds using microphotographs of stained microtomed cross-sections. The epoxy clearly penetrated farther into the SYP earlywood growth regions than latewood regions. The difference in adhesive penetration indicates the fracture energy of earlywood bonds is different from latewood bonds. As a result, the wider epoxy DCB specimens, with a better consistency

in growth types exposed on the adherend surface, would show less scatter in fracture energy values.

To investigate why such low toughness values were acquired for the epoxy bonds, fracture testing was performed on the bulk epoxy using single edge notched bend (SENB) specimens. The bulk epoxy's fracture energy was found to be several orders of magnitude higher than the wood-epoxy system; and considering wood's fracture energy is also much greater, the reason for the low values must lie elsewhere. The yield point and elastic modulus, E_a, of the epoxy was also determined. The elastic modulus was found to be more than twice the SYP-DCB adherend vertical stiffness, E_{yy}.

Quasi-static fracture testing was also performed on SYP-DCBs bonded with PF films. By analyzing microphotographs of microtomed cross-sections, the PF penetration into the SYP adherend was shown to be very shallow. This is interesting because the PF-SYP DCBs were found to have much higher critical and arrest fracture energy values than the epoxy-SYP DCBs, yet the epoxy bonds showed much deeper penetration for both latewood and earlywood regions. This indicates that deep adhesive penetration is not a requisite for higher Mode I fracture energy values.

The grain distribution influences were computationally investigated because of the stiffness difference between latewood and earlywood growth and the grain's angle along the length of the beams. All specimens were fabricated with an approximately 3^o grain angle converging at the bondline along the specimen length in the *x-y* plane. The grain angle and the stiffness difference between latewood and earlywood growth caused the effective stiffness, $(E_{xx}I)_{eff}$, to vary along the length of the beam. The effective stiffness variation caused the beam's receptibility for strain energy to also vary. Also

investigated are the effects on effective stiffness from a grain angle in the *x-z* plane. Various latewood grain thickness and distributions were examined within reasonable ranges for southern yellow pine. Based on these considerations, another recommendation is made for an appropriate specimen width.

Cyclic loading tests were performed on PF-SYP DCB's which were coated in aluminum paint and sealed in plastic bags during testing to control the wood moisture content. The cycle frequency was 3 Hz, with a valley to peak load ratio of $R = 0.5$. A softening was observed with cycling. For this reason testing was performed using load control in order to maintain a constant load ratio. Both peak and valley displacements increased with cycling at constant crack length. The local compliance between the peak and valley displacement points was observed to either increase or decrease. This compliance change depended on which increased more with softening, the peak or the valley displacement. With crack growth, stiffening was observed. And though overall the compliance increased after multiple crack extensions, occasionally specimen compliance actually decreased with small crack extensions. This indicates a new method may be needed for determining the applied fracture energy range, ΔG.

Frequently subsequent crack lengths required more cycles to failure than the previous crack length. Considering the test was performed using load control, this indicates a toughening mechanism. Monotonically extending the crack length far from the fatigued region created a fresh crack that did not show the toughened behavior. But toughening did resume with subsequent crack lengths. Plotting the crack growth rate, da/dN, against ΔG for initial crack lengths produced a Paris plot Region II line with a slope of 7.6 da/dN logarithmic decades to 1 ΔG logarithmic decade. Recommendations

were made for future research to make testing bonded wood-wood DCBs using cyclic loading a more viable and valid test choice.

References

Mostovoy, S., E.J. Ripling, "Influence of water on stress corrosion cracking of epoxy bonds." *Journal of Applied Polymer* Science, **13**, (1969), 1083-1111

Mostovoy, S., E. J. Ripling, C. F. Bersch, "Fracture Toughness of Adhesive Joints,"*Journal of Adhesion*, **3**, (1971)

Jones, R. M., *Mechanics of Composite Materials*, Scripta Book Company, Washington, D.C., 1975

Farhad, F., R. Muki, R. A. Westman, "The Role of the adhesive Layer in a Double Cantilever Joint", *Int. J. Solids. Structures*, **13**, (1977), 561-570

Wang, S.S., J.F. Mandell, F. J. McGarry, "An analysis of the crack tip stress field in DCB adhesive fracture specimens", *International Journal of Fracture*, **14**, (1978), 1.

Ebewele, R.O., B.H. River and J.A. Koutsky. "Tapered double cantilever beam fracture tests of phenolic-wood adhesive joints, part II. effects of surface roughness, the nature of surface roughness, and surface aging on joint fracture". *Wood Fiber Sci.* ,**2,** (1980), 1, 40-64.

Kinloch, A.J, S.J. Shaw, "The Fracture Resistance of a Toughened Epoxy Adhesive", *J. Adhesion*, **12,** (1981), 59

Ebewele, R.O., "Wood Processing variables and Adhesive Joint Performance", *Journal of Applied Polymer Science*, **32**, 2979-2988 (1986)

River, B.H., C.T. Scott and J.A. Koutsky. "Adhesive joint fracture behavior during setting and aging". *Forest Prod. J.*, **39,** (1989), 23-28

Williams, J.G., "End Corrections of Orthotropic DCB Specimens", *Composites Science and Technology* ,**35** ,(1989), 367-376

Hashemi, S., A.J. Kinloch, J.G. Williams, "The analysis of interlaminar fracture in uniaxial fibre-polymer composites", *Proc. R. Soc. Lond.* **A 427**, (1990), 173-199

Tsai, K.T., M.P. Ansell, "The fatigue properties of wood in flexure". *J. Mat. Sci.*, **22**, (1990), 865-878

Blackman, B., J. P. Dear, A. J. Kinloch, S. Osiyemi, "The calculation of adhesive fracture energies from double-cantilever beam test specimens", *Journal of Materials Science Letters*, **10,** (1991), 253-256

Cook, J., J. E. Gordon, "A mechanism for the control of crack propagation in all-

brittle systems", *Proc. R. Soc. of London*, **283,** (1991), 508-520

Dillard, D.A., P.R. McDaniels, J.A. Hinkley, "The use of an eccentric compressive load to aid in precracking single edge notch bend specimens", *Journal of Materials Science Letters*, **12,** (1993), 1258-1260

Penado, F. E., "A Closed Form Solution for the Energy Release Rate of the Double Cantilever Beam Specimen with an Adhesive Layer", *Journal of Composite Materials*, **27**, (1993) No. 4

River, *B*.H. and E.A. Okkonen. "Contoured wood double cantilever beam specimen for adhesive joint fracture tests." *Journal of Testing and Evaluation, JTEVA*, **21,** (1993), 1, 21-28

ASTM D 3433-93, Standard test method for fracture strength in cleavage of adhesives in bonded metal joints. Annual Book of ASTM Standards, Vol.15.06, 212-218.

ASTM D 5045-95 "Standard Test Methods for Plane-Strain Fracture Toughness and Strain Energy Release Rate of Plastic Materials", Annual Book of ASTM Standards, 1995

Davalos, J.F., P. Madabhusi-Raman and P. Qiao. "Characterization of mode-I fracture of hybrid material interface bonds by contoured DCB specimens". *Eng. Fracture Mech.* **58**, (1997), 3, 173-192

Qiao, P., J. F. Davalos, P. Madabhusi-Raman, "Characterization of mode-I fracture of hybrid material interface bonds by contoured DCB specimens", *Engineering Fracture Mechanics (UK)*, **58**, (1997), 3, 173-192

Wang, C.H., "Analysis of cracks in constrained layers", *International Journal of Fracture* **83**, (1997), 1-17

Du, J., M.D. Thouless, A.F. Yee, "Development of a process zone in rubber-modified epoxy polymers", **92,** (1998), 3, 271-285

Korjakin, A., R. Rikards, F. G. Buchholz, H. Wang, A.K. Bledzki, A. Kessler, "Compariative Study of Interlaminar Fracture Toughness of GFRP with DifferentFiber Source Treatments", *Polymer Composites*, **19**, (1998), No. 6

Dowling, N.E., *Mechancial Behavior of Materials: Engineering Methods for Deformation, Fracture, and Fatigue (2nd Edition)*, Prentice Hall, 1999

Green, D.W. J.E. Winandy and D.E. Kretschmann. "Mechanical properties of wood". Pages 4:1-45 in *Wood handbook, wood as an engineering material*. Forest Products Society, 1999.

Sernek, M., J. Resnik, F. Kamke, "Penetration of liquid urea-formaldehyde adhesive into beech wood", *Wood and Fiber Science,* **31**, (1999), 1, 41-48

Gagliano, J. M., *An Improved Method for the Fracture Cleavage Testing of Adhesively-Bonded Wood,* M.S. Thesis, V.P.I. & S.U. Blacksburg, VA 2001.

Gagliano, J. M., C. E. Frazier, "Improvements in the fracture cleavage testing of adhesively-bonded wood", *Wood and Fiber Science,* **33**, (2001), 3, 377-385

Groom, L., L. Mott, S. Shaler, "Mechanical Properties of Individual Southern Pine Fibers. Part I. Determination and variability of stress-strain curves with respect to tree height and juvenility", *Wood and Fiber Science,* **34**, (2002), 1, pp14-27

Frihart, C., Personal Conversation, 2004

Cramer, S., D. Kretschmann, R. Lakes, T. Schmidt, "Mesostructure Elastic Properties in Loblolly Pine", *Wood and Fiber Science*, **36,** (2004)

Appendix A1: Matlab codes for horizontally oriented grain, Chapter 4

```
%vertical late wood strain energy
%vwstrain.m, considering alpha = 90, beta = set, theta = irrelevant;
dx = 1/100;
bmax = 20;
hmax = 10;
Lmax = 75;
Eo = 6240;
GIC = 0.27;%N/mm
LWF = 3;
P = 10;

for(bbttaa = 3:2:4)

beta = bbttaa*pi/180;

clear EECavg;
clear EECstd;
clear EECmax;
clear EECmin;
clear Imax;
clear Imin;

h = 0.5;
do = 2;
c = 1;
for(D = 1:9)
    if(ceil(D/3) > c)
        c = c+1;
        h = 0.5
        do = do +1;
    end%if
bb =  0;
for b = 25:5:50

bb = bb+1;

w = h*ones(1,158);%
dho = [-7:do:400];%
mw = size(w);
mdho = size(dho);
K = min(mw(2),mdho(2));
Utot = 0;

for i = 2:Lmax/dx
      dho(i,:) = dho(i-1,:) - dx*tan(beta);
end
%determining which grains are in and which grains are out.
for i = 2:Lmax/dx
     kmin = K+1;
 kmax = -1;
```

```
    w(i,:) = w(1,:);
    dhmin = 2*b;
   for k = K:-1:1
       %k
   % i-(Lmax/dx)


if((dho(i,k)+0.5*w(i,k))>b ) %right hand side

            if(k>kmax)
                kmax = k;
            end %if k
            dho(i,k) = b - 0.5*(b - (dho(i,k) - 0.5*w(i,k)));
            w(i,k) = 2*(b - dho(i,k));

    if(dho(i,k)>b)
    dho(i,k) = 0;
    w(i,k) = 0;
    end% if dho

end %if  right hand side
              if(dho(i,k)>0 &dho(i,k)<dhmin)
                  dhmin = dho(i,k);
                kmin = k;
                %end%if
            end%if
        if(dho(i,k)>=-1*w(i,k)/2 )%left hand side
        if((dho(i,k)<=w(i,k)/2));
            dho(i,k)=0.5*(dho(i,k)+w(i,k)/2);
            w(i,k) = 2*dho(i,k);
            %if(k<kmin)

        end% if
            else
                w(i,k) = 0;
                dho(i,k) = 0;
    end%if  left hand side
end % for k

L =i*dx;
Il = (1/12)*sum(w(i,kmin:kmax))*(hmax^3)*LWF;
Ie = (1/12)*(b-sum(w(i,kmin:kmax)))*(hmax^3);
if(Ie<0 | Il<0)
Io(i) = max(Il,Ie);
else
Io(i) = Il+Ie;
end
Ul = 0;
if(Il>0)
Ul = (((P*L)^2)/(2*Eo*Il))*dx;
end
Ue = 0;
if(Ie>0)
Ue = (((P*L)^2)/(2*Eo*Ie))*dx;
end
Utot(i) = Ul+Ue+Utot(i-1);
```

```
dUdx(i) = (Utot(i)-Utot(i-1))/dx;
lfact = sum(w(i,kmin:kmax))/b;
efact = (1-lfact);
EEC(i) = (1/Io(i)^2)*((hmax^3)/12)/(efact*Eo+LWF*lfact*Eo);
    Pc(i) = sqrt((Eo*Io(i)*b*GIC)/(L^2));
end% for i

EECavg(D,bb) = mean(EEC(2:length(EEC)));
EECstd(D,bb) = std(EEC(2:length(EEC)));
EECmax(D,bb) = max(EEC(2:length(EEC)));
EECmin(D,bb) = min(EEC(2:length(EEC)));
Imax(D,bb) = max(Io(2:length(Io)));
Imin(D,bb) = min(Io(2:length(Io)));
Imin./Imax

if(b==bmax)
    h = h+0.5;
end %if b
end %for b
end %while D

if(bbttaa == 1)
   save bta1EECavg.txt EECavg -ascii -tabs
   save bta1EECstd.txt EECstd -ascii -tabs
   save bta1EECmax.txt EECmax -ascii -tabs
   save bta1EECmin.txt EECmin -ascii -tabs
   save bta1Imax.txt Imax -ascii -tabs
   save bta1Imin.txt Imin -ascii -tabs
end %if
if(bbttaa == 2)
   save bta2EECavg.txt EECavg -ascii -tabs
   save bta2EECstd.txt EECstd -ascii -tabs
   save bta2EECmax.txt EECmax -ascii -tabs
   save bta2EECmin.txt EECmin -ascii -tabs
   save bta2Imax.txt Imax -ascii -tabs
   save bta2Imin.txt Imin -ascii -tabs

end %if
if(bbttaa == 3)
   save bta3EECavg.txt EECavg -ascii -tabs
   save bta3EECstd.txt EECstd -ascii -tabs
   save bta3EECmax.txt EECmax -ascii -tabs
   save bta3EECmin.txt EECmin -ascii -tabs
   save bta3Imax.txt Imax -ascii -tabs
   save bta3Imin.txt Imin -ascii -tabs

end %if

if(bbttaa == 4)
   save bta4EECavg.txt EECavg -ascii -tabs
   save bta4EECstd.txt EECstd -ascii -tabs
   save bta4EECmax.txt EECmax -ascii -tabs
   save bta4EECmin.txt EECmin -ascii -tabs
   save bta4Imax.txt Imax -ascii -tabs
   save bta4Imin.txt Imin -ascii -tabs

end %if
```

```
if(bbttaa == 5)
   save bta5EECavg.txt EECavg -ascii -tabs
   save bta5EECstd.txt EECstd -ascii -tabs
   save bta5EECmax.txt EECmax -ascii -tabs
   save bta5EECmin.txt EECmin -ascii -tabs
   save bta5Imax.txt Imax -ascii -tabs
   save bta5Imin.txt Imin -ascii -tabs

end %if

if(bbttaa == 6)
   save bta6EECavg.txt EECavg -ascii -tabs
   save bta6EECstd.txt EECstd -ascii -tabs
   save bta6EECmax.txt EECmax -ascii -tabs
   save bta6EECmin.txt EECmin -ascii -tabs
   save bta6Imax.txt Imax -ascii -tabs
   save bta6Imin.txt Imin -ascii -tabs

end %if
if(bbttaa == 7)
   save bta7EECavg.txt EECavg -ascii -tabs
   save bta7EECstd.txt EECstd -ascii -tabs
   save bta7EECmax.txt EECmax -ascii -tabs
   save bta7EECmin.txt EECmin -ascii -tabs
   save bta7Imax.txt Imax -ascii -tabs
   save bta7Imin.txt Imin -ascii -tabs

end %if

if(bbttaa == 8)
   save bta8EECavg.txt EECavg -ascii -tabs
   save bta8EECstd.txt EECstd -ascii -tabs
   save bta8EECmax.txt EECmax -ascii -tabs
   save bta8EECmin.txt EECmin -ascii -tabs
   save bta8Imax.txt Imax -ascii -tabs
   save bta8Imin.txt Imin -ascii -tabs

end %if
end %for bbttaa
%quit
```

Appendix A2: Matlab codes for vertically oriented grain, Chapter 4

```
%vertical late wood strain energy%
vwstrain.m, considering alpha = 90, beta = set, theta = irrelevant;
bmax = 50;
hmax = 10;
Lmax = 105;
Eo = 6240;

LWF = 3;
P = 10;
dx = 1/100;
for(bbttaa = 3:2:4)

beta = bbttaa*pi/180;

clear EECavg;
clear EECstd;
clear EECmax;
clear EECmin;
clear Imax;
clear Imin;

h = 0.5;
do = 2;
c = 1;
for(D = 1:9)

    if(ceil(D/3) > c)
        c = c+1;
        h = 0.5
        do = do +1;
    end%if
bb =  0;
for b = 5:5:bmax
keyboard
bb = bb+1;

w = h*ones(1,150);%
dho = [-7:do:800];%
mw = size(w);
mdho = size(dho);
K = min(mw(2),mdho(2));
Utot = 0;

for i = 2:Lmax/dx
      dho(i,:) = dho(i-1,:) - dx*tan(beta);
end
%determining which grains are in and which grains are out.
for i = 2:Lmax/dx
     kmin = K+1;
 kmax = -1;

    w(i,:) = w(1,:);
   for k = 1:K
```

```
       %k
   % i-(Lmax/dx)


if((dho(i,k)+0.5*w(i,k))>b )

            if(k>kmax)
                kmax = k;
            end %if k
            dho(i,k) = b - 0.5*(b - (dho(i,k) - 0.5*w(i,k)));
            w(i,k) = 2*(b - dho(i,k));

    if(dho(i,k)>b)
    dho(i,k) = 0;
    w(i,k) = 0;
    end% if dho

    end %if

        if(dho(i,k)>=-1*w(i,k)/2 )
        if(dho(i,k)<=w(i,k)/2);
            dho(i,k)=0.5*(dho(i,k)+w(i,k)/2);
            w(i,k) = 2*dho(i,k);
            if(k<kmin)
                kmin = k;
            end%if
        end% if
            else
                w(i,k) = 0;
                dho(i,k) = 0;
    end%if
end % for k

L =i*dx;
Il = (1/12)*sum(w(i,:))*(hmax^3)*LWF;
Ie = (1/12)*(b-sum(w(i,:)))*(hmax^3);
if(Ie<0 | Il<0)
Io(i) = max(Il,Ie);
end
Io(i) = Il+Ie;
Ul = 0;
if(Il>0)
Ul = (((P*L)^2)/(2*Eo*LWF*Il))*dx;
end
Ue = 0;
if(Ie>0)
Ue = (((P*L)^2)/(2*Eo*Ie))*dx;
end
Utot(i) = Ul+Ue+Utot(i-1);
lfact = sum(w(i,kmin:kmax))/b;
efact = (1-lfact);
EEC(i) = (1/Io(i)^2)*((hmax^3)/12)/(efact*Eo+LWF*lfact*Eo);

end% for i

EECavg(D,bb) = mean(EEC(2:length(EEC)));
EECstd(D,bb) = std(EEC(2:length(EEC)));
```

```
EECmax(D,bb) = max(EEC(2:length(EEC)));
EECmin(D,bb) = min(EEC(2:length(EEC)));
Imax(D,bb) = max(Io(2:length(Io)));
Imin(D,bb) = min(Io(2:length(Io)));


if(b==bmax)
    h = h+0.5;
end %if b
end %for b
end %while D

if(bbttaa == 1)
   save bta1EECavg.txt EECavg -ascii -tabs
   save bta1EECstd.txt EECstd -ascii -tabs
   save bta1EECmax.txt EECmax -ascii -tabs
   save bta1EECmin.txt EECmin -ascii -tabs
   save bta1Imax.txt Imax -ascii -tabs
   save bta1Imin.txt Imin -ascii -tabs
end %if
if(bbttaa == 2)
   save bta2EECavg.txt EECavg -ascii -tabs
   save bta2EECstd.txt EECstd -ascii -tabs
   save bta2EECmax.txt EECmax -ascii -tabs
   save bta2EECmin.txt EECmin -ascii -tabs
   save bta2Imax.txt Imax -ascii -tabs
   save bta2Imin.txt Imin -ascii -tabs

end %if
if(bbttaa == 3)
   save bta3EECavg.txt EECavg -ascii -tabs
   save bta3EECstd.txt EECstd -ascii -tabs
   save bta3EECmax.txt EECmax -ascii -tabs
   save bta3EECmin.txt EECmin -ascii -tabs
   save bta3Imax.txt Imax -ascii -tabs
   save bta3Imin.txt Imin -ascii -tabs

end %if

if(bbttaa == 4)
   save bta4EECavg.txt EECavg -ascii -tabs
   save bta4EECstd.txt EECstd -ascii -tabs
   save bta4EECmax.txt EECmax -ascii -tabs
   save bta4EECmin.txt EECmin -ascii -tabs
   save bta4Imax.txt Imax -ascii -tabs
   save bta4Imin.txt Imin -ascii -tabs

end %if
if(bbttaa == 5)
   save bta5EECavg.txt EECavg -ascii -tabs
   save bta5EECstd.txt EECstd -ascii -tabs
   save bta5EECmax.txt EECmax -ascii -tabs
   save bta5EECmin.txt EECmin -ascii -tabs
   save bta5Imax.txt Imax -ascii -tabs
   save bta5Imin.txt Imin -ascii -tabs

end %if
```

```
if(bbttaa == 6)
   save bta6EECavg.txt EECavg -ascii -tabs
   save bta6EECstd.txt EECstd -ascii -tabs
   save bta6EECmax.txt EECmax -ascii -tabs
   save bta6EECmin.txt EECmin -ascii -tabs
   save bta6Imax.txt Imax -ascii -tabs
   save bta6Imin.txt Imin -ascii -tabs

end %if
if(bbttaa == 7)
   save bta7EECavg.txt EECavg -ascii -tabs
   save bta7EECstd.txt EECstd -ascii -tabs
   save bta7EECmax.txt EECmax -ascii -tabs
   save bta7EECmin.txt EECmin -ascii -tabs
   save bta7Imax.txt Imax -ascii -tabs
   save bta7Imin.txt Imin -ascii -tabs

end %if

if(bbttaa == 8)
   save bta8EECavg.txt EECavg -ascii -tabs
   save bta8EECstd.txt EECstd -ascii -tabs
   save bta8EECmax.txt EECmax -ascii -tabs
   save bta8EECmin.txt EECmin -ascii -tabs
   save bta8Imax.txt Imax -ascii -tabs
   save bta8Imin.txt Imin -ascii -tabs

end %if
end %for bbttaa
%quit
```

Appendix B: Matlab code for extracting data points from stored array, Chapter 5

```
%fwork.m, Script to extract and separate time, load and displacement
%data from MTS System record file
'Processing data file'
        fid=fopen('pf5s1129.dat');
        t =1;

        while 1

            tline = fgetl(fid);
            if ~ischar(tline), break, end
            temp = str2num(tline);
            if(size(temp)>0)
                a(t,:) = temp;
               %disp(a(t,:))
                t = t+1;
            end

        end
        fclose(fid);
        'Saving seperate time, displacement and load to seperate file'
        t = a(:,1);
        d = a(:,2);
        P = a(:,3);
        save P5s1129.txt P -ascii
        save t5s1129.txt t -ascii
        save d5s1129.txt d -ascii


%comp.m
%program to read the compliance from the cycled load vs. displacement
curve
%input data:  t - time, d - displacement, P - load
%

clear compup
clear compdn
%clear
%Nmin = 2;
%Nmax = 90;
%load t5s151.txt
%load d5s151.txt
%load P5s151.txt
%P = P5s151;
%d = d5s151;
%t = t5s151;
dt = 0.01;%sensitivity for time range checks
dd = 0.01;%sensitivity for displacement checks

%Finding the appropriate index for cycle region starting around Nmin
%use time vector, knowing that w = 3Hz, so t = N*3 (sec);
begi = 1;

i = begi;
```

```
while( i < length(t))

    if((t(i)+dt > Nmin/3 & t(i)-dt<Nmin/3) | t(i) == Nmin/3)
    begi =i-2;
    i = length(t);

    end %if
%keyboard
    i = i+1;
end% while
        'Determining up and down swing compliances starting at Nmin'
mnew = -1
i = begi
%keyboard
dInew = [0 1000];
%tInew = 0;
for N = Nmin:(Nmax+(Nmax-Nmin))%2*Nmax%
% now to determine the region for which cycle N is in its up/down-swing
%N
i = begi;
%keyboard
   di = 2;%2;
while( i < (length(t)-di))

    dthree = d(begi:(i+di));
    tthree = t(begi:(i+di));
   % [Y,I] = sort(dthree);%(begi:i+1));
    dIold = dInew;
  %  tIold = tInew;
    mold = mnew;
    mnew = polyfit(tthree, dthree,1);

    %    if(sign(mnew(1)) ==sign(mold(1)))

    if(dthree(length(dthree))>dIold(1
       dInew(1) = dthree(length(dthree));
       dInew(2) = dthree(1);
       endi = i+1;
   elseif( dthree(length(dthree))<dIold(2))
       dInew(2) = dthree(length(dthree));
       dInew(1) = dthree(1);
       endi = i+1;
        else
            [Y,I] = sort(dthree);
            dInew(2) = max(dthree(1),dthree(length(dthree)));
            dInew(1) = min(dthree(1),dthree(length(dthree)));

            endi = i+2;%I(length(I));
            i = length(t);
           % endi = begi;
        end %if
    i = i+1;
end %while
mold = -1*mnew;

dtemp = d(begi:endi);
Ptemp = P(begi:endi);
```

```
m = POLYFIT(dtemp,Ptemp,1);
dmin = min(d(begi:endi));
Pmin = min(P(begi:endi));
dmax = max(d(begi:endi));
Pmax = max(P(begi:endi));
%keyboard
%determining the area under graph in order to compare (viscoelastic?)
decay
%within each cycle
A = 0;
for(j = begi:(endi-1))
    dd = d(j+1)-d(j);
    dP = P(j+1)-P(j);
    A = A+ dd*dP;
end
if(sign(mnew(1))>0)
    compup(N) = 1/m(1);
    dminup(N) = dmin;
    dmaxup(N) = dmax;
    Pminup(N) = Pmin;
    Pmaxup(N) = Pmax;
    Aup(N) = A;
else
    compdn(N) = 1/m(1);
    dmindn(N) = dmin;
    dmaxdn(N) = dmax;
    Pmindn(N) = Pmin;
    Pmaxdn(N) = Pmax;
    Adn(N) = A;
end %if
begi = endi

end  %for N

%removing 0's from compup and compdn
n = 1;
for N = Nmin:min(length(compup),length(compdn));
    if(compup(N)>0)
        upcomp(n) = compup(N);
        updmin(n) = dminup(N);
        updmax(n) = dmaxup(N);
        upPmin(n) = Pminup(N);
        upPmax(n) = Pmaxup(N);

        dncomp(n) = compdn(N+1);
        dndmin(n) = dmindn(N+1);
        dndmax(n) = dmaxdn(N+1);
        dnPmin(n) = Pmindn(N+1);
        dnPmax(n) = Pmaxdn(N+1);
        n = n+1;
        Atot(n) = Aup(N) - Adn(N+1);
    end

end
save upcomp.txt upcomp -ascii
save dncomp.txt dncomp -ascii
```